Development of Time of Flight Modulation of Intensity by Zero Effort for Larmor

Niels Geerits

Student Number: 4283503

Committee:
Dr. Ing. J. Plomp, Dr. W.G. Bouwman, Dr. S.W.H. Eijt and Dr. Ir. N.H. van Dijk

Programme: Master of Applied Physics at Delft University of Technology

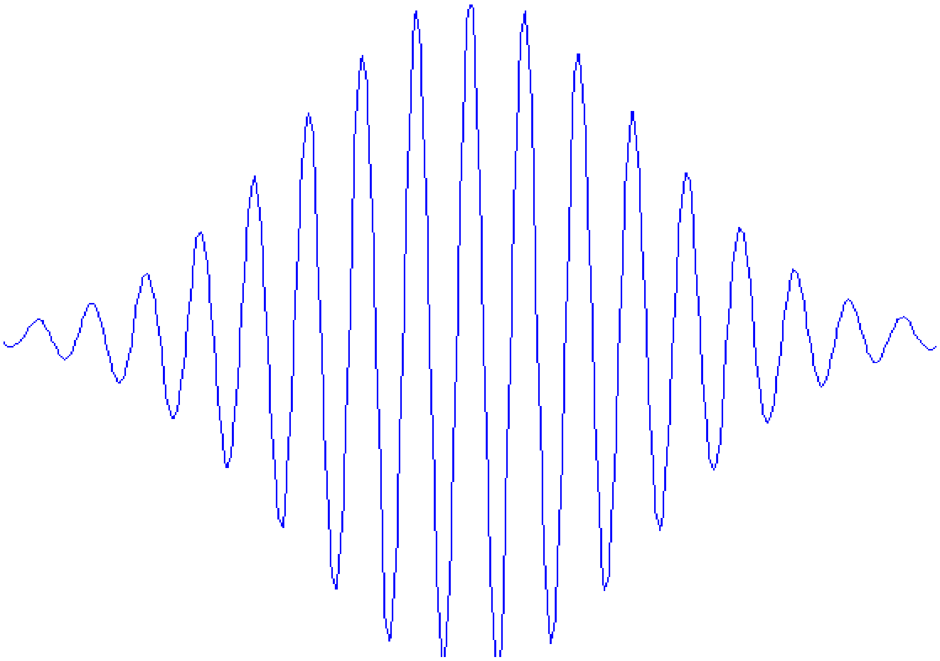

October 18, 2018

Abstract

A time of flight MIEZE spectrometer, which employs radio frequency spin flippers with square pole shoes and a magnetic yoke, is presented. These flippers can achieve higher fields than conventional resonant RF spin flippers, which employ an air core. High fields are crucial for the construction of a high resolution and compact MIEZE spectrometer. Setups using conventional flippers and novel flippers are built for comparison and a variety of experiments to characterize time of flight MIEZE instruments. Evidence is presented, which indicates that the high field flippers are capable of generating a $100kHz$ MIEZE signal, with an amplitude similar to that obtained with a conventional MIEZE setup. Furthermore the need for a fast and thin detector is demonstrated both experimentally and by the use of Monte-Carlo simulations. In addition the shape of the MIEZE focal spot has been determined to be Gaussian. Finally the importance of stable timing for time of flight MIEZE is demonstrated. This research is relevant for the implementation of MIEZE on the Larmor instrument at ISIS pulsed neutron source in the UK.

Contents

Acknowledgments

I wish to express my gratitude towards the entire research group for their openness, trust and effort to make me feel like a part of their team. Special thanks to Jeroen Plomp for providing this project to me and for his efforts which allowed me to travel to PNCMI 2018 and the ISIS neutron source for experiments. Furthermore I want to thank Steven Parnell for helping me to get started and his guidance and contributions to the project along the way. Furthermore I am indebted towards Michel Thijs who provided both his technical expertise and numerous FE simulations of the setup. In addition I wish to extend my gratitude towards both Ad van Well and Wim Bouwman for our useful discussions on neutron scattering and spin echo. Finally I would also like to thank Stephan Eijt and Niels van Dijk for agreeing to take part in my commission.

Index of Standards

Here you will find the mathematical standards used in this report.

Fourier Transform: A non unitary definition of the Fourier transform is used:
$F(\omega) = \int_{-\infty}^{\infty} f(t)e^{-i\omega t}dt$
Laplace Transform: The standard definition of the Laplace transform is used:
$F(s) = \int_{0}^{\infty} f(t)e^{-st}dt$
Inverse Laplace Transform: The following definition of the inverse Laplace transform is used:
$f(t) = \frac{1}{2\pi i} \lim_{T\to\infty} \int_{\alpha-iT}^{\alpha+iT} F(t)e^{st}ds$
Sinc functions: The non normalized definition of the sinc function is used:
$sinc(x) = \frac{\sin(x)}{x}$
Matrix Vector Notation: Usually matrix vector notation is used unless indicated otherwise: $\vec{u} = A\vec{v}$. Vectors can be identified by the arrows, while matrices are indicated in the text.
Index notation: In some cases when dealing with 2x2 matrices and vectors containing two elements a special index notation will be used: $v_i = A_{ij}v_j$, where $i \neq j$. In this case the ith element of $\vec{v}$ is given by the jth element of $\vec{v}$ multiplied by some scalar given by A_{ij}

1 Introduction

The Larmor instrument, situated at ISIS target station 2 in the UK, is a versatile tool for materials research using polarised neutrons. At ISIS neutrons are generated by firing a high energy proton pulses onto a high Z target. The collision causes the target nucleus to decompose into a large number of high energy nuclear fragments, many of which are neutrons. This process is called spallation [1][2]. The Larmor instrument can operate in a variety of modes, such as (polarised) Small Angle Neutron Scattering (SANS), used to explore structures on the order of $1-100nm$, Spin Echo SANS (SESANS) and Spin Echo Modulated SANS (SEMSANS), both used to look at larger structures on the order of $0.1-20\mu m$ [3], Larmor Diffraction (LD), a technique for the study of crystals, Neutron Resonant Spin Echo (NRSE) and Modulation of IntEnsity by Zero Effort (MIEZE), which are both used to probe the dynamics of a sample (i.e. Magnons) in the $0.001-1000ns$ range [4][5][6]. With the exception of NRSE, LD and MIEZE all of these modes have been tested and verified to be working with the Larmor instrument. While techniques like Neutron Spin Echo (NSE) and NRSE have a larger energy resolution than MIEZE [5], MIEZE has a few advantages over NRSE and NSE, since it can also be used to measure the dynamics of hydrogenous and magnetic samples whereas NRSE and NSE cannot [7]. These magnetic materials are interesting in particular since they may have applications in spintronics and quantum computing [8][9], which could increase digital data storage capacity and computation power. These polarized options for the Larmor instrument are developed by the Delft University of Technology as part of a grant from NWO.

In this report a MIEZE mode is developed for the Larmor instrument. As the name suggests a MIEZE instrument modulates the neutron beam intensity in time. The amplitude of the intensity oscillations is maximal when no sample is placed in the instrument. MIEZE employs two Neutron Resonant Spin Echo coils (NRSE coils), which induce a longitudinal Stern-Gerlach effect. The first NRSE coil causes the two neutron spin states to go out of phase, while the second coil overcompensates the effects of the first coil. As a result the phase difference between the two states will diminish as the neutrons approach the focus point where they are measured (Figure 1 [5])[3]. This allows one to place the sample after all the spin manipulation instrumentation. When an inelastic scattering event takes place in the sample the two spin states will arrive at the detector slightly out of phase. As a result the amplitude of the intensity modulation will be decreased. Hence this decrease in amplitude is a measure for the energy transfer between the sample and the neutrons [5].

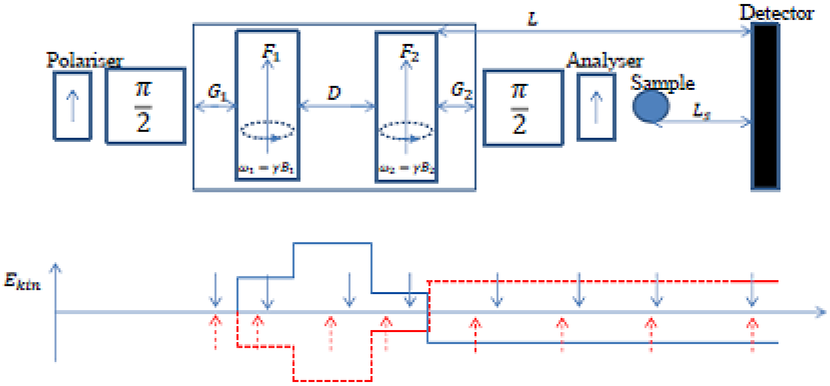

Figure 1. Schematic of a typical MIEZE setup (top) and the quantum mechanical explanation of MIEZE (bottom).

Typically MIEZE spectrometers utilize rectangular air cored electromagnets with RF coils (resonant flippers). The RF frequency is tuned such that $\omega_i = \gamma B_i$. The MIEZE modulation frequency is twice the frequency difference between the two NRSE coils [4]. However the Larmor instrument employs a new type magnet which utilizes square pole shoes and an RF coil. Due to the pole shoes these novel flippers can achieve higher fields than resonant flippers. In addition these spin flippers are equipped with a gradient coil, allowing them to operate in a "gradient mode" [10]. As noted above, Larmor is situated at ISIS, which is a pulsed neutron source. A consequence of this is that the neutron wavelength is encoded in the neutron flight time. This is often referred to as Time of Flight (TOF). While the reactor source at TU Delft is continuous, one can employ a device which consists of two rotating disks with a pie piece shaped cut in each disk (called a chopper) to create a virtual pulsed source, which enables one to do TOF measurements.

To demonstrate the feasibility of a MIEZE mode on Larmor, we construct two MIEZE setups at TU Delft. The first MIEZE setup utilizes conventional resonant flippers and serves as a benchmark setup, while the second setup will utilize the novel NRSE coils, also used by Larmor. Both setups employ a chopper, allowing one to do TOF MIEZE measurements [11].

This report explores the theory necessary to describe and understand TOF MIEZE in section 2. In section 3 various experimental methods are discussed and the MIEZE setups are shown. Next in the section 4 the experimental results are shown. Following this in section 5 these results are discussed and explained in terms of the theory. Section 6 discusses the future of MIEZE on Larmor. Finally in section 7 a conclusion of the research shown in this report is given.

2 Theory

In this section the theoretical basis of MIEZE is discussed, this is done from a quantum mechanical perspective, where we assume that the incoming neutrons can be described as plane waves. A similar approach is shown in [4]. In the first subsection the Schroedinger equation for a neutral spin $\frac{1}{2}$ particle in a magnetic field is derived [12]. The next four subsections will discuss the core components of our MIEZE setups, static magnetic fields [12], resonant radio frequency spin flippers [13] and the gradient mode of our novel spin flippers. In the following subsection these results are used to derive the MIEZE focusing condition and the consequences of a poorly aligned setup are discussed [4]. The subsequent subsection demonstrates, using the focusing condition, how the MIEZE technique can be used to measure energy transfers between a sample and the neutrons [14] (also known as inelastic scattering). In addition the resolution of a MIEZE spectrometer is derived. This resolution turns out to scale with the phase difference of the two neutron spin states at the sample position. In the final subsection the inelastic scattering function of liquids is derived in the low energy limit.

2.1 Derivation of the Schroedinger Equation for a Neutral Spin $\frac{1}{2}$ Particle in a Magnetic Field

In the following subsection it will be demonstrated that magnetic fields have an influence on neutrons. To do so we will derive the Schroedinger equation for any neutral spin $\frac{1}{2}$ particle in a magnetic field. In general the Schroedinger equation is given by:

$$H\psi = E\psi \tag{1}$$

with ψ the wavefunction, E the total energy of the system and H the hamiltonian which is given by

$$H = T + V(\vec{r}) = -\frac{\hbar^2}{2m}\nabla^2 + V(\vec{r}) \tag{2}$$

With T the particles kinetic energy and $V(\vec{r})$ the potential energy, $\hbar$ denotes the reduced planck constant and m the particles mass. To derive an appropriate expression for the potential energy, we first look at the force a magnetic field exerts on a magnetic dipole. It turns out this depends on the model used for the magnetic dipole moment [12]. If one assumes that the magnetic dipole moment, $\vec{\mu}$ is created by two oppositely charged magnetic monopoles separated by a certain distance the force equals:

$$\vec{F} = -\nabla[\vec{\mu} \cdot \vec{B}] - \vec{\mu} \times \nabla \times \vec{B}$$

On the other hand if the magnetic dipole moment is created only by loop currents the force would be given by:

$$\vec{F} = -\nabla[\vec{\mu} \cdot \vec{B}]$$

To this date there has been no experimental evidence for the existence of magnetic monopoles, therefore it is assumed that the second model is correct. As a result the potential is simply given by:

$$V = -\vec{\mu} \cdot \vec{B} \tag{3}$$

Thus the Schroedinger equation is given by [12]:

$$-\frac{\hbar^2}{2m}\nabla^2\psi - \vec{\mu} \cdot \vec{B}\psi = E\psi \tag{4}$$

Note that with the Schroedinger equation we are talking about operators. This means that the dipole moment used here is the magnetic dipole moment operator, and not simply a vector like in classical electrodynamics. This operator shares the property of all quantum mechanical operators that

$$< \vec{\mu} > = \langle\psi| \vec{\mu} |\psi\rangle$$

Classically we know that the magnetic moment of a loop current is given by

$$\vec{\mu} = I\vec{A} = \frac{q\vec{v}}{2\pi|r|}\pi|r|^2\hat{n} = -\frac{q\vec{v}}{2} \times \vec{r} \tag{5}$$

With $\hat{n}$ the normal vector of the area spanned by the loop current. Using the definition of angular momentum $\vec{L} = m\vec{r} \times \vec{v}$ we find

$$\vec{\mu} = \frac{q}{2m}\vec{L} = \gamma\vec{L} \tag{6}$$

Where γ is the gyromagnetic ratio. Finally we use the relationship between spin and angular momentum $\vec{L} = \frac{\hbar}{2}\vec{\sigma}$, with $\vec{\sigma} = \sigma_x\hat{x} + \sigma_y\hat{y} + \sigma_z\hat{z}$, with σ_i a Pauli matrix.

$$\sigma_x = \begin{pmatrix} 0 & 1 \\ 1 & 0 \end{pmatrix} \quad \sigma_y = i\begin{pmatrix} 0 & -1 \\ 1 & 0 \end{pmatrix} \quad \sigma_z = \begin{pmatrix} 1 & 0 \\ 0 & -1 \end{pmatrix} \tag{7}$$

Note that the Pauli matrices are part of a special mathematical group called the SU(2) group (Special Unitary group), this means they are all unitary and that the absolute value of their determinants are equal to one. Using the definition of the angular momentum operator we can derive the following equation for the magnetic moment operator [15].

$$\vec{\mu} = \frac{\gamma\hbar}{2}\vec{\sigma} \tag{8}$$

Yielding the final expression for our Schroedinger equation.

$$-\frac{\hbar^2}{2m}\nabla^2\vec{\psi}(\vec{x}) - \frac{\hbar\gamma}{2}[\vec{\sigma} \cdot \vec{B}]\vec{\psi}(\vec{x}) = E\vec{\psi}(\vec{x}) \tag{9}$$

One will note $\vec{\psi} = \psi_i$ with the subscript, $i = 1$ or 2, indicating the spin state (up or down).

The exact calculation of γ for a neutron is complex, because one must consider the movement and spins of each quark which create the neutron. γ has been experimentally determined to be $1.8301 * 10^8 \frac{T}{s}$ [15]. In the calculation of the gyromagnetic ratio one assumes the quarks to be in the ground state, however it is also possible to have excited quarks (this is referred to as Δ^0 baryon). If this is the case the magnetic moment is different from the normal neutron magnetic moment.

2.2 Neutrons in Homogeneous Static Magnetic Fields

As described earlier, in this subsection we will explore wavefunctions for neutrons in homogeneous static magnetic fields (similar calculations can be found in [12][15]). We assume zero field for $x < 0$ and a non zero static field pointing in an arbitrary direction for $x > 0$. The incident neutron propagates from $-\infty$ to the boundary region at $x = 0$, where it is partially transmitted and reflected (Figure 2).

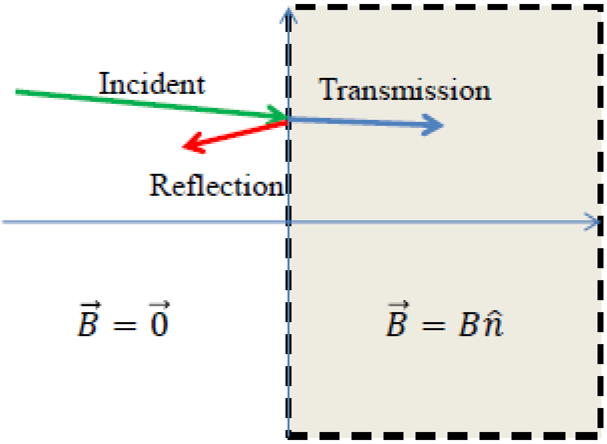

Figure 2. Schematic of the proposed problem. An incident neutron hits a semi infinite magnetic field region and is partially reflected and transmitted.

To solve this problem we shall first formulate the time independent schroedinger equation (found in the previous subsection as equation (9)) and the boundary conditions.

$$-\frac{\hbar^2}{2m}\nabla^2\vec{\psi}(\vec{x}) - \frac{\hbar\gamma}{2}[\vec{\sigma}\cdot\vec{B}]\vec{\psi}(\vec{x}) = E\vec{\psi}(\vec{x}) \tag{10}$$

$$\psi_i(x=0,y,z) = c_i e^{ik_y y} = [1+R_i]e^{ik_y y} \tag{11}$$

$$\frac{d\psi_i}{dx}(x=0,y,z) = -ik_x d_i e^{ik_y y} = -ik_x[1-R_i]e^{ik_y y} \tag{12}$$

c_i and d_i are arbitrary constants for now and R is the reflection coefficient (we use this later). This is simply the Schroedinger equation for a step potential, with the added difficulty of the two spin states being coupled. The problem can be solved by applying the Laplace transform on x and a Fourier transform on y. Doing so leads to the following set of linear equations.

$$-\frac{\hbar^2}{2m}[(s_x^2 - w_y^2 + \frac{\gamma m}{\hbar}[\vec{\sigma}\cdot\vec{B}])\vec{\Psi} - (s_x c_i - ik_x d_i)\delta(\omega_y - k_y)] = E\vec{\Psi} \tag{13}$$

The above set of equations is a matrix vector problem.

$$A\vec{\Psi} = \vec{K} \tag{14}$$

With

$$A_{11} = \frac{\hbar^2}{2m}[s_x^2 - w_y^2] + \frac{\hbar\gamma}{2}[\vec{\sigma}\cdot\vec{B}]_{11} + E$$

$$A_{12} = \frac{\hbar\gamma}{2}[\vec{\sigma}\cdot\vec{B}]_{12}$$

$$A_{21} = \frac{\hbar\gamma}{2}[\vec{\sigma}\cdot\vec{B}]_{21}$$

$$A_{22} = \frac{\hbar^2}{2m}[s_x^2 - w_y^2] + \frac{\hbar\gamma}{2}[\vec{\sigma}\cdot\vec{B}]_{22} + E$$

$$K_i = \frac{\hbar^2}{2m}(s_x c_i - ik_x d_i)\delta(\omega_y - k_y)$$

Because the matrix vector problem is only 2 by 2 it can easily be inverted:

$$\vec{\Psi} = \frac{1}{A_{11}A_{22} - A_{12}A_{21}} \begin{pmatrix} A_{22} & -A_{12} \\ -A_{21} & A_{11} \end{pmatrix} \vec{K} \tag{15}$$

This yields the following decoupled equations, using $\epsilon_i = \frac{2m}{\hbar^2}(E_0 + \frac{\hbar\gamma}{2}[\vec{\sigma} \cdot \vec{B}]_{ii})$:

$$\Psi_i = \frac{[s_x^2 - w_y^2 + \epsilon_j][s_x c_i - ik_x d_i] - \frac{m\gamma}{\hbar}[\vec{\sigma} \cdot \vec{B}]_{ij}[s_x c_j - ik_x d_j]}{[s_x^2 - w_y^2 + \epsilon_j][s_x^2 - w_y^2 + \epsilon_i] - \frac{m^2\gamma^2}{\hbar^2}[\vec{\sigma} \cdot \vec{B}]_{ij}[\vec{\sigma} \cdot \vec{B}]_{ji}} \delta(w_y - k_y) \tag{16}$$

with $i \neq j$. Next we substitute $\epsilon_0 = \epsilon_1 + \epsilon_2$. We also note that Pauli matrices are hermitian therefore $[\vec{\sigma} \cdot \vec{B}]_{ij}[\vec{\sigma} \cdot \vec{B}]_{ji} = \left|\vec{\sigma} \cdot \vec{B}\right|^2_{ij}$

$$\Psi_i = \frac{[s_x^2 - w_y^2 + \epsilon_j][s_x c_i - ik_x d_i] - \frac{m\gamma}{\hbar}[\vec{\sigma} \cdot \vec{B}]_{ij}[s_x c_j - ik_x d_j]}{s_x^4 + s_x^2[\epsilon_0 - 2w_y^2] - w_y^2\epsilon_0 + \epsilon_i\epsilon_j + w_y^4 - \frac{m^2\gamma^2}{\hbar^2}\left|\vec{\sigma} \cdot \vec{B}\right|^2_{ij}} \delta(w_y - k_y) \tag{17}$$

We are interested in finding the wavefunction in real space. To achieve this we must apply the inverse Laplace transform to the above equation.

$$\psi_i(x, \omega_y) = \frac{1}{2\pi i} \lim_{T \to \infty} \int_{\alpha - iT}^{\alpha + iT} \Psi_i e^{s_x x} ds_x \tag{18}$$

This is calculated by integrating over the so called Bromwich contour (Figure 3).

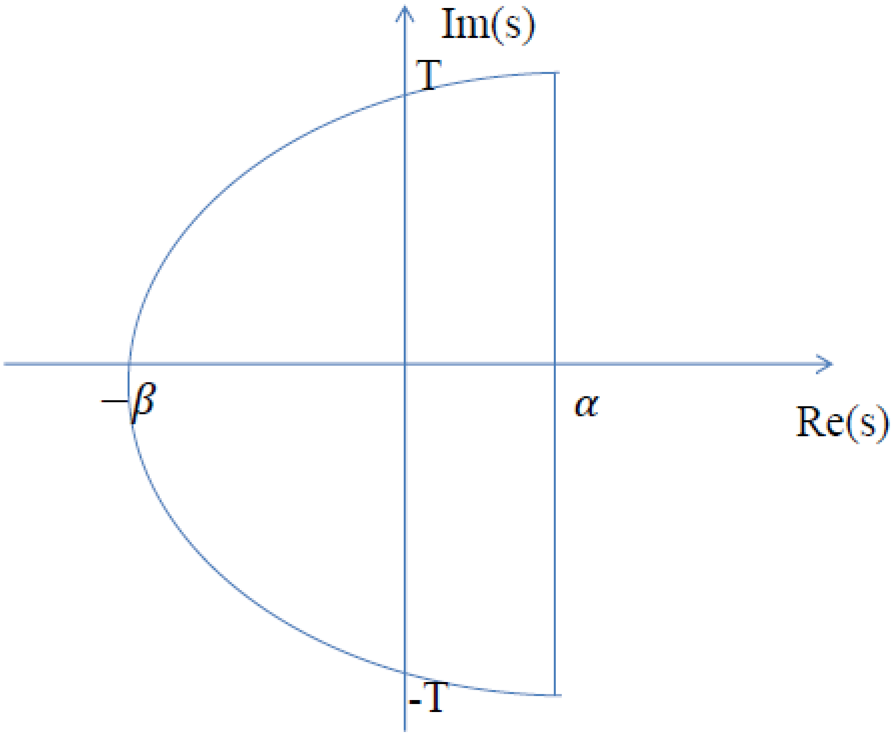

Figure 3. Schematic of the Bromwich contour. β and T are taken to infinity.

In this particular case we can apply Jordan's Lemma, which states that the integral over the curved part of the Bromwich contour is zero for all $x > 0$, thus the inverse Laplace transform is given by Cauchy's residue theorem.

$$\psi_i(x,\omega_y) = \sum Res(\Psi_i e^{s_x x}) \tag{19}$$

To calculate the residues of $\Psi_i e^{s_x x}$ we must first find the poles of said function. In this case the poles of our function are given by the zeros of the denominator of Ψ_i:

$$s_x^4 + s_x^2[\epsilon_0 - 2w_y^2] - w_y^2\epsilon_0 + \epsilon_i\epsilon_j + w_y^4 - \frac{m^2\gamma^2}{\hbar^2}\left|\vec{\sigma}\cdot\vec{B}\right|_{ij}^2 = 0$$

$$[s_x^2 + \frac{\epsilon_0 - 2w_y^2}{2}]^2 - \frac{(\epsilon_0 - 2w_y^2)^2}{4} - w_y^2\epsilon_0 + \epsilon_i\epsilon_j - \frac{m^2\gamma^2}{\hbar^2}\left|\vec{\sigma}\cdot\vec{B}\right|_{ij}^2 + w_y^4 = 0$$

Thus we find the following poles:

$$s_x = \pm\sqrt{\pm\sqrt{[\frac{\epsilon_i - \epsilon_j}{2}]^2 + \frac{m^2\gamma^2}{\hbar^2}\left|\vec{\sigma}\cdot\vec{B}\right|_{ij}^2} - \frac{\epsilon_0 - 2w_y^2}{2}} \tag{20}$$

And again it is important to note that $i \neq j$. We can see there are four poles in total. Each pole is denoted by p_k. Note that our function Ψ_i can be rewritten in terms of its four poles.

$$\Psi_i = \frac{[s_x^2 - w_y^2 + \epsilon_j][s_x c_i - ik_x d_i] - \frac{m\gamma}{\hbar}[\vec{\sigma}\cdot\vec{B}]_{ij}[s_x c_j - ik_x d_j]}{[s_x - p_1][s_x - p_2][s_x - p_3][s_x - p_4]}\delta(w_y - k_y) \tag{21}$$

Using this information we can work out equation 19:

$$\psi_i(x,\omega_y) = \sum_k \frac{[p_k^2 - w_y^2 + \epsilon_j][p_k c_i - ik_x d_i] - \frac{m\gamma}{\hbar}[\vec{\sigma}\cdot\vec{B}]_{ij}[p_k c_j - ik_x d_j]}{\prod_{n\neq k}[p_k - p_n]}\delta(w_y - k_y)e^{ip_k x} \tag{22}$$

Finally to go from ω_y space back to real space we must do an inverse Fourier transform over ω_y

$$\psi_i(x,y) = \sum_k \frac{[P_k^2 - k_y^2 + \epsilon_j][P_k c_i - ik_x d_i] - \frac{m\gamma}{\hbar}[\vec{\sigma}\cdot\vec{B}]_{ij}[P_k c_j - ik_x d_j]}{\prod_{n\neq k}[P_k - P_n]}e^{iP_k x + ik_y y} \tag{23}$$

With

$$P_k = \pm\sqrt{\pm\sqrt{[\frac{\epsilon_i - \epsilon_j}{2}]^2 + \frac{m^2\gamma^2}{\hbar^2}\left|\vec{\sigma}\cdot\vec{B}\right|_{ij}^2} - \frac{\epsilon_0 - 2k_y^2}{2}} \tag{24}$$

We can see that the solution consists of two forward propagating waves and two backwards propagating waves. Recall that to apply Jordan's lemma we had to assume $x > 0$, therefore the backwards propagating waves are not reflected waves. The kinetic energy of these waves are shifted with respect to the incident wave. To explore the solution further let us assume that $\vec{B}$ is parallel to the z-axis. As a result all non diagonal matrix elements are zero. This simplifies equations 23 and 24 to:

$$P_k = \pm i\sqrt{\mp\frac{\epsilon_i - \epsilon_j}{2} + \frac{\epsilon_0 - 2k_y^2}{2}} = \pm i\sqrt{\epsilon_i - k_y^2} \;\; or \;\; = \pm i\sqrt{\epsilon_j - k_y^2} \tag{25}$$

$$\psi_i(x,y) = \sum_k \frac{[P_k^2 - k_y^2 + \epsilon_j][P_k c_i - ik_x d_i]}{\prod_{n\neq k}[P_k - P_n]}e^{iP_k x + ik_y y} \tag{26}$$

If we look at the forward propagating wave we find:

$$\psi_i(x,y) = \frac{\sqrt{\epsilon_i - k_y^2}c_i + k_x d_i}{2\sqrt{\epsilon_i - k_y^2}} e^{-i\sqrt{\epsilon_i - k_y^2}x + ik_y y} \tag{27}$$

Now we fill in our expression for ϵ_i while noting $E_0 = \frac{\hbar^2(k_x^2+k_y^2)}{2m}$

$$\psi_i(x,y) = \frac{\sqrt{\epsilon_i - k_y^2}c_i + k_x d_i}{2\sqrt{\epsilon_i - k_y^2}} e^{-i\sqrt{k_x^2 + \frac{\gamma m}{\hbar}[\vec{\sigma}\cdot\vec{B}]_{ii}}x + ik_y y} \tag{28}$$

Finally we will find c_i and d_i by applying the proper boundary conditions. To do so we assert that the incident, reflected and transmitted wave are continuous out the boundary:

$$1 + R_i = T_i \tag{29}$$

$$k_x(1 - R_i) = k_i^t T_i \tag{30}$$

with R_i the reflection coefficient, T_i the transmission coefficient and $k_i^t =$ the wavenumber of the transmitted wave. Applying these conditions results in:

$$R_i = \frac{k_x - k_i^t}{k_x + k_i^t} \tag{31}$$

$$T_i = \frac{2k_x}{k_x + k_i^t} \tag{32}$$

So the final expression for our transmitted wavefunction is:

$$\psi_i(x,y) = \frac{2k_x}{k_x + \sqrt{k_x^2 + \frac{\gamma m}{\hbar}[\vec{\sigma}\cdot\vec{B}]_{ii}}} e^{-i\sqrt{k_x^2 + \frac{\gamma m}{\hbar}[\vec{\sigma}\cdot\vec{B}]_{ii}}x + ik_y y} \tag{33}$$

One can see that under high angles (large k_y and small k_x) and high positive magnetic fields the $i = 1$ spin state is transmitted, while the $i = 2$ spin state can only be reflected, as a result magnetic interfaces can be used as polarizing neutron optics [16][17][18]. In our case k_y is almost zero and $k_x >> \frac{\gamma m}{h}B$, thus the transmission amplitude for both spin states is quasi unitary. In addition from these results we learn that upon entering a magnetic field the two neutron spin states will begin to move out of phase (Figure 4) [5]. From a classical perspective this means that one neutron state is slightly faster (due to higher kinetic energy), while the other spin state is slower (lower kinetic energy). This is the well known Stern-Gerlach effect.

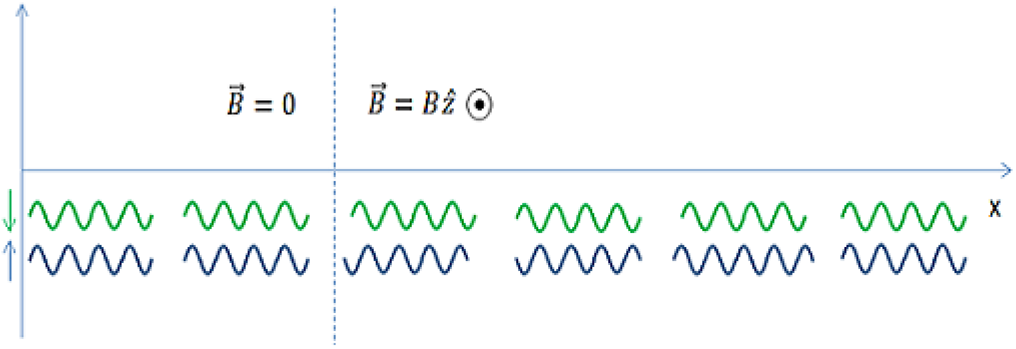

Figure 4. Illustration of the Stern-Gerlach effect using a wave model. The blue (up) spin state propagates faster than the green (down) spin state in a magnetic field causing the two to move out of phase. However due to the monochromicity of the waves they come back into phase every 2π phase shift. This causes patterns of interference.

For small magnetic fields we can linearize the neutron wavenumber:

$$\sqrt{k_x^2 + \frac{\gamma m}{\hbar}[\vec{\sigma} \cdot \vec{B}]_{ii}} = k_x + \frac{\gamma m[\vec{\sigma} \cdot \vec{B}]_{ii}}{2\hbar k_x} + ...$$

And thus the neutron wavefunction simplifies to

$$\psi_i(x, y) \approx e^{-ik_x x - i\frac{\gamma m[\vec{\sigma} \cdot \vec{B}]_{ii}}{2\hbar k_x} x + ik_y y} \tag{34}$$

Now when we look at the expectation value of the spin in the x-direction we find an interesting result:

$$< \sigma_x >= \langle\psi| \hat{\sigma_z} |\psi\rangle = \cos\left(\frac{\gamma m B_z}{\hbar k_x} x\right) = \cos\left(\frac{\gamma B_z}{v_x} x\right) \tag{35}$$

Fringes which correspond to constructive and destructive interference of the two spin states! This phenomenon is known as precession [15]. Of course this perfect sinusoidal interference pattern is only measured for perfectly monochromatic neutrons. In the case of polychromatic neutrons we will demonstrate in a later subsection that the interference pattern takes on a sinc shape. In the next subsection a simpler method for explaining this phenomenon is explored.

2.3 Precession: Neutrons in Homogeneous Static Magnetic Fields in the Time Domain

In this subsection the concept of precession is derived and explained in the time domain [15]. To do so we consider a problem similar the the problem in the previous subsection. Consider a neutron moving through an infinite (in space) static and homogeneous magnetic field. The time dependent Schroedinger equation is then given by

$$i\hbar\frac{\partial}{\partial t}\vec{\psi} = -\frac{\hbar^2}{2m}\nabla^2\vec{\psi} - \frac{\hbar\gamma}{2}[\vec{\sigma} \cdot \vec{B}]\vec{\psi} \tag{36}$$

To solve this equation we switch from the lab frame to the neutron frame. As a result we must move at a velocity v with the neutron. In this case $\nabla^2\vec{\psi} = 0$. However a problem arises from the fact that the two spin states are not moving at the same velocity, this was derived in the previous subsection. However it turns out that for small fields (up to thousands of Tesla) and realistic neutron velocities (order $10^3\frac{m}{s}$) the small contribution from $\nabla^2\vec{\psi} = 0$ can be neglected [19]. In this case equation (36) simplifies to:

$$\frac{\partial}{\partial t}\vec{\psi} = i\frac{\gamma}{2}[\vec{\sigma} \cdot \vec{B}]\vec{\psi} \tag{37}$$

While the ”classical” solution of dividing by $\vec{\psi}$ and integrating on both sides yields the correct result, it is not mathematically rigorous since technically one may not divide by a vector. A more rigorous approach is to use the integrating factor. This results in the following equation:

$$\frac{\partial}{\partial t}[e^{-i\frac{\gamma}{2}\vec{\sigma}\cdot\vec{B}}\vec{\psi}] = 0 \tag{38}$$

Which has the following well known solution:

$$\vec{\psi}(t) = e^{i\frac{\gamma}{2}\vec{\sigma}\cdot\vec{B}t}\vec{\psi}(t=0) \tag{39}$$

The operator

$$e^{i\frac{\gamma}{2}\vec{\sigma}\cdot\vec{B}t} = e^{i\frac{\gamma B}{2}\vec{\sigma}\cdot\hat{n}}$$

is defined by its Taylor series:

$$e^{i\frac{\gamma Bt}{2}\vec{\sigma}\cdot\hat{n}} = I + i\frac{\gamma Bt}{2}\vec{\sigma}\cdot\hat{n} - [\frac{\gamma Bt}{2}]^2 I - i[\frac{\gamma Bt}{2}]^3\vec{\sigma}\cdot\hat{n} + ... \tag{40}$$

Where I is the identity matrix. We used that $[\vec{\sigma}\cdot\hat{n}]^2 = I$, because all Pauli matrices are unitary. One can recognize a cosine and a sine in the Taylor series. Using this allows us to simplify equation 40 [15]:

$$e^{i\frac{\gamma Bt}{2}\vec{\sigma}\cdot\hat{n}} = \cos\left(\frac{\gamma B}{2}t\right)I + i\sin\left(\frac{\gamma B}{2}\right)\vec{\sigma}\cdot\hat{n} \tag{41}$$

Below the operators for $\hat{n} = \hat{x}$, $\hat{n} = \hat{y}$ and $\hat{n} = \hat{z}$ are shown explicitly:

$$e^{i\alpha\sigma_x} = \begin{pmatrix} \cos(\alpha) & i\sin(\alpha) \\ i\sin(\alpha) & \cos(\alpha) \end{pmatrix} \quad e^{i\alpha\sigma_y} = \begin{pmatrix} \cos(\alpha) & \sin(\alpha) \\ -\sin(\alpha) & \cos(\alpha) \end{pmatrix} \quad e^{i\alpha\sigma_z} = \begin{pmatrix} e^{i\alpha} & 0 \\ 0 & e^{-i\alpha} \end{pmatrix} \tag{42}$$

These operators are an important building block for our mathematical understanding of Spin Flippers and MIEZE. But what does it mean? When these act upon a 2D vector (e.g. $\vec{\psi}(t=0)$) they rotate the vector while preserving its length. This means that in the neutrons frame of reference its spin is rotated around the $\hat{n}$ axis, with a frequency of $\omega = \gamma B$ (Figure 5). This phenomenon is known as Larmor Precession [15][19].

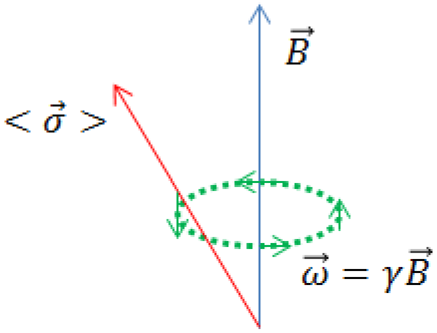

Figure 5. Schematic of Larmor precession. The expectation value of the spin vector $< \vec{\sigma} >$ precesses with a frequency ω around the magnetic field ($\vec{B}$) axis.

2.4 Resonant Radio Frequency Spin Flippers

In the previous subsections the mathematical buildings blocks for neutrons in magnetic fields were derived. In this subsection we look at the first application of said building blocks: the resonant radio frequency spin flipper (or resonant flipper for short). As the name implies this device flips the neutron spin by 180 degrees [4][13][15]. It will soon become apparent that this operation increases the total energy of the neutron. To achieve this the resonant flipper employs a static field B_0 perpendicular to the neutron flight path and a linearly polarized RF field B_{rf} parallel to the the flight path [11]. In mathematical terms the field is given by:

$$\vec{B} = B_0\hat{z} + B_{rf}\cos(\omega t + \phi)\hat{x} \tag{43}$$

We will soon derive that $\omega = \gamma B_0$ is required for a spin flip. Note that by flip we mean that the neutron spin is flipped relative to the static field axis (or the $\hat{z}$ axis). The linearly oscillating field can be written as a superposition of two circularly polarized fields (Figure 6) [20].

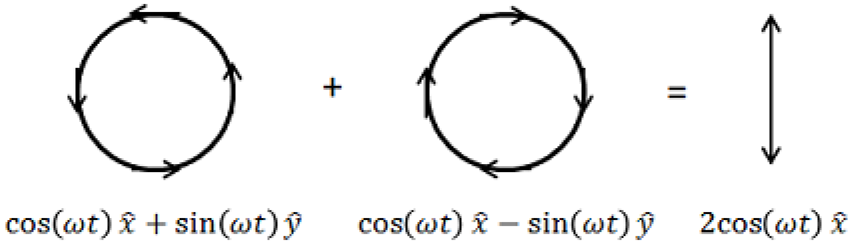

Figure 6. Illustration of superimposing two oppositely rotating magnetic fields. The result is a linearly polarized field.

Thus if we solve the Schroedinger equation for a rotating field and a static field we can solve it for a linearly oscillating field by the principle of superposition. Here we will use an approach similar to the approach used in [13]. We first formulate the problem using the time dependent Schroedinger equation:

$$i\hbar\frac{\partial}{\partial t}\vec{\psi} = -\frac{\hbar^2}{2m}\nabla^2\vec{\psi} - \frac{\hbar\gamma}{2}[\vec{\sigma}\cdot\vec{B}]\vec{\psi} \tag{44}$$

Like in the previous subsection we switch from the lab frame to the neutron frame where $\nabla^2\vec{\psi} = 0$. Then the differential equation simplifies to

$$\frac{\partial}{\partial t}\vec{\psi} = i\frac{\gamma}{2}[B_0\sigma_z + \frac{B_{rf}}{2}(\cos(\omega t + \phi)\sigma_x + \sin(\omega t + \phi)\sigma_y)]\vec{\psi} \tag{45}$$

The keen observer may notice that the term $\cos(\omega t + \phi)\sigma_x + \sin(\omega t + \phi)\sigma_y$ can be rewritten in terms of the spin rotation operators which we derived the in previous section. In terms of these new operators our differential equation reads:

$$\frac{d}{dt}\vec{\psi} = i\frac{\gamma}{2}[B_0\sigma_z + \frac{B_{rf}}{2}\sigma_x e^{i\sigma_z(\omega t + \phi)}]\vec{\psi} \tag{46}$$

Using some commutation relations between the Pauli operators and our rotation operators we can derive the next steps.

$$\frac{d}{dt}\vec{\psi} = i\frac{\gamma}{2}[B_0\sigma_z + \frac{B_{rf}}{2}e^{-\frac{i}{2}\sigma_z(\omega t + \phi)}\sigma_x e^{\frac{i}{2}\sigma_z(\omega t + \phi)}]\vec{\psi} \tag{47}$$

$$\frac{d}{dt}\vec{\psi} = i\frac{\gamma}{2}e^{-\frac{i}{2}\sigma_z(\omega t + \phi)}[B_0\sigma_z + \frac{B_{rf}}{2}\sigma_x]e^{\frac{i}{2}\sigma_z(\omega t + \phi)}\vec{\psi} \tag{48}$$

To further simplify the problem we switch to a frame which rotates with the rotating magnetic field. Such that we can substitute: $\vec{\psi} = e^{-\frac{i}{2}\sigma_z(\omega t+\phi)}\vec{\psi}^r$ Using this substitution is equation 48 results in the following equation.

$$\frac{d}{dt}[e^{-\frac{i}{2}\sigma_z(\omega t+\phi)}\vec{\psi}^r] = i\frac{\gamma}{2}e^{-\frac{i}{2}\sigma_z(\omega t+\phi)}[B_0\sigma_z + \frac{B_{rf}}{2}\sigma_x]\vec{\psi}^r \tag{49}$$

After applying the product rule for differentiation and doing some simple algebra we are left with:

$$\frac{d}{dt}\vec{\psi}^r = i\frac{\gamma}{2}[(B_0 + \frac{\omega}{\gamma})\sigma_z + \frac{B_{rf}}{2}\sigma_x]\vec{\psi}^r \tag{50}$$

Thanks to our work in the previous subsection we know that the solution to this differential equation is given by equation (39). One can see that if $B_0 >> B_{rf}$ the $B_0 + \frac{\omega}{\gamma}$ term will dominate. As a result the neutron spin will not be flipped with respect to the B_0 or $\hat{z}$ axis. Only if $\omega = -\gamma B_0$ will the B_{rf} term dominate. As a result if B_0 is sufficiently large and $\omega = -\gamma B_0$ a linearly oscillating field is equivalent to a circularly polarized field, which rotates in the same direction as the Larmor precession. Let us now explore the case where $\omega = -\gamma B_0$

$$\frac{d}{dt}\vec{\psi}^r = i\frac{\gamma B_{rf}}{4}\sigma_x\vec{\psi}^r \tag{51}$$

This differential equation is solved using equation (39).

$$\vec{\psi}^r = e^{i\frac{\gamma B_{rf}t}{4}\sigma_x}\vec{\psi}^r(t=0) \tag{52}$$

Now we return to the non rotating frame.

$$\vec{\psi} = e^{\frac{i}{2}\sigma_z(\gamma B_0 t-\phi)}e^{i\frac{\gamma B_{rf}t}{4}\sigma_x}e^{\frac{i}{2}\sigma_z\phi}\vec{\psi}(t=0) \tag{53}$$

Next we use a commutation relation to tidy up the result.

$$\vec{\psi} = e^{\frac{i}{2}\sigma_z(\gamma B_0 t-2\phi)}e^{i\frac{\gamma B_{rf}t}{4}\sigma_x}\vec{\psi}(t=0) \tag{54}$$

If the resonant flipper has length d then the time the neutron exits the flipper will be given by $t_f = \frac{d}{v}$. Thus upon exiting the flipper the neutron wavefunction will be given by:

$$\vec{\psi}(t=\frac{d}{v}) = e^{\frac{i}{2}\sigma_z(\gamma B_0\frac{d}{v}-2\phi)}e^{i\frac{\gamma B_{rf}d}{4v}\sigma_x}\vec{\psi}(t=0) \tag{55}$$

A π flip occurs when

$$B_{rf} = \frac{2\pi v}{\gamma d} \tag{56}$$

Note that at a pulse sourced where the flipper is a distance S from the source B_{rf} can be expressed in terms of the time t [11].

$$B_{rf} = \frac{2\pi S}{\gamma dt} \tag{57}$$

with $0 < t < T$, where T is the pulse length. This is an important result for the time of flight methods which require the use of resonant flippers.

When the π flip condition for B_{rf} is satisfied the neutron wavefunction is given by:

$$\psi_i(t = \frac{d}{v}) = e^{\frac{i}{2}\sigma_z^{ii}(\gamma B_0 \frac{d}{v} - 2\phi)} e^{i\frac{\pi}{2}\sigma_x} \psi_i(t = 0) = e^{\frac{i}{2}\sigma_z^{ii}(\gamma B_0 \frac{d}{v} - 2\phi)} \psi_j(t = 0) \tag{58}$$

with $i \neq j$ (note that off diagonal elements are zero). Let us consider an example. A spin up neutron enters a resonant spin flipper which has its static magnetic field oriented parallel to the neutron spin. Upon entering the kinetic energy of this neutron is increased. At the exit of the flipper the neutron spin has been flipped, but its kinetic energy has not been altered. Thus upon leaving the flipper the neutrons kinetic energy increases once again (as it now has spin down). This principle is illustrated in Figure 7 for a neutron which is in a superposition state of both up and down spin [4].

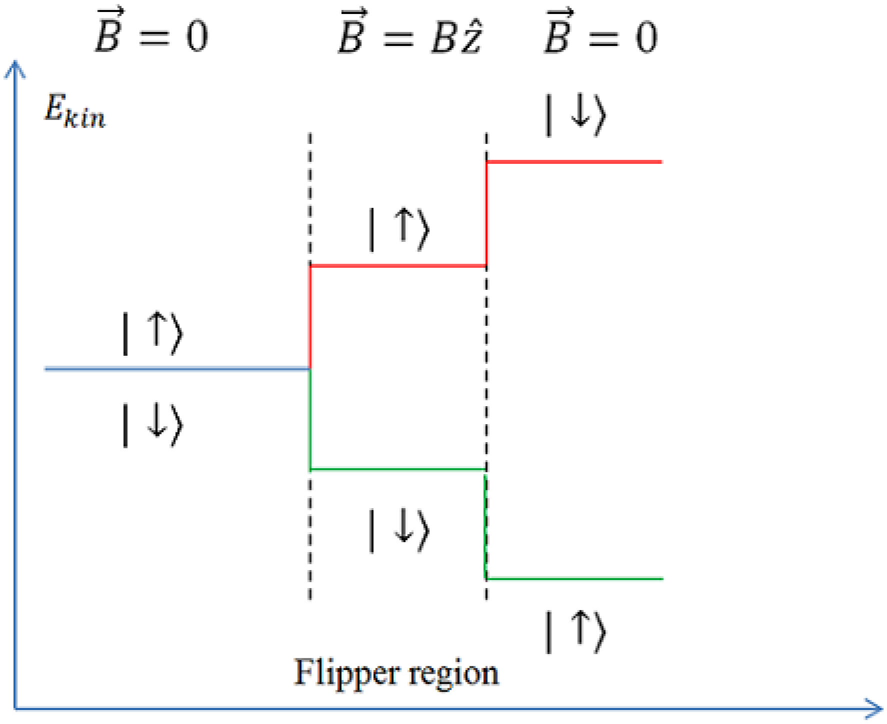

Figure 7. Illustration of the kinetic energy splitting and flipping of the two neutron spin states upon interacting with a resonant spin flipper. The horizontal axis denotes the position along the propagation direction of the neutrons (x-axis), while the vertical axis denotes the kinetic energy.

After having observed Figure 1 in the introduction one should start to recognize various MIEZE building blocks in for example Figure 4 and Figure 7. At the end of this section all of these building blocks should come together to form one complete picture.

2.5 Adiabatic Radio Frequency Spin Flippers

Resonant flippers tend to use air cored coils to generate the static fields. As a result these coils require high currents (20 A in our experiments but can be up to hundreds of amperes [19]). This problem can be alleviated by using pole shoes with a high permeability. For this reason our new flippers utilize pure iron (ARMCO pure iron) pole shoes. This allows us to generate high fields at much lower currents (a few amperes). Thus our novel coils can be used as high field resonant flippers. However our flippers also have a second mode of operation called adiabatic or gradient mode. In this mode, in addition to the static and RF field, a gradient field is superimposed on top of the static field. Furthermore this same gradient field is multiplied with the RF-Field. As a result the RF field amplitude has a sinusoidal shape across the flipper peaking in the center [10]

(Figure 8).

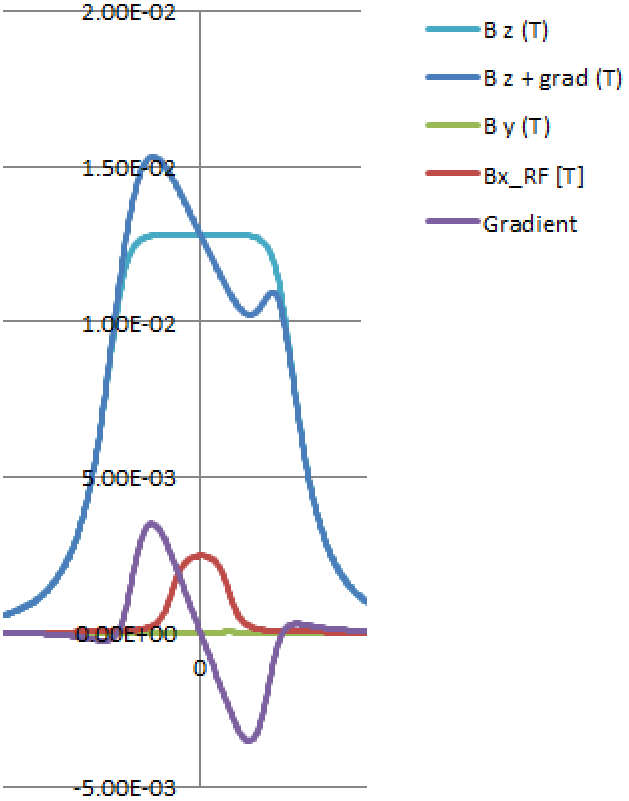

Figure 8. Plot of various fields inside of an adiabatic flipper. On the x-axis the position along the propagation direction is shown, while the y-axis depicts the magnetic flux density in Tesla. The light blue curve denotes the static field, the dark blue curve shows the superposition of the static field with the gradient field, the red curve shows the RF field multiplied by the gradient field and the purple curve depicts the gradient field.

In mathematical terms this field can be described as followed (assuming that the gradient field is one half in strength compared to the RF field):

$$\vec{B} = [B_0 + B_{rf}\cos\left(\frac{\pi x}{d}\right)]\hat{z} + 2B_{rf}\sin\left(\frac{\pi x}{d}\right)\cos(\omega t + \phi)\hat{x} \tag{59}$$

Where d is the flipper length. We can apply the same trick as in the previous subsection where we see the linearly polarized RF field as a superposition of two circularly polarized fields. We can ignore the field that rotates in the opposite direction of the neutron precession. Once again we will insert this field into the Schroedinger equation. The solution is very similar as in the previous subsection, therefore it is inspired by [13].

$$\frac{\partial}{\partial t}\vec{\psi} = i\frac{\gamma}{2}[(B_0 + B_{rf}\cos\left(\frac{\pi x}{d}\right))\sigma_z + B_{rf}\sin\left(\frac{\pi x}{d}\right)\sigma_x e^{i\sigma_z(\omega t+\phi)}]\vec{\psi} \tag{60}$$

We use the same commutation relations as in the previous subsection, also note $x = vt$

$$\frac{\partial}{\partial t}\vec{\psi} = i\frac{\gamma}{2}e^{-\frac{i}{2}\sigma_z(\omega t+\phi)}[(B_0 + B_{rf}\cos\left(\frac{\pi vt}{d}\right))\sigma_z + B_{rf}\sin\left(\frac{\pi vt}{d}\right)\sigma_x]e^{\frac{i}{2}\sigma_z(\omega t+\phi)}\vec{\psi} \tag{61}$$

And we switch to the same rotating frame as in the previous subsection $\vec{\psi} = e^{-\frac{i}{2}\sigma_z(\omega t+\phi)}\vec{\psi}^r$

$$\frac{\partial}{\partial t}[e^{-\frac{i}{2}\sigma_z(\omega t+\phi)}\vec{\psi}^r] = i\frac{\gamma}{2}e^{-\frac{i}{2}\sigma_z(\omega t+\phi)}[(B_0 + B_{rf}\cos\left(\frac{\pi vt}{d}\right))\sigma_z + B_{rf}\sin\left(\frac{\pi vt}{d}\right)\sigma_x]\vec{\psi}^r \tag{62}$$

After application of the product rule and some simple algebra we obtain

$$\frac{\partial}{\partial t}\vec{\psi}^{r} = i\frac{\gamma}{2}[(B_0 + \frac{\omega}{\gamma} + B_{rf}\cos\left(\frac{\pi v t}{d}\right))\sigma_z + B_{rf}\sin\left(\frac{\pi v t}{d}\right)\sigma_x]\vec{\psi}^{r} \tag{63}$$

and we select the resonance condition $\omega = -\gamma B_0$

$$\frac{\partial}{\partial t}\vec{\psi}^{r} = i\frac{\gamma B_{rf}}{2}[\cos\left(\frac{\pi v t}{d}\right))\sigma_z + \sin\left(\frac{\pi v t}{d}\right)\sigma_x]\vec{\psi}^{r} \tag{64}$$

One should recognize yet another circularly polarized field, which rotates from $\hat{z}$ to $\hat{x}$ down to $-\hat{z}$. We can also describe this in terms of our rotation operators (note that a commutation relation is also applied).

$$\frac{d}{dt}\vec{\psi}^{r} = i\frac{\gamma B_{rf}}{2}e^{i\sigma_y \frac{\pi v}{2d}t}\sigma_z e^{-i\sigma_y \frac{\pi v}{2d}t}\vec{\psi}^{r} \tag{65}$$

Next we enter a second rotating frame such that $\vec{\psi}^{r} = e^{\frac{i}{2}\frac{\pi v}{2d}\sigma_y t}\vec{\psi}^{rr}$

$$\frac{d}{dt}[e^{\frac{i}{2}\frac{\pi v}{2d}\sigma_y t}\vec{\psi}^{rr}] = i\frac{\gamma B_{rf}}{2}e^{i\sigma_y \frac{\pi v}{2d}t}\sigma_z\vec{\psi}^{rr} \tag{66}$$

Once again we apply the product rule of differentiation and obtain

$$\frac{d}{dt}\vec{\psi}^{rr} = i[\frac{\gamma B_{rf}}{2}\sigma_z - \frac{\pi v}{2d}\sigma_y]\vec{\psi}^{rr} \tag{67}$$

Which is solved by equation (39)

$$\vec{\psi}^{rr} = e^{i[\frac{\gamma B_{rf}}{2}\sigma_z - \frac{\pi v}{2d}\sigma_y]t}\vec{\psi}^{rr}(t=0) \tag{68}$$

Finally we return to the original frame.

$$\vec{\psi} = e^{\frac{i}{2}\sigma_z(\gamma B_0 t - \phi)}e^{-\frac{\pi v}{2d}\sigma_y t}e^{i[\frac{\gamma B_{rf}}{2}\sigma_z - \frac{\pi v}{2d}\sigma_y]t}e^{-\frac{i}{2}\phi\sigma_z}\vec{\psi}(t=0) \tag{69}$$

This wavefunction becomes a lot simpler if we assume that $\gamma B_{rf} >> \frac{\pi v}{2d}$

$$\vec{\psi} = e^{\frac{i}{2}\sigma_z(\gamma B_0 t - \gamma B_{rf} t - 2\phi)}e^{-\frac{\pi v}{2d}\sigma_y t}\vec{\psi}(t=0) \tag{70}$$

One can see that the π flip condition is given by $t = \frac{d}{v}$, which means that any neutron independent of its velocity will have its spin flipped by the time it leaves an adiabatic flipper. At this point the wavefunction is given by:

$$\psi_i = e^{\frac{i}{2}\sigma_z^{ii}(\gamma B_0 \frac{d}{v} - \gamma B_{rf}\frac{d}{v} - 2\phi)}\psi_j(t=0) \tag{71}$$

with $i \neq j$ Thus unlike the resonant flippers these adiabatic flippers will flip neutrons of all wavelengths, without the need to change the RF field during the pulse. This makes these flippers not only suitable for pulsed sources, but also for continuous sources. As stated above our novel flippers can be utilized in both adiabatic and resonant mode. Why resonant mode is sometimes preferable is discussed in the method section. We have now derived all the buildings blocks necessary to understand MIEZE. Thus in the next section we will take a theoretical look at a MIEZE setup and describe the evolution of the neutron wavefunction within the instrument.

2.6 Evolution of the Neutron Wavefunction Within a MIEZE Instrument and the MIEZE Focusing Condition

In this subsection the MIEZE focusing condition is derived by calculating the evolution of a neutron wavefunction inside of a MIEZE instrument. This so called plane wave approach was first explored by Golub and Gaehler in 1994 [4]. However since our setup also utilizes a guide field we must take this into account as well. This guide field concept is not entirely new as it is applied in a similar manner in the MICE technique [21]. The general setup is shown below in Figure 9.

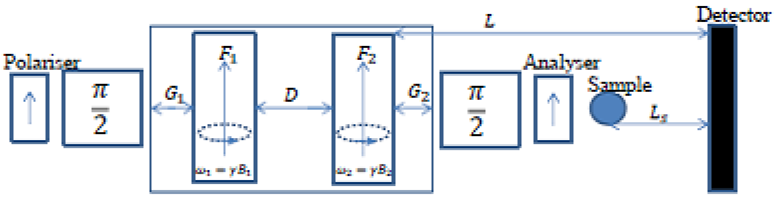

Figure 9. Side view of our MIEZE setup. The flippers F_1 and F_2 are contained inside of a guide field. The guide field is parallel to the static field of the two flippers. The first $\frac{\pi}{2}$ rotator prepares the spin up neutrons coming from the polarizer in a superposition of the up and down spin state. The second $\frac{\pi}{2}$ flipper ensures that we measure in the correct basis.

In these calculations we will ignore the $\frac{\pi}{2}$ rotators, as they are not necesarry for our theoretical understanding of MIEZE. In addition we will assume that the flippers are resonant flippers, however it turns out that adiabatic flippers yield exactly the same result, if the gradient field in both flippers are equal. Further more we assume that the neutron will enter the guide field in an equal superposition of both spin states. Finally we will assume that there are no reflections, that is the transmission coefficient is equal to one.
When the neutron enters the guide field the wavevector is changed according to equation (33).

$$\psi_i(x) = e^{-i\sqrt{k_x^2+\frac{\gamma m}{\hbar}\sigma_z^{ii}B_g}x}\psi_i^0 \tag{72}$$

Where B_g is the magnetic flux density of the guide field and ψ_i^0 denotes the amplitude of the i-th spin state. Upon entering the first flipper the wavefunction changes again according to equation (33)

$$\psi_i(x) = e^{-i\sqrt{k_x^2+\frac{\gamma m}{\hbar}\sigma_z^{ii}B_g}G_1-i\sqrt{k_x^2+\frac{\gamma m}{\hbar}\sigma_z^{ii}B_1}x}\psi_i^0 \tag{73}$$

with B_1 the static field in the first flipper. Next the neutron experiences a spin flip, which is described by equation 58

$$\psi_i(x) = e^{\frac{i}{2}\sigma_z^{ii}(\gamma B_1\frac{d}{v}-2\phi_1)}e^{-i\sqrt{k_x^2-\frac{\gamma m}{\hbar}\sigma_z^{ii}B_g}G_1-i\sqrt{k_x^2-\frac{\gamma m}{\hbar}\sigma_z^{ii}B_1}x}\psi_j^0 \tag{74}$$

The expressions for the various phases will start to get long, so we will shorten them using the symbol χ_i. Upon leaving the flipper the kinetic energy contribution from the static magnetic field is doubled as it was explained in Figure 7. However the guide field slightly perturbs this.

$$\psi_i(x) = e^{\frac{i}{2}\sigma_z^{ii}(\gamma B_1\frac{d}{v}-2\phi_1)}e^{-i\chi_1-i\sqrt{k_x^2-\frac{\gamma m}{\hbar}\sigma_z^{ii}[2B_1-B_g]}x}\psi_j^0 \tag{75}$$

The neutron now traverses the distance D and enters the second spin flipper. At this point the wavefunction is given by

$$\psi_i(x) = e^{\frac{i}{2}\sigma_z^{ii}(\gamma B_1\frac{d}{v}-2\phi_1)}e^{-i\chi_1-i\sqrt{k_x^2-\frac{\gamma m}{\hbar}\sigma_z^{ii}[2B_1-B_g]}D-i\sqrt{k_x^2+\frac{\gamma m}{\hbar}\sigma_z^{ii}[B_2-2B_1]}x}\psi_j^0 \tag{76}$$

Once again the neutron spin is flipped by the spin flipper leading to the following wavefunction

$$\psi_i(x) = e^{\frac{i}{2}\sigma_z^{ii}(\gamma(B_2-B_1)\frac{d}{v}+2[\phi_1-\phi_2])}e^{-i\chi_1-i\chi_2-i\sqrt{k_x^2-\frac{\gamma m}{\hbar}\sigma_z^{ii}[B_2-2B_1]}x}\psi_i^0 \tag{77}$$

With

$$\chi_1 = \sqrt{k_x^2 + \frac{\gamma m}{\hbar}\sigma_z^{ii} B_g} G_1$$

$$\chi_2 = \sqrt{k_x^2 + \frac{\gamma m}{\hbar}\sigma_z^{ii}[2B_1 - B_g]} D$$

Now the neutron leaves the flipper again

$$\psi_i(x) = e^{\frac{i}{2}\sigma_z^{ii}(\gamma(B_2-B_1)\frac{d}{v}+2[\phi_1-\phi_2])} e^{-i\chi_1-i\chi_2-i\sqrt{k_x^2-\frac{\gamma m}{\hbar}\sigma_z^{ii}[2B_2-2B_1+B_g]}x}\psi_i^0 \tag{78}$$

Finally we reach the end of the guide field and enter a zero field region, where the wavefunction is given by

$$\psi_i(x) = e^{\frac{i}{2}\sigma_z^{ii}(\gamma(B_2-B_1)\frac{d}{v}+2[\phi_1-\phi_2])} e^{-i\chi_1-i\chi_2-i\chi_3-i\sqrt{k_x^2-\frac{\gamma m}{\hbar}\sigma_z^{ii}[2B_2-2B_1]}x}\psi_i^0 \tag{79}$$

With

$$\chi_3 = \sqrt{k_x^2 - \frac{\gamma m}{\hbar}\sigma_z^{ii}[2B_2 - 2B_1 + B_g]} G_2$$

The focus is at the point where all k_x dependent phase shifts are zero. This can only be obtained in first order [4]. Thus we will linearize all wavevectors using

$$\sqrt{k_x^2 + \kappa} = k_x + \frac{\kappa}{2k_x} + ... \tag{80}$$

and we will express k_x in terms of the neutron velocity:

$$k_x = \frac{mv}{\hbar} \tag{81}$$

Note also that ϕ_1 and ϕ_2 simply denote the phase of the RF field at the time the neutron enters the respective flipper, thus $\phi_1 = \omega_1 t$ and $\phi_2 = \omega_2[t+\Delta t]$. These substitutions lead to the following first order approximation of the wavefunction

$$\psi_i = e^{\frac{i}{2}\sigma_z^{ii}(\Delta\omega\frac{d}{v}+2\Delta\omega t)} e^{-ik_x[x+L_t]+\sigma_z^{ii}\frac{i}{2v}[-2\Delta\omega x+(\omega_g-2\Delta\omega)G_2+(2\omega_1-\omega_g)D+\omega_g G_1]}\psi_i^0 \tag{82}$$

Where we used that $\gamma B = \omega$ and $\omega_2 - \omega_1 = \Delta\omega$. In addition we ignored the arbitrary and constant phase $\omega_2\Delta t$. Next it is helpful to calculate the expectation value of the spin in the x-direction.

$$< \sigma_x >= \cos\left(2\Delta\omega t + \frac{1}{v}[-2\Delta\omega x + 2\omega_1 D + \Delta\omega d - 2\Delta\omega G_2 + \omega_g[G_1 + G_2 - D]]\right) \tag{83}$$

Thus to have no velocity dependent phase shift we must satisfy the following focusing condition

$$-2\Delta\omega x + 2\omega_1 D + \Delta\omega d - 2\Delta\omega G_2 + \omega_g[G_1 + G_2 - D] = 0 \tag{84}$$

Therefore the focusing condition is given by

$$x = L = \frac{2\omega_1 D + \omega_g[G_1 + G_2 - D]}{2\Delta\omega} + \frac{d}{2} - G_2 \tag{85}$$

This distance is measured from the edge of the guide field. If we wish to know the focusing condition from the edge of the last flipper we must add G_2

$$L = \frac{2\omega_1 D + \omega_g[G_1 + G_2 - D]}{2\Delta\omega} + \frac{d}{2} \tag{86}$$

We can check a special case where $\omega_g = 0$

$$L = \frac{D}{\frac{\omega_2}{\omega_1} - 1} + \frac{d}{2} \tag{87}$$

Which is in agreement with the focusing condition for zero guide field found in 1994 [4]. Once the focusing condition is satisfied equation (83) becomes a simple cosine.

$$< \sigma_x >= \cos(2\Delta\omega t) \tag{88}$$

Thus at the focal point the neutron polarization along the x-direction is modulated in time, with a modulation frequency of

$$\omega_m = 2\Delta\omega = 2(\omega_2 - \omega_1) \tag{89}$$

A final point of discussion is the poorly aligned setup, that is, what happens if the detector is moved a distance ΔL out of focus. In this case $< \sigma_x >$ will be given by

$$< \sigma_x >= \cos\left(2\Delta\omega[t - \frac{\Delta L}{v}]\right) = \cos\left(2\Delta\omega(t - \frac{m\lambda\Delta L}{h})\right) \tag{90}$$

Which would be fine if the neutrons are perfectly monochromatic, but this is never the case, thus we must average over the bandwidth $\Delta\lambda$ (in first order this is a good approximation).

$$< \sigma_x >= \int_{\lambda_0 - \frac{\Delta\lambda}{2}}^{\lambda_0 + \frac{\Delta\lambda}{2}} \cos\left(2\Delta\omega(t - \frac{m\lambda\Delta L}{h})\right) d\lambda \tag{91}$$

Which is really just a phase shifted cosine transform. The result is given by a sinc function.

$$< \sigma_x >= sinc(\frac{\Delta\omega\Delta L m\Delta\lambda}{h}) \cos\left(2\Delta\omega[t - \frac{m\Delta L\lambda_0}{h}]\right) \tag{92}$$

In time of flight $\lambda_0 = \frac{h}{mL}t$, thus our cosine experiences a frequency shift [22].

$$< \sigma_x >= sinc(\frac{\Delta\omega\Delta L m\Delta\lambda}{h}) \cos\left(2\Delta\omega[1 - \frac{\Delta L}{L}]t\right) \tag{93}$$

This is a very useful tool as the MIEZE frequency we measure will tell us exactly how far out of focus we are and in which direction we must move the detector. One can also see the importance of a good wavelength resolution, as a bad wavelength resolution increases the sensitivity of the MIEZE instrument to misalignment.

2.7 MIEZE Measurements and Resolution

MIEZE measurements are discussed and the resolution of MIEZE spectrometers is derived in this subsection. A MIEZE spectrometer measures energy transfers between the sample and the incident neutrons. When such an inelastic scattering event takes place the neutron velocity is changed. As a result the two spin states will not arrive at the detector at the same time, causing the amplitude of the polarization modulation to drop. Thus this drop in polarization is a measure for the energy transfer between sample and neutron. This amplitude drop and the resolution of a MIEZE spectrometer can be derived using the expectation value for the neutron spin in the x-direction. We will regard this modulated polarization as a quantum mechanical quasi particle which scatters on the sample at a distance L_s from the detector. This quasi particle splits into two partial waves. One partial wave experiences a positive energy transfer, while the other experiences the opposite energy transfer. This method is motivated by a method used for grating interferometers [23]. The expectation value of the neutron spin in the x-direction after an inelastic scattering event is given by:

$$< \sigma_x >= \frac{1}{2}\cos(2\Delta\omega t + \phi(dv)) + \frac{1}{2}\cos(2\Delta\omega t + \phi(-dv)) \tag{94}$$

Where the time independent phase $\phi(dv)$ is given by;

$$\phi = \frac{1}{v}[-2\Delta\omega[L - L_s] + 2\omega_1 D + \Delta\omega d - 2\Delta\omega G_2 + \omega_g[G_1 + G_2 - D]] - \frac{2\Delta\omega L_s}{v + dv} \tag{95}$$

Which we can simplify using the focusing condition

$$\phi = \frac{2\Delta\omega L_s}{v} - \frac{2\Delta\omega L_s}{v + dv} = \frac{2\Delta\omega L_s dv}{v^2 + vdv} \tag{96}$$

Thus the neutron spin in the x-direction is given by

$$< \sigma_x >= \frac{1}{2}\cos\left(2\Delta\omega[t + \frac{L_s dv}{v^2 + vdv}]\right) + \frac{1}{2}\cos\left(2\Delta\omega[t - \frac{L_s dv}{v^2 - vdv}]\right) \tag{97}$$

To further simplify this expression we must first do some algebra:

$$< \sigma_x >= \frac{1}{2}\cos\left(2\Delta\omega[t + \frac{L_s(v - dv)}{v^2 - dv^2}\frac{dv}{v}]\right) + \frac{1}{2}\cos\left(2\Delta\omega[t - \frac{L_s(v + dv)}{v^2 - dv^2}\frac{dv}{v}]\right) \tag{98}$$

Which can be simplified by using the following trigonometric relation

$$\cos(\omega t + \phi + \theta) + \cos(\omega t + \phi - \theta) = 2\cos(\theta)\cos(\omega t + \phi) \tag{99}$$

giving us

$$< \sigma_x >= cos(2\Delta\omega\frac{L_s dv}{(v^2 - dv^2)})\cos\left(2\Delta\omega[t + \frac{L_s dv^2}{v(v^2 - dv^2)}]\right) \tag{100}$$

This is the exact solution which holds for all energy transfers. One can see that high energy transfers will shift the MIEZE frequency slightly (as v is dependent on t at a pulsed source). However MIEZE is limited at high energy transfers due to aliasing effects: the MIEZE amplitude will drop for small energy transfers but will start to rise again for very large energy transfers. Usually MIEZE is pitched as a high resolution interferometer [5][24], so let us simplify equation (100) for the case where $v >> dv$

$$< \sigma_x >= \cos\left(2\Delta\omega\frac{L_s dv}{v^2}\right)\cos(2\Delta\omega t) \tag{101}$$

Now we would like to express dv in terms of the energy transfer $\hbar\omega$. Let us first express $\hbar\omega$ as the difference between the final neutron energy and the incident neutron energy.

$$\hbar\omega = \frac{1}{2}m[(v_1 \pm dv)^2 - v_1^2] = \frac{m}{2}[\pm 2dvv_1 + dv^2]$$

Since we are looking at small changes in neutron velocity first order effects will dominate, hence $dv^2 \approx 0$

$$dv = \pm\frac{\hbar\omega}{mv_1}$$

If we apply this finding to equation (101) and use $v = \frac{\hbar k}{m}$ we find the following:

$$< \sigma_x >= \cos\left(2\Delta\omega\frac{m^2 L_s\omega}{\hbar^2 k^3}\right)\cos(2\Delta\omega t) \tag{102}$$

Thus the amplitude reduction is dependent on the energy transfer and an instrument parameter, which is called the spin echo time or Fourier time:

$$\tau = \frac{2\Delta\omega m^2}{\hbar^2 k^3}L_s \tag{103}$$

Due to the periodic nature of the cosine, the argument of the cosine $\omega\tau$, should also be smaller than or equal to π. This means that the maximum τ determines the energy resolution as followed:

$$\Delta E_{min} = \frac{h}{2\tau_{max}} \tag{104}$$

which is equivalent to the well known Nyquist criterion. In the high energy limit where $dv \to v$ we must be careful, with how we choose $\Delta\omega$, but in principle, measuring such higher energy transfers should be possible.

We looked at the amplitude drop for a single symmetric energy transfer. If we have multiple such energy transfers, we must average over each transfer. This yields a cosine transform [14]. Thus the ratio between the beam polarization with and without sample yields the following amplitude term:

$$\frac{P}{P_0} = \int S(q,\omega)\cos(\omega\tau)d\omega = \hat{s}(q,\tau) \tag{105}$$

Where $S(q,\omega)$ is the scattering function, or dynamic structure factor. It is a distribution function which describes the relative occurrence of a certain energy transfer at a certain scattering vector q. $\hat{s}(q,\tau)$ is called the intermediate scattering function and is the cosine transform of the scattering function [14]. One should not forget to average over the velocity v in a real experiment, as the beam is never truly monochromatic.

2.8 The Intermediate Scattering Function for Liquids in the Low Energy Limit

To derive the so called scattering function we will make use of Fermi's golden rule which is valid for weak scattering, since it is based on the first order Born approximation. The scattering function simply scales with the transition rate given by Fermi's golden rule [25][26]:

$$\Gamma_{if} = \frac{2\pi}{\hbar}|\langle f|\hat{V}|i\rangle|^2\delta(E_i - E_f + \hbar\omega) \tag{106}$$

Where i denotes the initial state and f denotes the final state (note that these states are a tensor product of the sample s and neutron states ψ). To solve this we must find the scattering potential $\hat{V}$. For $\hat{V}$ we usually pick the Fermi pseudo potential.

$$\hat{V} = \sum_j C_j\delta(r - R_j) \tag{107}$$

Thus we can calculate the matrix elements, assuming that the initial and final neutron states can be described as plane waves

$$|\sum_j C_j \langle s_f| \langle\psi_f|\delta(r - R_j)|\psi_i\rangle |s_i\rangle|^2 = |\sum_j C_j \langle s_f| \int e^{i\vec{q}\cdot\vec{r}}\delta(\vec{r} - \vec{R}_j)dr\,|s_i\rangle|^2 \tag{108}$$

with $\vec{q} = \vec{k}_f - \vec{k}_i$ the scattering vector. This can be further simplified using the properties of the delta function

$$|\sum_j C_j \langle s_f| e^{i\vec{q}\cdot\vec{R}_j}|s_i\rangle|^2 = \sum_{j,j'} C_jC_{j'}\langle s_f|e^{i\vec{q}\cdot\vec{R}_j}|s_i\rangle\langle s_i|e^{-i\vec{q}\cdot\vec{R}_{j'}}|s_f\rangle \tag{109}$$

We are now ready to insert this expression into equation 106. We will also use the Fourier transform to express the delta function (ignoring normalization)

$$\Gamma_{if} \propto \int \sum_{j,j'} C_jC_{j'}\langle s_f|e^{i\vec{q}\cdot\vec{R}_j}|s_i\rangle\langle s_i|e^{-i\vec{q}\cdot\vec{R}_{j'}}|s_f\rangle e^{i\frac{(E_f - E_i)t}{\hbar}}e^{-i\omega t}dt \tag{110}$$

We will now use the following equivalence

$$e^{i\hat{H}t}\left|s\right\rangle = \left|s\right\rangle e^{iEt}$$

If we assume that $\hat{H}$ is constant in time we can use the above relation as the time evolution operators, such that

$$R(t) = e^{\frac{i}{\hbar}\hat{H}t} R e^{-\frac{i}{\hbar}\hat{H}t}$$

With $R(0) = R$ Using these relationships we can simplify equation (110) to the following

$$\Gamma_{if} \propto \int \sum_{j,j'} C_j C_{j'} \left\langle s_f\right| e^{i\vec{q}\cdot\vec{R}_j(t)} \left|s_i\right\rangle \left\langle s_i\right| e^{-i\vec{q}\cdot\vec{R}_{j'}(0)} \left|s_f\right\rangle e^{-i\omega t} dt \tag{111}$$

Finally we sum over all final states using $\sum \left|s_f\right\rangle \left\langle s_f\right| = 1$ and we must sum over all initial states and weigh them appropriately. This results in the so called thermal average of an operator $\sum_i p_i \left\langle s_i\right| \hat{A} \left|s_i\right\rangle =< A >$. In our case that leads to a correlation function [25].

$$S(q,\omega) \propto \int \sum_{j,j'} C_j C_{j'} < e^{i\vec{q}\cdot\vec{R}_j(t)} e^{-i\vec{q}\cdot\vec{R}_{j'}(0)} > e^{-i\omega t} dt \tag{112}$$

Recall that with MIEZE we measure the cosine transform of the scattering function, which is also the real part of the Fourier transform. This is rather convenient because equation (112) is a Fourier transform. Thus the intermediate scattering function measured by MIEZE is given by:

$$S(q,\tau) \propto Re[\sum_{j,j'} C_j C_{j'} < e^{i\vec{q}\cdot[\vec{R}_j(t) - \vec{R}_{j'}(0)]} >] \tag{113}$$

As a next simplification we may assume that correlations between various particles are very small, therefore we say $i = j$

$$S(q,\tau) \propto Re[\sum_{j} C_j^2 < e^{i\vec{q}\cdot[\vec{R}_j(t) - \vec{R}_j(0)]} >] \tag{114}$$

When we look at a single particle we may drop the summation, also for convenience we will set C_j to one. We also regard only small angles such that $\vec{q}\cdot\vec{r} = qr$

$$S(q,\tau) \propto Re[\left\langle s_i\right| e^{iq[R(t)-R(0)]} \left|s_i\right\rangle] \tag{115}$$

Recall that $\langle s_i|s_i\rangle$ is simply the probability density function of finding the particle at a certain position at a time t. In thermal equilibrium in the diffusive limit this PDF is well described by a Gaussian function. Thus we find that our intermediate scattering function is the Fourier transform of a Gaussian [27].

$$S(q,\tau) \propto Re[\int_{-\infty}^{\infty} G(r,\tau) e^{iqr} dr] = G(q,\tau) \tag{116}$$

Where $G(q,\tau)$ can be derived from the heat equation [27] yielding

$$S(q,\tau) = e^{-Dq^2\tau} \tag{117}$$

with D the diffusion coefficient. Recall that this is only valid in the case where scattering angles are small and we disregard particle particle interaction. Our result has been confirmed for liquids such as water numerous times in literature [27][28][29]. A correction can be found in [28][30] called the random jump model, which is valid also for slightly larger angles. The correction is given by:

$$S(q,\tau) = e^{-\frac{Dq^2}{1+Dq^2\tau_0}\tau} \tag{118}$$

with τ_0 a material constant.

3 Method

As mentioned in the introduction we wish to demonstrate the feasibility of applying our high field spin flippers to MIEZE. To achieve this we construct a conventional MIEZE setup which utilizes two bootstrapped resonant spin flippers contained inside of a zero field chamber and an experimental MIEZE setup which employs our novel spin flippers inside of a guide field. Finally the results from each setup are compared. In the first subsection of this chapter a few experimental concepts are explained. In the following two subsections our resonant and novel spin flippers are described and characterized. In the next subsection the utilized detector technology is discussed and its limitations explored. In the following two subsections the conventional setup (using resonant flippers) and the experimental setup are shown. In the final subsection we take a look at the data extraction and processing methods.

3.1 Experimental Concepts

In this subsection a few experimental concepts are explained, which were not necessary to understand the theory. In particular we will explore Time of Flight (ToF), visibility and v-coils/$\frac{\pi}{2}$ rotators.

3.1.1 Time of Flight

Time of Flight (ToF) refers to the fact that the neutron flight time encodes the neutron wavelength at pulsed sources [20]. This is due to the fact that wavelength and velocity are related in quantum mechanics.

$$v = \frac{h}{m\lambda} \tag{119}$$

Thus the wavelength is given by

$$\lambda = \frac{ht}{mL} \tag{120}$$

with L the distance from the pulsed source and $0 < t < T$ where T is the pulse length. A TU Delft we have a continuous source, however one can turn the continuous beam into a pulsed beam by employing a double disk chopper [31] (Figure 10). The chopper used in these experiments consists of two disks on an axis. Each disk has two small cuts cut into them, which are slightly phase shifted. The maximum rotation speed of our chopper is 25Hz which leads to a pulse frequency of 50Hz. The disks can be moved closer together to increase the wavelength resolution of the device at the cost of a decreased neutron flux. This resolution is given by [32]

$$\frac{\Delta\lambda}{\lambda} = \frac{\Delta t}{t} = \frac{D}{L} \tag{121}$$

where D is the distance between the two disks and L the distance from the center of the chopper to the detector. The chopper emits an optical pulse 90 degrees before the openings pass in front of the beam. This optical pulse can be used as a reference to start the detector and other components.

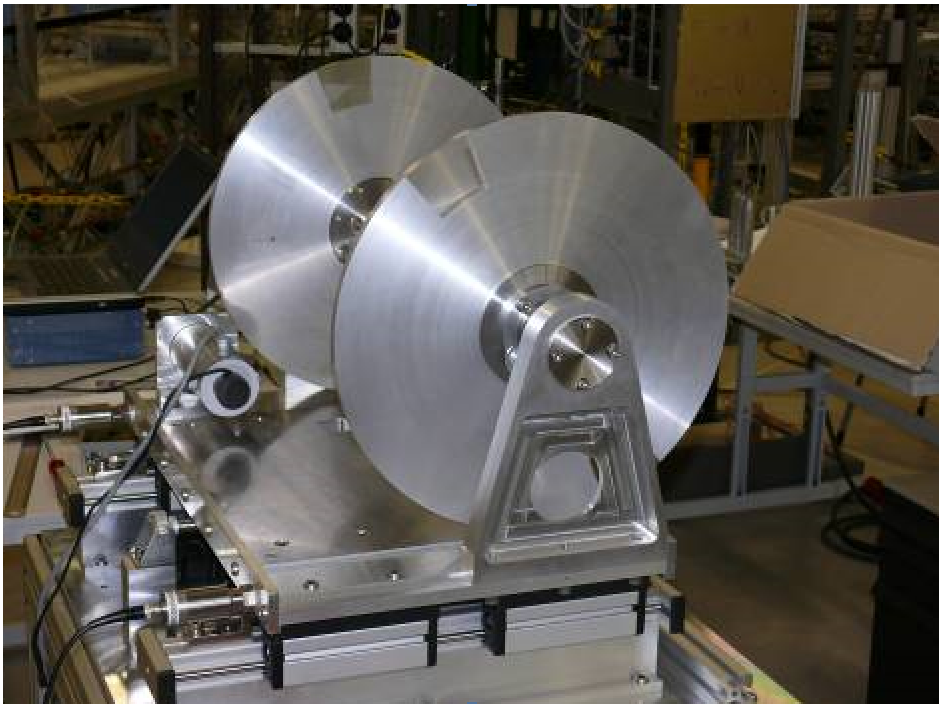

Figure 10. Picture of the chopper used for our experiments. This picture was taken by Demo at TU Delft.

3.1.2 Visibility

In the theory section we often referred to the expectation value of σ_x, however it was never addressed how one measures this quantity. One does this by measuring the intensity of the projection of the neutron spins on the $+x$ axis, I_+ and the projection on the $-x$ axis, I_-. This allows one to calculate the polarization along the x-axis $< \sigma_x >$ or the Visibility [15][20].

$$P = \frac{I_+ - I_-}{I_+ + I_-} \tag{122}$$

We define I_- as the neutron intensity measured by the MIEZE instrument when a beam flipper is placed in front of the instrument. Therefore I_+ is the intensity measured when the beam flipper is disabled. The definition is arbitrary, but once chosen one must be consistent.

3.1.3 $\frac{\pi}{2}$ Rotators and V-Coils

Previously $\frac{\pi}{2}$ rotators were introduced as a means to prepare a neutron in a superposition between up and down state and a way to measure the polarization in the x-basis. To facilitate this we employ steel tubes lined with magnets. These magnets are displaced with respect to each other along the circumference and the length of the tube. As a result the magnetic field inside the tube rotates adiabatically from the z direction at one side of the tube to the x direction at the other side of the tube. On the side where the field points in the x direction we place a v-coil. This device consists out of a mu-metal box and a specially wound coil. This results in a progressively increasing field in the x-direction as one moves along the v-coil. At the end of the coil there is a current sheet which causes the field to drop to zero diabaticaly [33] (Figure 11). The combination of v-coil and the steel tube results in a spin flipped by $\frac{\pi}{2}$ with respect to the z-axis.

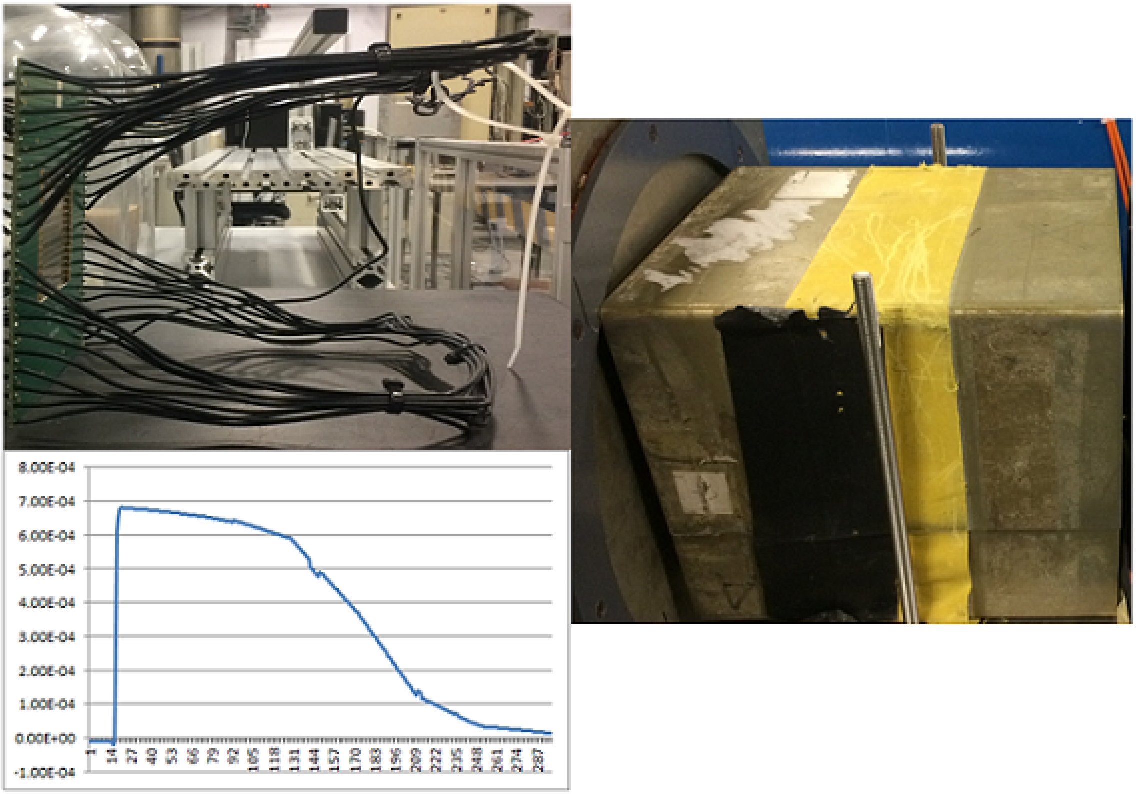

Figure 11. A picture of a v-coil without shielding (top left) a graph of the magnetic field inside of the device (bottom left) (the y-axis denotes the field strength in Tesla and the x-axis denotes the neutron position along the beamline) and a picture of a v-coil with mu-metal shielding (right).

3.2 Resonant Radio Frequency Spin Flippers

The resonant flippers used for our experiments (Figure 12) were originally constructed for the FLEXX instrument at Helmholtz-Zentrum-Berlin (HZB) [34]. These flippers are in a bootstrapped pair configuration. This means that each flipper actually consists of two flippers with anti-parallel static fields. As a result the energy splitting effect demonstrated in section 2.4 is doubled. Thus we can treat a bootstrapped resonant flipper as a single flipper running at twice the frequency and field [35].

Each flipper has a total of 5 electrical connections, one for the static coils (the coils are placed in series), two for the resonant coils and two for pickup coils which measure the oscillating RF field. Each flipper also has 3 cooling connections, one for compressed air and the other two for water (inlet and outlet). The compressed air exits around the neutron entry and exit windows. Each flipper within the bootstrap pair has a length of 4cm.

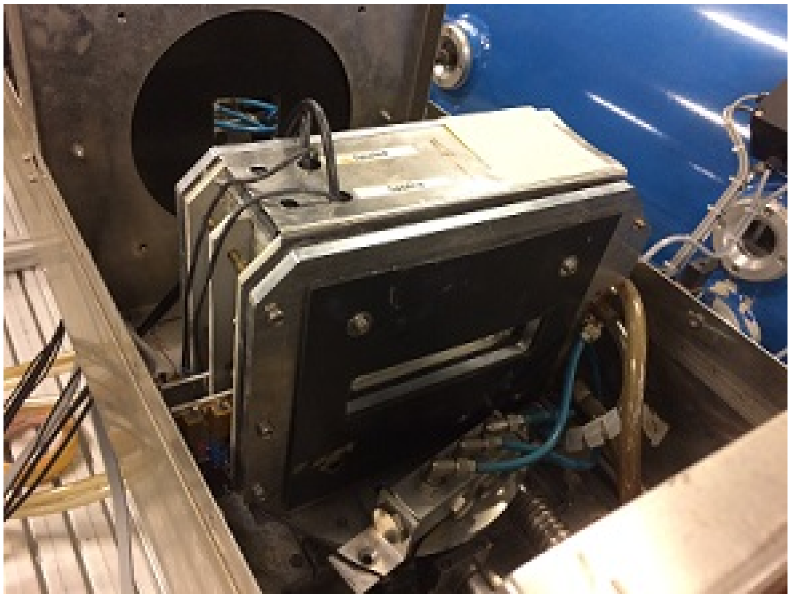

Figure 12. Picture of the bootstrap pair resonant flippers mounted in a zero field chamber.

By removing the top piece of a resonant flipper one can insert a Gauss probe to measure the static magnetic field strength as a function of the current in the coil. The following linear I-B response was measured.

$$B = 3.1 \cdot 10^{-4} I \tag{123}$$

As described in section 2.4 resonant flippers will only perform a π flip for one neutron wavelength if the amplitude of the RF field is constant, equation (56). However equation (57) demonstrates that one can modulate the RF field using a $1/t$ function in time of flight (section 3.1.1) to obtain a π flip for all wavelengths. This can create problems at small t because $1/t$ functions are not bounded. To resolve this we pick a starting wavelengths (in our case 1.8Å) and set the RF field to zero for times smaller than the time when the 1.8Å neutrons arrive [11]. Figure 13 shows a typical RF waveform which is fed to the flipper. This waveform is generated using a Matlab script (see appendix) and a function generator, it is then amplified by an RF amplifier and sent into the RF coil. The function generator generates the waveform as soon as it receives a pulse from the chopper. Said waveform is only generated once per chopper pulse.

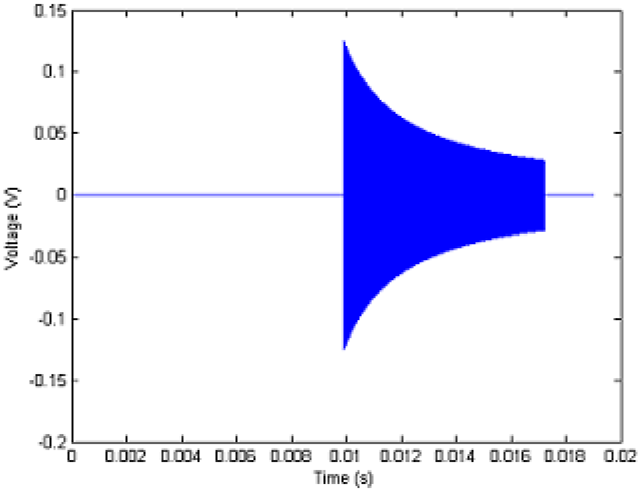

Figure 13. Graph of the waveform which is sent to the RF coil of a spin flipper.

The flipper is operated by selecting a certain static field and frequency ($\omega = \gamma B$) and tuning the RF field such that the flipped beam polarization is as close as possible to the non flipped beam polarization is magnitude. Recall that our resonant flippers are a bootstrapped pair. This means we must disabled one of the flippers in the pair to do a π flip, or we must op to do a 2π flip with both flippers running (thus both flippers flip by π). Figure 14 shows the non flipped beam polarization, the flipped beam polarization and the flipper efficiency, for a single flipper in the bootstrapped pair, thus for the total efficiency of one pair the results must be squared. The mean flipping efficiency of a single resonant flipper (non bootstrapped) was 96.6%. As a result the largest obtainable visibility using our two bootstrapped resonant coils is 87.1% (assuming a base visibility of 100%).

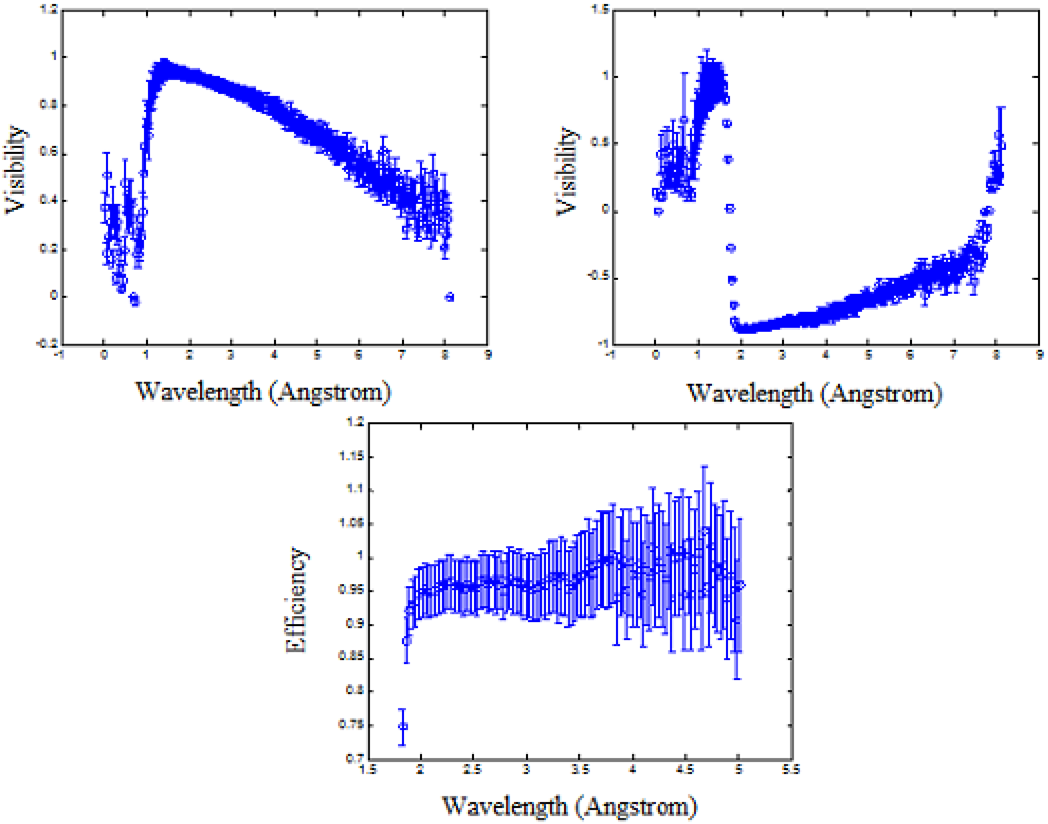

Figure 14. Graphs of the unflipped beam polarization (top left), flipped beam polarization (top right) and flipper efficiency (bottom).

3.3 High Field Radio Frequency Spin Flippers

Our novel flippers (Figure 15) were originally developed at TU Delft for spin echo techniques [36]. These flippers are capable of reaching higher fields and precession frequencies than conventional resonant flippers, due to the fact that they use magnetic poleshoes instead of an air core [10]. These poleshoes are made out of a high purity iron made by ARMCO. In addition these flippers are equipped with a gradient coil, which allows them to function as adiabatic flippers. When the gradient coil is disabled the flippers are basically just high field resonant flippers.

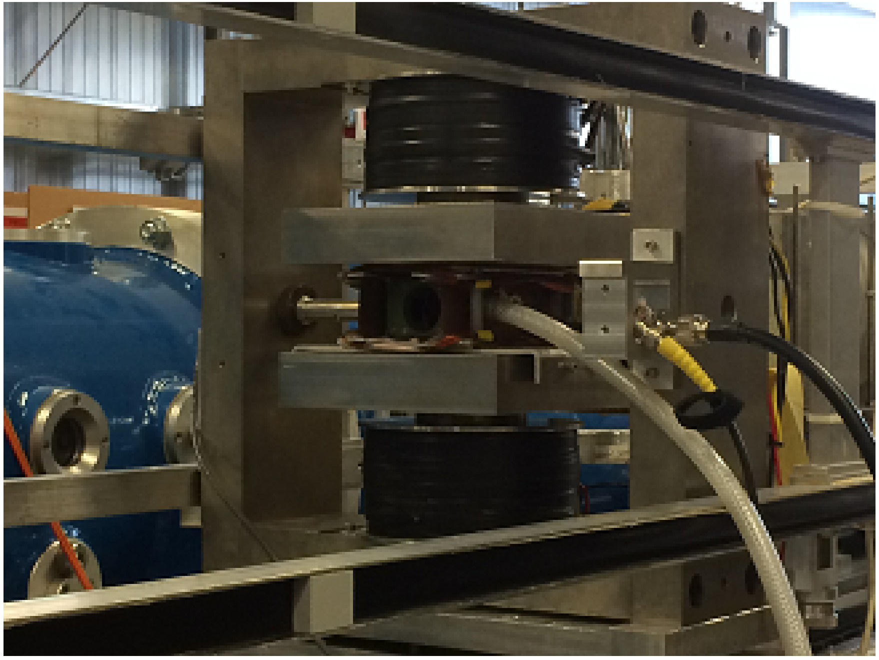

Figure 15. Picture of a high field radio frequency spin flipper at TU Delft.

Each flipper has one connection for compressed air to cool down the resonant coil and 5 electrical connections: one for the static field, another for the RF coil, one pickup coil to measure current in the RF coil, one for the gradient coil and the final one for a smaller coil which is wound around the magnetic yoke. This smaller coil is in place to compensate for the effects of hysteresis in the magnetic poleshoes. Furthermore these flippers are equipped with a Guass probe which is inserted between the two poleshoes. This Gauss probe is connected to a feedback loop which regulates the voltage across the static field coil, such that the field measured by the probe reaches a certain user defined setpoint.

When the gradient coils of these flippers are active and thus the flipper is operating as an adiabatic flipper, the resonant field amplitude can be set to a constant value, as was demonstrated in the theory section. In this case for a good π flip to occur the matching between the static field and the frequency of the RF field is not very sensitive (also demonstrated in the theory section) and one can trust that the actual static field is close enough to the user defined setpoint. However when this flipper is used as a resonant flipper the gradient field must be disabled and the RF field is modulated by a $1/t$ function like in the previous subsection, in addition the π flip is much more sensitive to the matching of the static field and the RF frequency, due to its long length (12cm) compared to our conventional resonant flippers. The feedback loop can no longer be trusted to set the correct field when the high field flippers are used as resonant flippers. This is because the Gauss probes are slightly displaced from the center of the flipper where the static field is slightly lower (Figure 16). Thus some manual adjustment on the side of the user is required to get a good π flip.

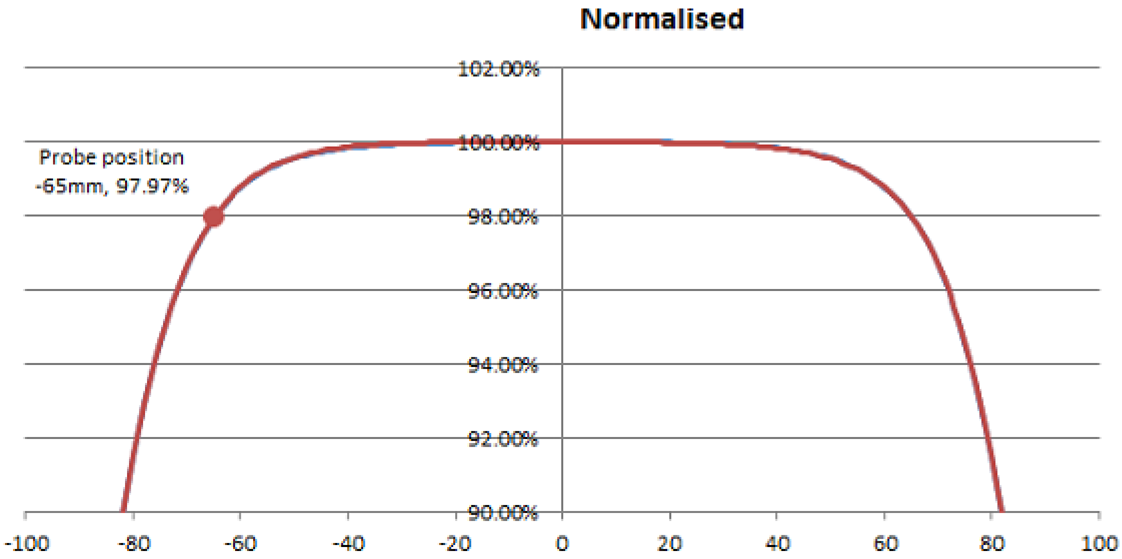

Figure 16. Normalized magnetic field strength as a function of distance (in mm) from the center of the flipper. The Gauss probe position is marked with a red dot.

The flip efficiency of our novel flippers during these experiments was 95%, however these flippers were not tuned as extensively as our resonant flippers due to time constraints. Keep in mind that due to the high field nature of our novel flippers they do not need to be bootstrapped, thus only two flippers are required for MIEZE, leading to a maximum polarization of 90%.

3.4 Detector Technology

Neutron detection plays a crucial role in a MIEZE instrument. In particular the time resolution of the detector is of critical importance when attempting to measure high frequency modulation. This time resolution is determined by two factors: the sampling frequency and the thickness of the detection interface. If neutrons are detected across the detector interface with equal frequency this time resolution is given by:

$$\Delta t = \frac{d}{v} \tag{124}$$

where d is the size of the interface and v the neutron velocity. Monte-Carlo simulations show that the time resolution is a bit higher due to the fact that neutrons are slightly more likely to be detected in the front of the detector than in the back of the detector. These simulations assume an exponential distribution type absorption pattern to calculate the expected visibility and Figure of Merit (FoM) [38] (see appendix and results).

$$FoM = P^2 I \tag{125}$$

Where P is the visibility and I the count rate. The calculations also take the focal shape (equation 93) into account, by averaging over it using an exponential probability distribution function. These simulations are conducted using C++, the results are saved to a binary file and imported into Matlab. Using Matlab the results can be analyzed and plotted into a graph.

Nonetheless measurement of high frequency MIEZE signals will require thin detectors. CASCADE is a detector which employs thin boron sheets and an ionization chamber. The boron sheets convert the neutrons into ionizing radiation, which is detected in the ionization chamber [37]. The fact that the boron sheets are so thin lends the detector a very high time resolution.

For the experiments shown in this report 1cm thick helium tubes were used (Figure 17). Using the neutron imaging setup at TU Delft the macroscopic absorption cross-section of the tubes was determined, this was critical for the Monte-Carlo simulations described above. We attempt to increase the time resolution of the tubes by placing 8mm cadmium strips in front of the detector. This reduces the effective thickness of the detector, thus increasing the time resolution.

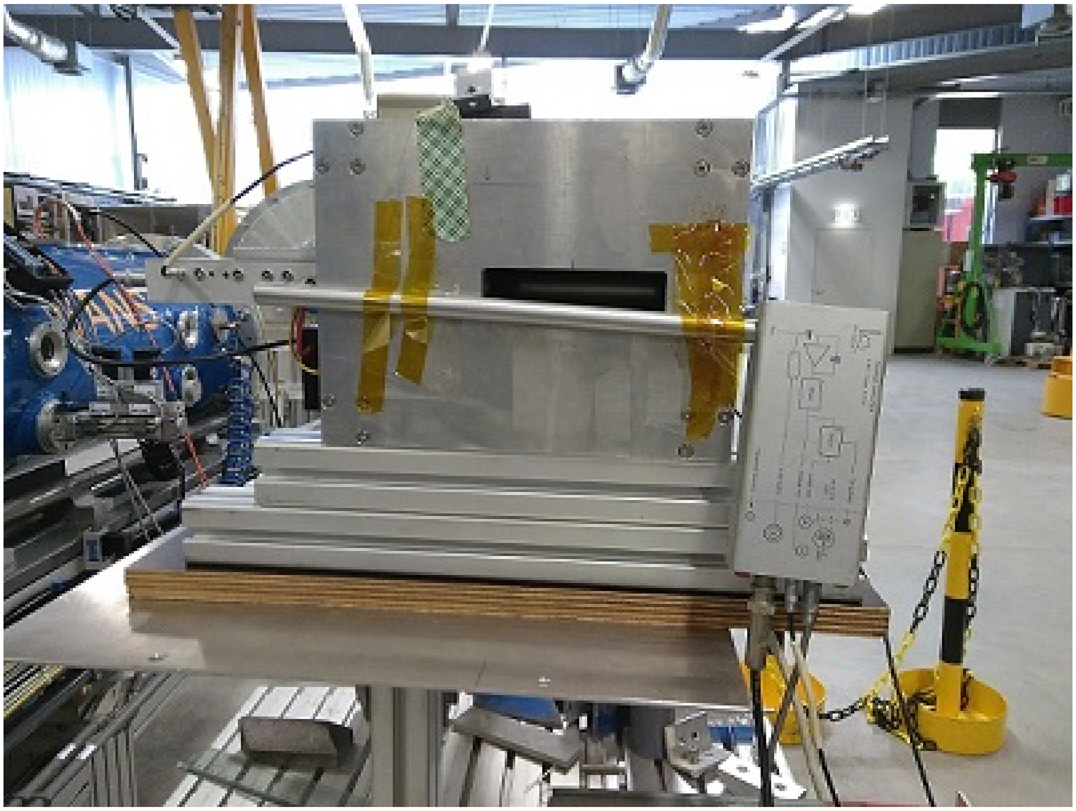

Figure 17. Picture of a 1cm helium tube taped to a beamstop.

Figure 18. Picture of the position sensitive detector consisting out of 16 helium tubes.

To measure the focal spot size (equation 93) a position sensitive detector is employed, which consists out of 16 1cm thick helium tubes placed behind each other on an incline (Figure 18). Due to the incline each tube "sees" a small part of the neutron beam at a different distance from the MIEZE instrument. We note that each tube produces a "neutron shadow" on the tubes behind it, thus reducing the effective diameter of said tubes. As a result the time resolution of these tubes is slightly higher than that of a single ^{3}He tube.

3.5 Conventional Setup

Our conventional setup (Figure 19) is a MIEZE instrument constructed using two bootstrapped resonant flippers, separated by a distance of $67cm$, inside of a zero field chamber. The zero field chamber prevents stray external fields from entering, which mitigates depolarization effects. $\frac{\pi}{2}$ rotators are placed at the entrance and exit of the zero field chamber. An adiabatic spin flipper, which functions as our beam flipper, is placed between the polarizer and the zero field chamber. The analyzer is placed closely after the last $\frac{\pi}{2}$ rotator. Finally the detector is placed $4.2m$ from the second resonant flipper. The goals of this setup are to measure the shape of the focal spot, demonstrate the out of focus time of flight MIEZE frequency shift, demonstrate the importance of the detectors thickness and to build a foundation which can be "compared" to our experimental setup.

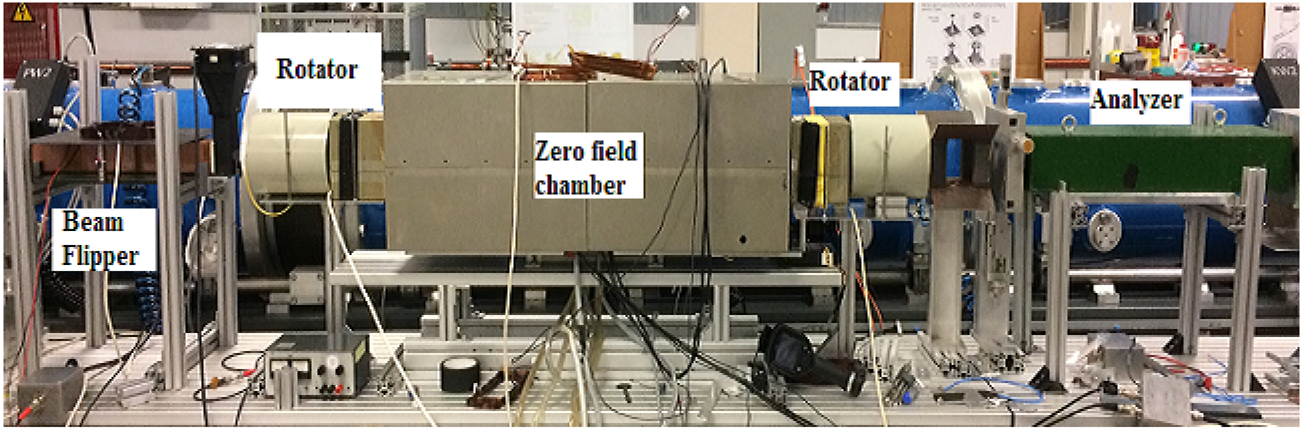

Figure 19. A picture of the entire setup: from left to right one can see the beam flipper, $\frac{\pi}{2}$ rotation element, the zero field chamber containing the two resonant flippers, another $\frac{\pi}{2}$ rotation element and finally the analyzer.

The highest well detectable MIEZE frequency of our setup should be around $100kHz$ (based on Monte Carlo simulations), therefore the difference between the two frequencies of the second and first flipper is set to $25kHz$ (recall that these are bootstrapped flippers). In this case the frequency of the first flipper must be set to $156.6kHz$ and the frequency of the second flipper to $181.6kHz$. This means that the static fields must be set to $5.4mT$ $(17.2A)$ and $6.2mT$ $(20A)$ respectively. Due to the high currents required to maintain these static fields both water and air cooling are used. The chopper is $9.3m$ from the detector and is set to spin at $25Hz$, which leads to an effective pulse frequency of $50Hz$. Furthermore the chopper disks are placed $0.4m$ apart to ensure a sufficiently high count rate. Two experiments are conducted using this configuration; the first utilizes the position sensitive detector to measure the focal spot and demonstrate the MIEZE frequency shift in time of flight. The second experiment utilizes a $10mm$ helium tube covered with an $8mm$ cadmium strip to test the thesis presented in section 3.4. A final experiment is conducted using a tube with an effective diameter of $8mm$. In addition the chopper disks are placed close together $(17cm)$ to increase wavelength resolution. The goal of this experiment is to maximize polarization. Table 1 shows all relevant instrument parameters.

	D	L	f_1	f_2	f_m	$\frac{\Delta\lambda}{\lambda}$	S	F
Experimental Parameters	$0.67m$	$4.2m$	$156.6kHz$	$181.6kHz$	$100kHz$	$1.8\% - 4.3\%$	$9.3m$	$50Hz$

Table 1. Table containing all instrument parameters. D denotes the flipper separation, L the distance between the last flipper and the detector, f_1 the RF frequency of the first flipper, f_2 the RF frequency of the second flipper, f_m the expected in focus MIEZE frequency, $\frac{\Delta\lambda}{\lambda}$ the wavelength resolution, S the distance between the source and the detector and F the pulse frequency.

3.6 Experimental Setup

The purpose of the experimental setup (Figure 20) is to demonstrate that our high field flippers are applicable to MIEZE and yield results which are similar to those of a conventional setup. In addition we wish to confirm the theory derived in section 2.6 for the MIEZE focusing condition when using a guide field. Furthermore this setup demonstrates the "MIEZE start up procedure" which will be required when doing MIEZE at Larmor with high modulation frequencies.
The setup consists of two high field flippers ($70cm$ separation) contained inside of a guide field. The guide field replaces the zero field chamber of a conventional setup by preventing depolarization of the beam due to stray fields. $\frac{\pi}{2}$ rotators are located at the edges of the guide field. An adiabatic flipper placed between the polarizer and the first rotator functions as a beam flipper. The analyzer is placed as close to the last rotator as possible. Finally the detector (a $1cm$ helium tube) is located roughly $4.2m$ from the last flipper. This distance is fine tuned by measuring the MIEZE frequency and using equation (93). The pulse frequency is once again set to $50Hz$ and the wavelength resolution is maximized by putting the chopper blades close together ($\frac{\Delta\lambda}{\lambda} = 1.8\%$). Feedback loops, with user defined set-points are used to control the field strength.

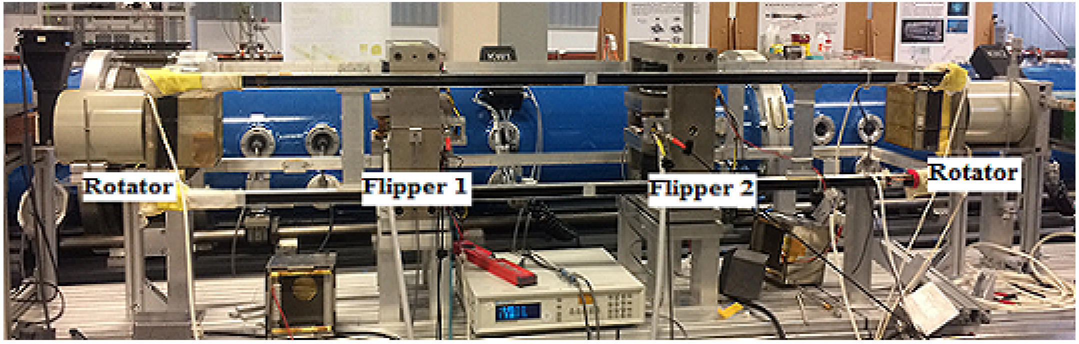

Figure 20. Picture of the experimental MIEZE setup. From left to right one can see the edge of the beam flipper, a $\frac{\pi}{2}$ rotator, the two flippers and the final rotator. In addition one can see the guide field coil placed around the flipper setup.

3.6.1 MIEZE Startup Procedure

Due to the small focal spot size at high modulation frequencies a procedure is required to ensure that the detector is placed exactly in focus. To achieve this we start at low frequencies and preferably in a situation where $D \approx G_1 + G_2$. However the latter becomes less critical as the modulation frequency increases. At low frequencies the focal spot is large according to equation (93) and using the frequency shift one can determine the exact location of the focal point. Once the detector has been placed in the exact focal point the frequency of each flipper can be doubled. If the condition $D = G_1 + G_2$ is met the focal point should not move. After doubling the flipper frequencies one checks the frequency shift again and moves the detector (if necessary) to the correct focus. Once this step is completed one can double the frequencies once more. One can repeat the previous steps until one reaches the desired modulation frequency. In the experiments shown here the modulation frequencies $20kHz$ $40kHz$ and $100kHz$ are chosen for demonstration purposes. The relevant instrument parameters are listed below in table 2.

	f_1	f_2	D	$\frac{\Delta\lambda}{\lambda}$	S	F	B_g	$G_1 + G_2$
$20kHz$	$61.49kHz$	$71.49kHz$	$0.70m$	1.8%	$9.3m$	$50Hz$	$0.6mT$	$1.0m$
$40kHz$	$122.98kHz$	$142.98kHz$	$0.70m$	1.8%	$9.3m$	$50Hz$	$0.6mT$	$1.0m$
$100kHz$	$307.45kHz$	$357.45kHz$	$0.70m$	1.8%	$9.3m$	$50Hz$	$0.6mT$	$1.0m$

Table 2. Table containing relevant experimental parameters for each modulation frequency. f_1 denotes the RF frequency of the first flipper, f_2 the frequency of the second flipper, D the distance between the two flippers, $\frac{\Delta\lambda}{\lambda}$ the wavelength resolution, S the distance between the source and the detector, F the pulse frequency, B_G the guide field strength and $G_1 + G_2$ the distance from the first rotator to the first flipper plus the distance from the second flipper to the second rotator.

3.7 Data Acquisition and Processing

The final steps towards generating useful results are data acquisition and processing. This subsection describes the steps taken to generate raw data and interpret said data in a meaningful way. The first part of this subsection is about the acquisition, while the last part is about data processing.

3.7.1 Acquisition

Data is acquired digitally using A/D converters and a LabView software interface. In addition this software gives control over a variety of experimental parameters such as the detector sampling frequency, total number of samples, chopper rotation speed, turning on and off the beam flipper and in the case of our experimental setup the static magnetic field strength of both flippers. The software will acquire time of flight data with the beam flipper off (e.g. I_+) for a user defined amount of time and then collect data with the beam flipper on (e.g. I_-) for a user defined amount of time. This data is written into a .jpl file. A custom Matlab script (see appendix) is utilized to import the .jpl data and start the first processing steps.

Due to hardware limitations the total number of samples may not exceed 4000, which means that it is not always possible to capture the entire $20ms$ pulse if the sampling frequency is very large. In addition due to said limitations it is not possible to do measurements of different parts of the pulse and stitch them together like a mosaic image. This is because the user defined delay is misinterpreted by the software under these conditions. As a result the user does not know at which point in the pulse the hardware starts and stops measuring. A possible remedy for this is to mark the signal at certain points, either by changing the MIEZE frequency for certain wavelengths or just turning off the flippers for a specific amount of time at specific wavelengths (thus encoding the wavelength in the "dead time").

3.7.2 Processing

As described above the raw data is imported into Matlab using a script. This script takes the I_+ and I_- data and calculates the statistical errors according to the well known formula

$$\sigma_I = \sqrt{I} \tag{126}$$

Using equation (122) the visibility is determined and the error is calculated by another well known formula in statistics.

$$\sigma_P = P\sqrt{\frac{1}{I_+} + \frac{1}{I_-}} \tag{127}$$

The data comes in simply numbered by bins. The script must convert the bin number to a time by multiplying it by the sampling time and adding any user defined delays. In addition this time is converted to a wavelength using equation (120). Finally the I_+ and I_- data are plotted against wavelength with errorbars in one graph and the Visibility is plotted against time with errors in another graph.

Upon completion of these initial processing steps we wish to determine the frequency and amplitude of our signals. Two custom Matlab scripts (see appendix) are at our disposal for this purpose. The first script performs a fast Fourier transform and plots the resulting spectral amplitude against frequency. The user can then determine the exact frequency of the signal and adjust the position of the detector if necessary according to equation (93). In addition the spectral amplitude at the MIEZE frequency should be equal to the contrast. These numbers can be used for example in the focal shape determination experiment. The second Matlab script is useful for calculating the intermediate scattering function of a sample. In addition to importing the data (both empty beam and sample in beam) and calculating errors it uses Matlabs curve fitting tool to fit sine waves to the signal. Each signal (empty beam and with sample) is cut up into a user defined amount of segments, the spin echo time is calculated for each segment and a sine wave is fit to each segment. The script then extracts the amplitude/visibility and the respective error from each fit. Finally the sample in beam amplitudes are divided by the empty beam amplitudes yielding the intermediate scattering function. The result is plotted with errors against the spin echo time.

The keen observer may have noticed that the conventional setup and the experimental setup do not use exactly the same detector. The conventional setup uses cadmium strips in front of the $1cm$ tube while the experimental setup does not. Using monte-carlo simulations a correction factor is derived and applied to the data to help better compare the two setups.

4 Results

Results from the various experiments are presented in this section. First the results from Monte-Carlo results are shown, followed by the various results from the conventional MIEZE experiment including the MIEZE signal seen by an $8mm$ helium tube, the cadmium covered $1cm$ tube and the position sensitive detector. The latter experiment also shows the focal spot size and frequency shifting. Next results from the experimental setup are shown including a comparison between the expected focal point position (equation 85) and the measured position. These experiments also demonstrate the MIEZE start up procedure. Following this the singals from the conventional setup are compared to the signals from the experimental setup, with and without the Monte Carlo based correction. Finally the results from an experiment demonstrating wavelength marking (discussed in section 3.7.1) are shown.

4.1 Monte Carlo Simulations

The Monte Carlo methods simulate the statistical absorption of neutrons, with a cosine like polarization, in helium 3 detectors of different sizes, assuming an exponential absorption probability distribution function. A random number, which indicates the position at which a neutron is absorbed, is "pulled" out of this exponential PDF. Using the neutron velocity a time of absorption is calculated. Finally the polarization of said neutron is put into the appropriate time bin. This process is repeated for one to ten million neutrons, to obtain a final figure for the polarization and figure of merit. Thus mathematically speaking the simulations average over a cosine using an exponential probability distribution function and calculate the absorption coefficient of various tubes. The simulations also take into account other factors which reduce visibility, such as focal shape and time averaging. Below the results from the Monte Carlo simulations are shown. Figures 21 22 and 23 are plots of the expected Figure of Merit and the visibility against the detector thickness. These simulations assume realistic settings comparable to the actual setups at TU Delft. Figure 24 shows the expected Figure of merit and visibility assuming similar conditions seen on the Larmor instrument at ISIS neutron source.

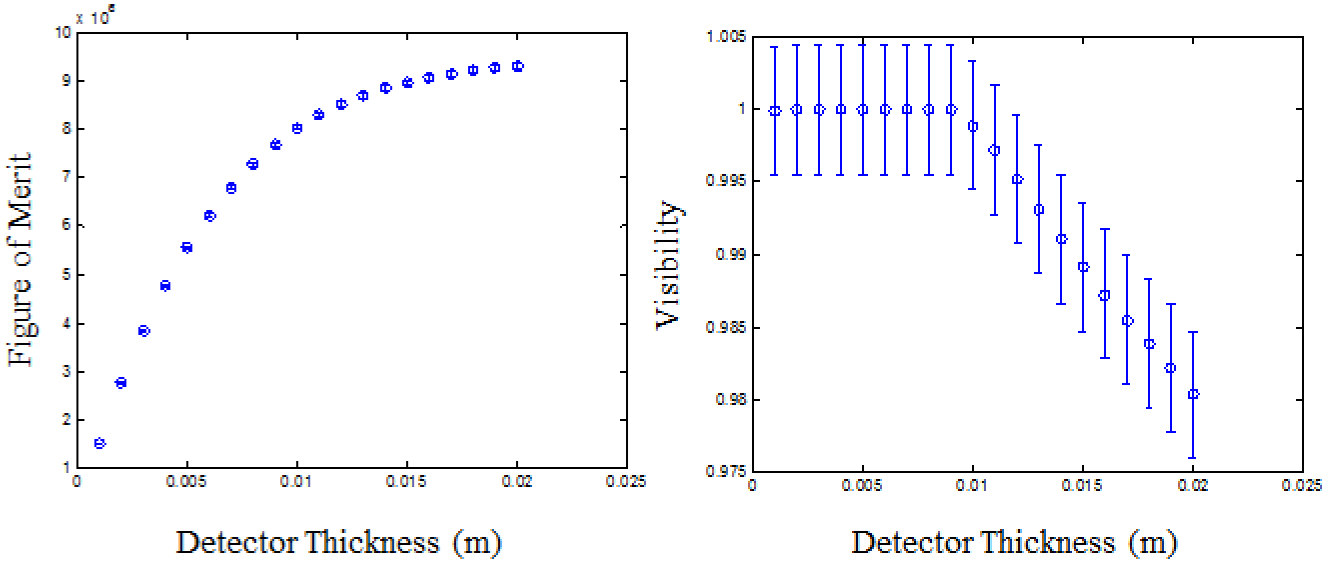

Figure 21. Results from the Monte Carlo simulations assuming a $20kHz$ MIEZE signal, a wavelength of 2.17Å, a wavelength resolution of 4.3% and a sampling time of $5\mu s$. The Figure of merit (left) and the visibility (right) are plotted against the detector thickness in meters with the respective statistical errors

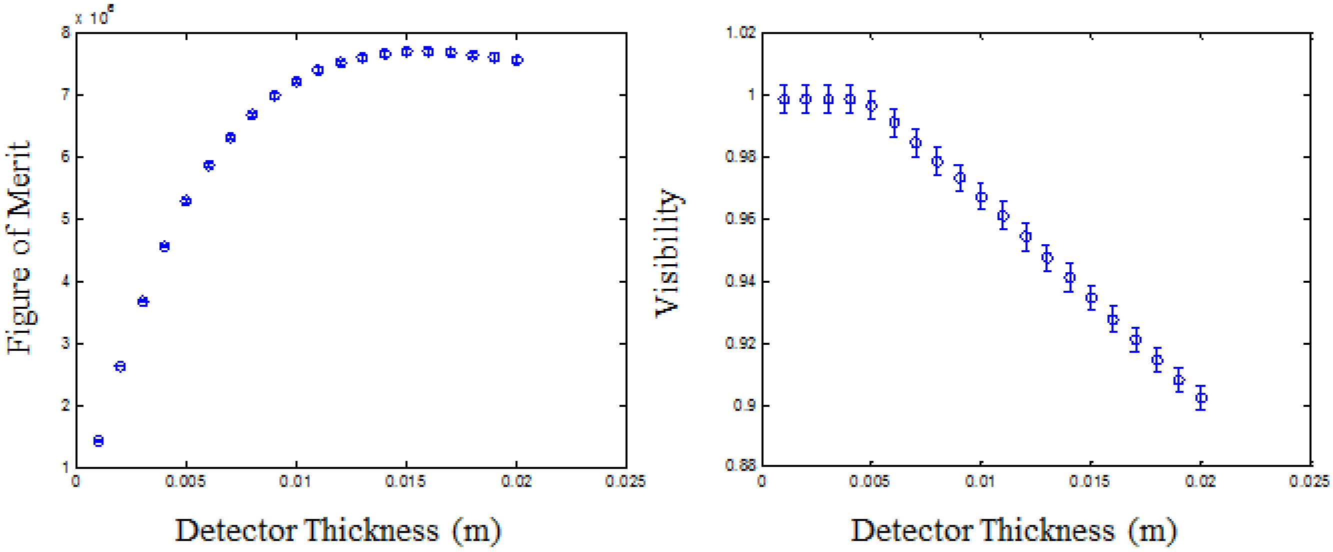

Figure 22. Results from the Monte Carlo simulations assuming a 40kHz MIEZE signal, a wavelength of 2.17Å, a wavelength resolution of 4.3% and a sampling time of 2.6μs. The Figure of merit (left) and the visibility (right) are plotted against the detector thickness in meters with the respective statistical errors

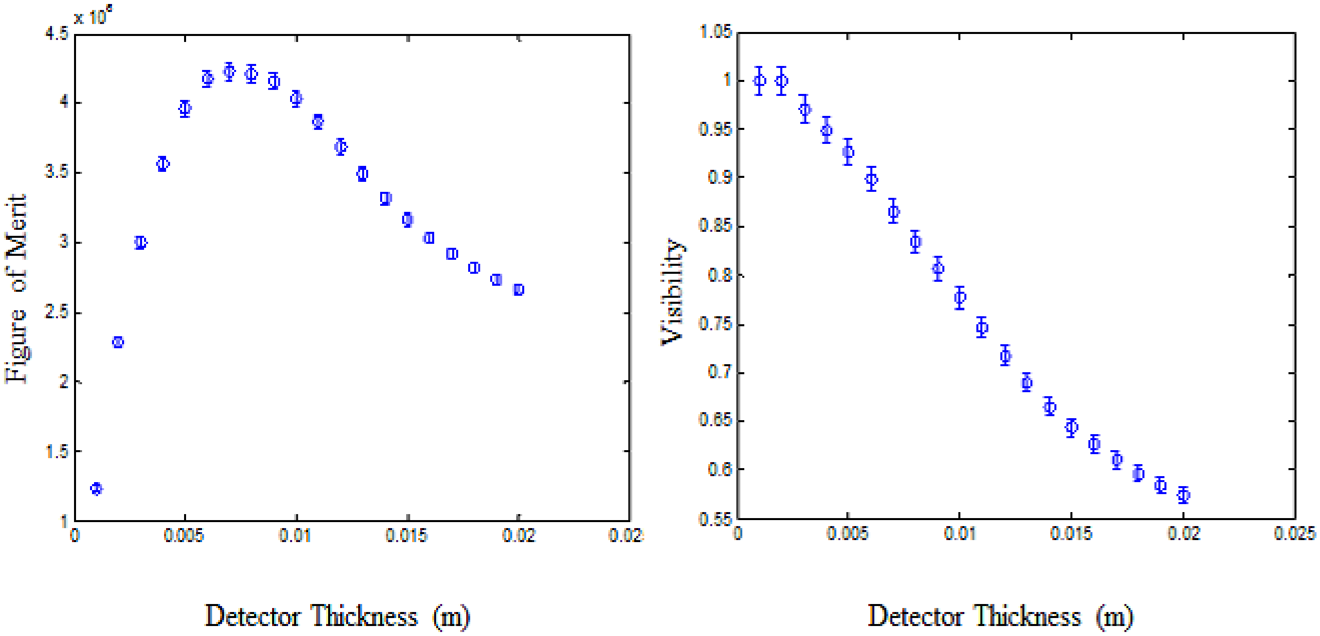

Figure 23. Results from the Monte Carlo simulations assuming a 100kHz MIEZE signal, a wavelength of 2.17Å, a wavelength resolution of 4.3% and a sampling time of 1.2μs. The Figure of merit (left) and the visibility (right) are plotted against the detector thickness in meters with the respective statistical errors.

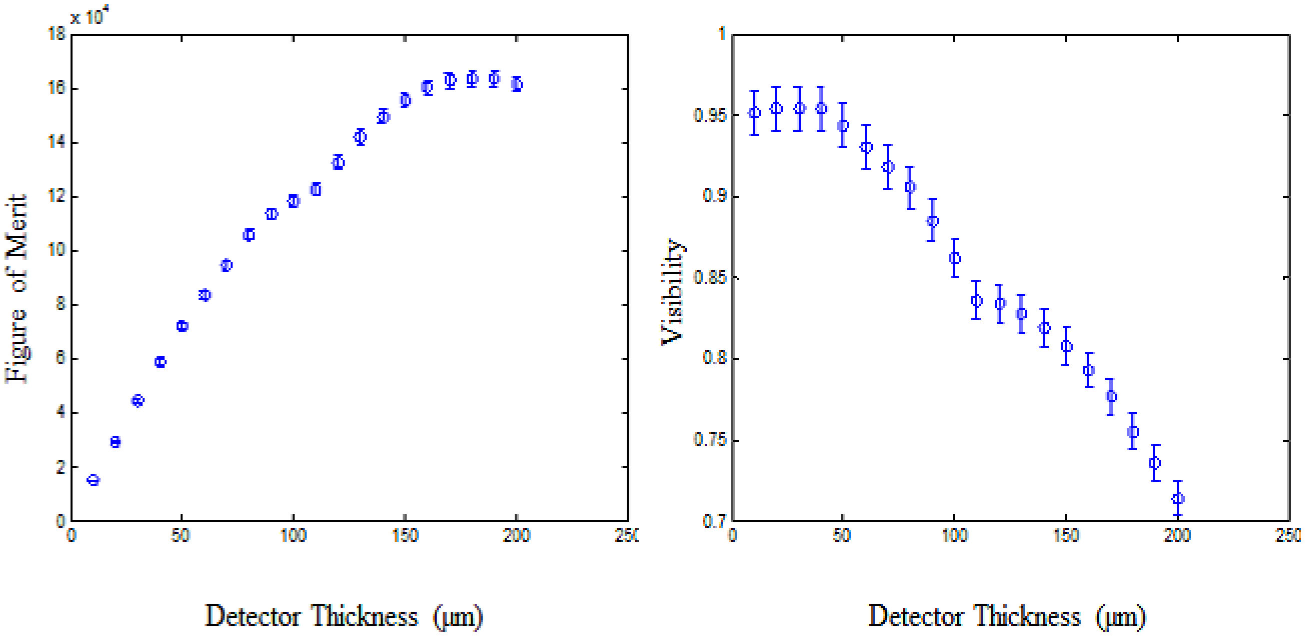

Figure 24. Results from the Monte Carlo Simulations assuming 1MHz MIEZE signal, a wavelength of 10Å, a wavelength resolution of 1% and a sampling of 10ns. The Figure of merit (left) and the visibility (right) are plotted against the detector thickness in micrometers with the respective statistical errors.

4.2 Conventional MIEZE Results

In this section MIEZE signals are shown that were generated using the conventional setup. In addition the focal shape and frequency shifting is shown. Figure 25 shows a $100kHz$ MIEZE signal as seen by the $8mm$ helium tube. Figure 26 shows the same signal as seen by a $10mm$ tube covered by an $8mm$ cadmium strip. Figure 27 and 26 show results using the position sensitive detector, the first one shows FFTs of the MIEZE signal detected by each tube and the latter shows the maximum visibility observed by each tube (the focal shape).

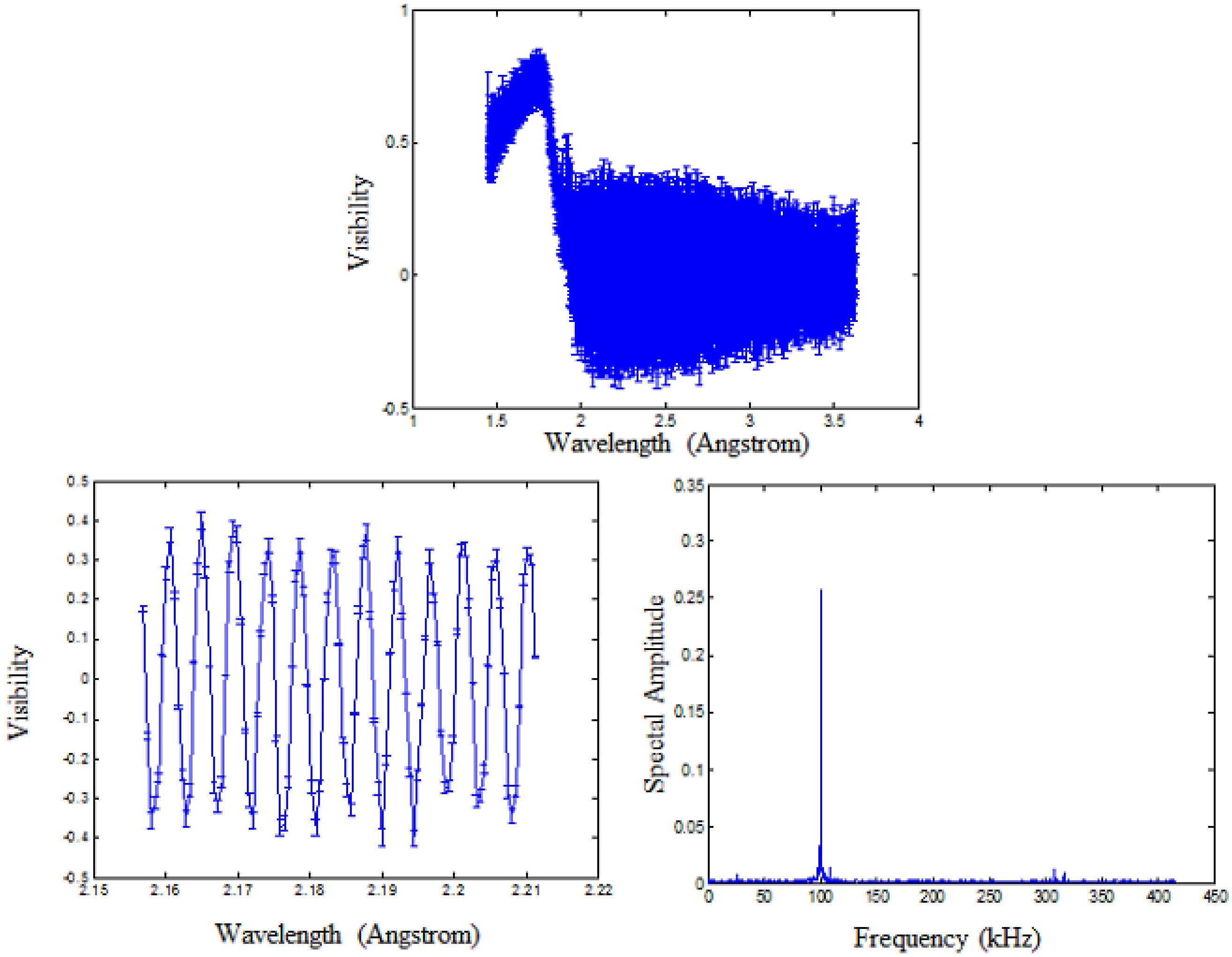

Figure 25. A $100kHz$ TOF MIEZE signal generated by the conventional setup as seen by an $8mm$ detector taking 1 sample every $1.2\mu s$. The top plot shows the full signal against the wavelength in Angstrom, the oscillations are not visible due to the high frequency compared to the pulse time. The lower left plot shows a small part of the MIEZE signal against wavelength and the lower right plot shows an FFT of the full MIEZE signal (top).

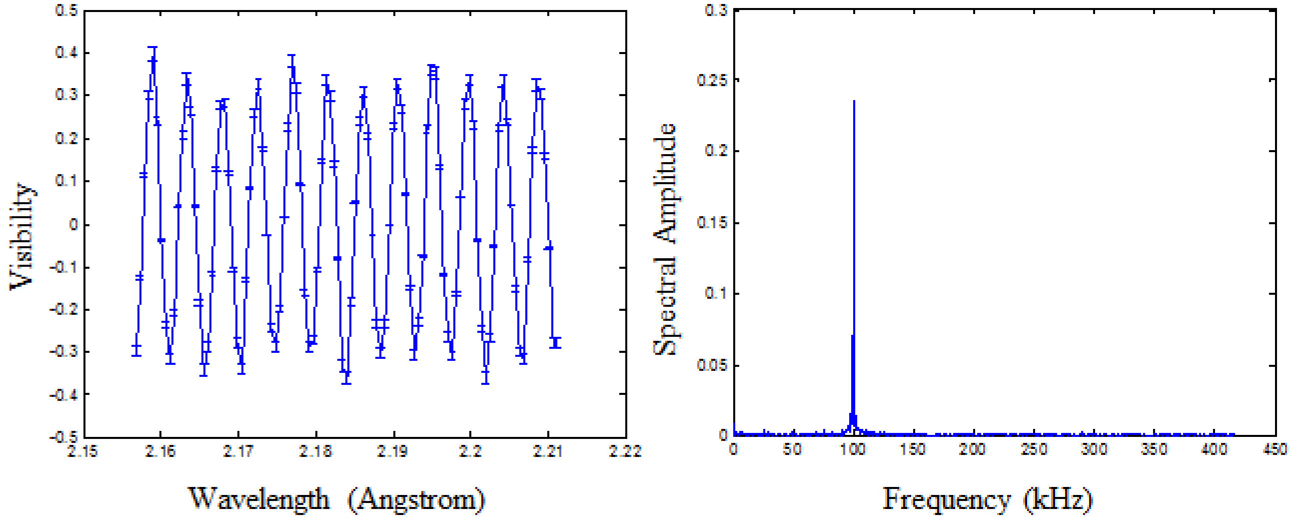

Figure 26. A 100kHz TOF MIEZE signal generated by the conventional setup as seen by a 1cm detector covered with an 8mm cadmium strip taking one sample every 1.2μs. The left plot shows a small part of the MIEZE signal against the wavelength in Angstrom. The right plot shows the FFT of the full MIEZE signal.

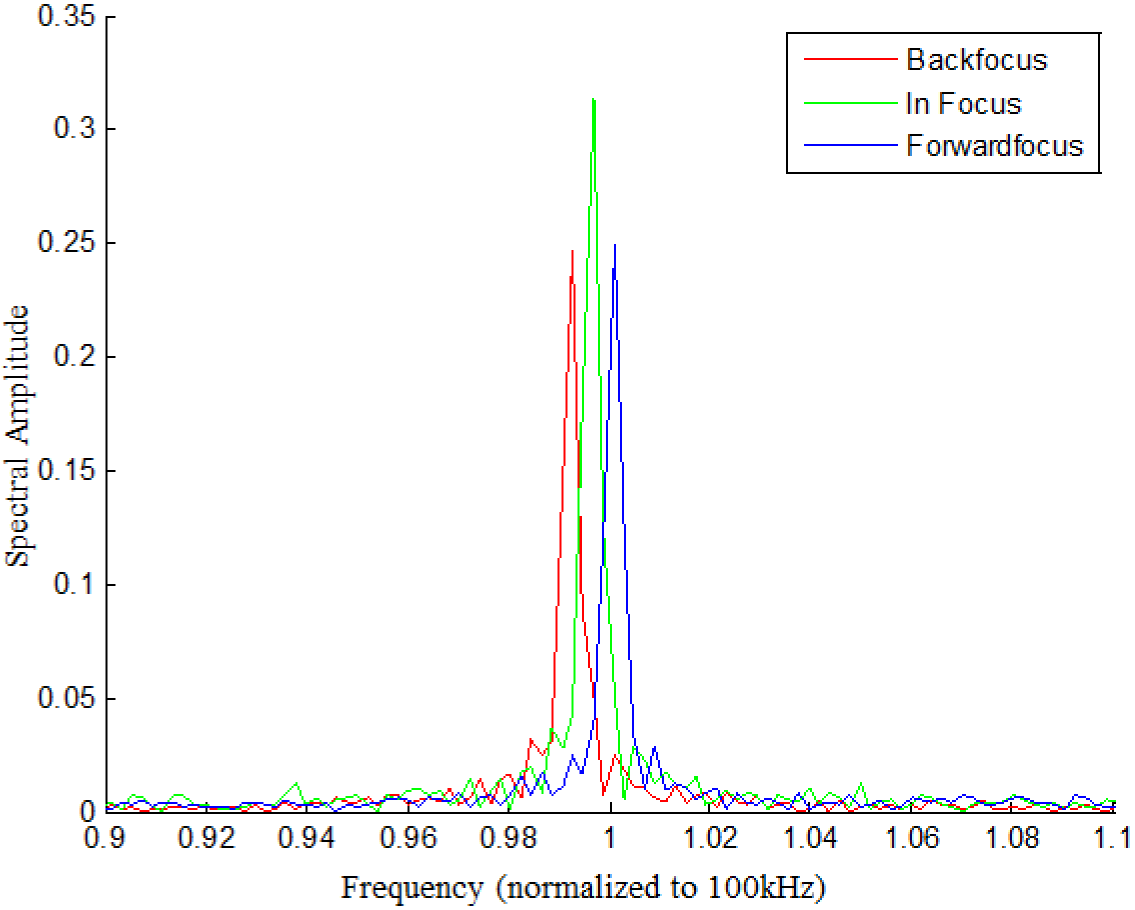

Figure 27. FFTs of MIEZE signals seen at different distances from the focal point. The signals were recorded using the position sensitive detector, which sampled once every $1.2\mu s$. The green curve is the in focus MIEZE signal, while the red curve is the MIEZE signal recorded $4cm$ further away from the second RF flipper and the blue curve is the MIEZE signal recorded $4cm$ closer to the second RF flipper.

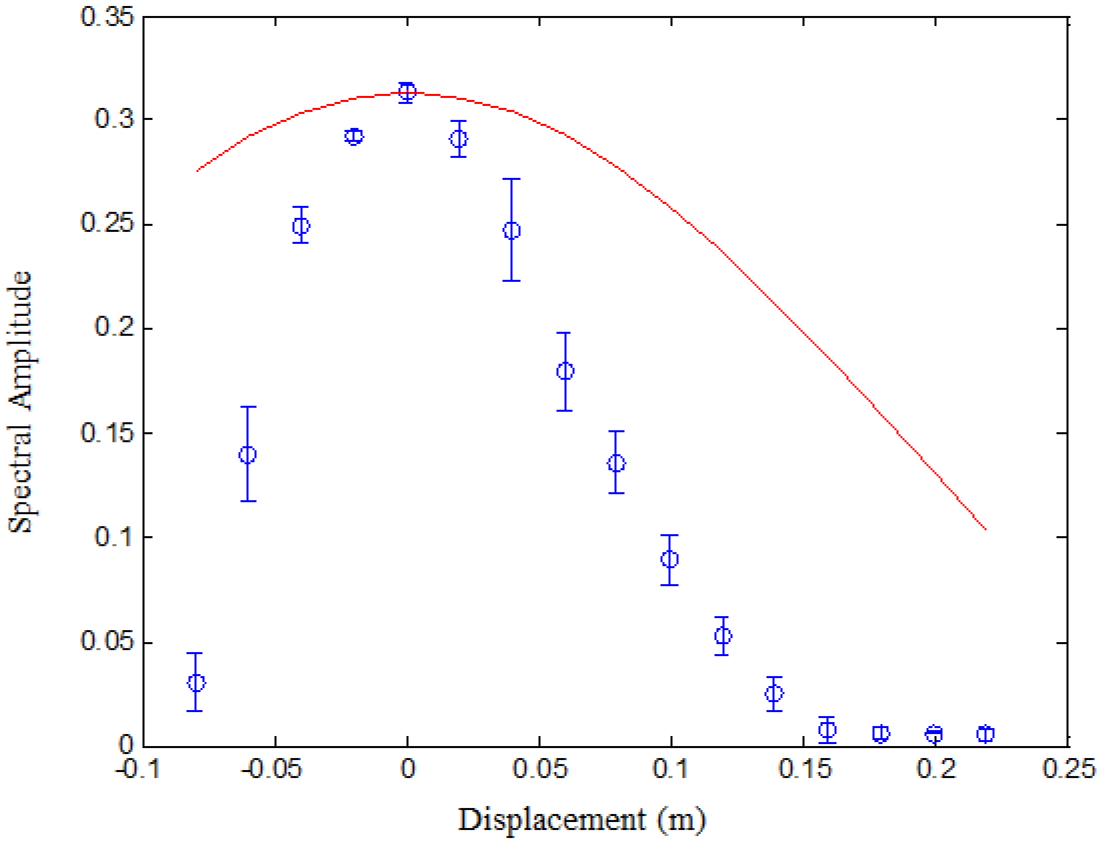

Figure 28. Spectral Amplitude as seen by each tube of the position sensitive detector, the x-axis denotes the helium tubes position with respect to the focus position. The red line represents the theoretical expectation (equation 93). The errorbars indicate two standard deviations.

4.3 Experimental MIEZE Results

In this subsection the results from the MIEZE startup procedure are shown in Figure 29. In addition in table 3 the real focal position is shown next to the expected focal position (equation 85).

Frequency	L_{theory}	L_{exp}	$\frac{\Delta L}{L_{theory}}$
$20kHz$	$4.62m$	$4.73m$	2.4%
$40kHz$	$4.49m$	$4.51m$	0.5%
$100kHz$	$4.39m$	$4.36m$	0.7%

Table 3. Expected distance from the last flipper to the focal point L_{theory}, experimentally determined distance from the last flipper to the focal point L_{exp} and the relative error for various MIEZE frequencies.

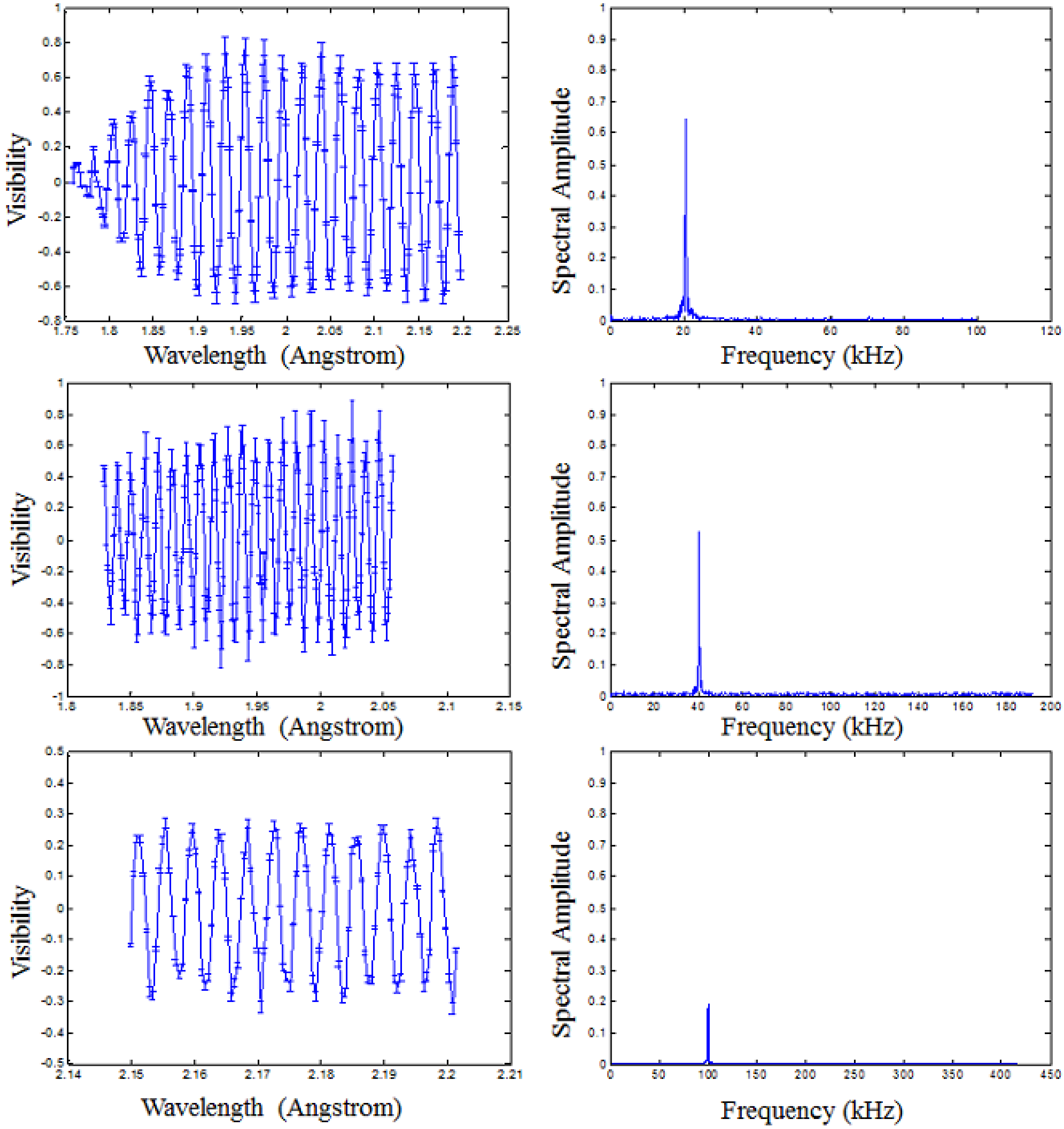

Figure 29. MIEZE start up procedure using the experimental MIEZE setup. The top graphs show a 20kHz signal (left) and its FFT (right), the middle ones show a 40kHz signal with the respective FFT and the bottom graphs show a 100kHz signal with the respective FFT.

4.4 Comparisons and Corrections

In this subsection the result from the experimental and conventional setups are put side by side (Figure 30). In addition the corrections found using Monte-Carlo simulations are applied (Figure 31).

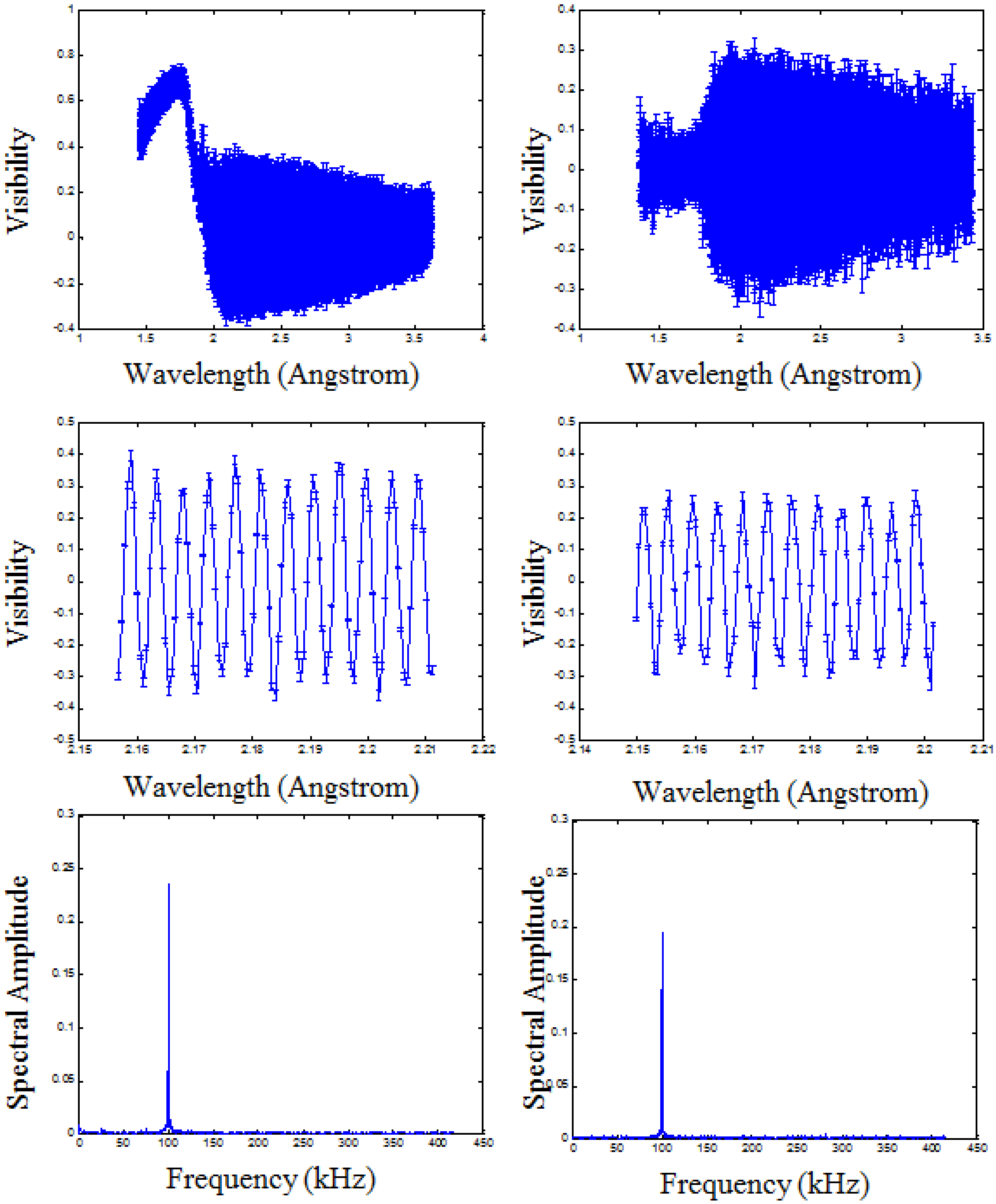

Figure 30. Side by side view of the results from the conventional (left) and the experimental setup (right). The full time of flight signal is shown at the top, while a small snapshot of the MIEZE signal is shown in the middle and finally at the bottom the FFT of each signal is shown.

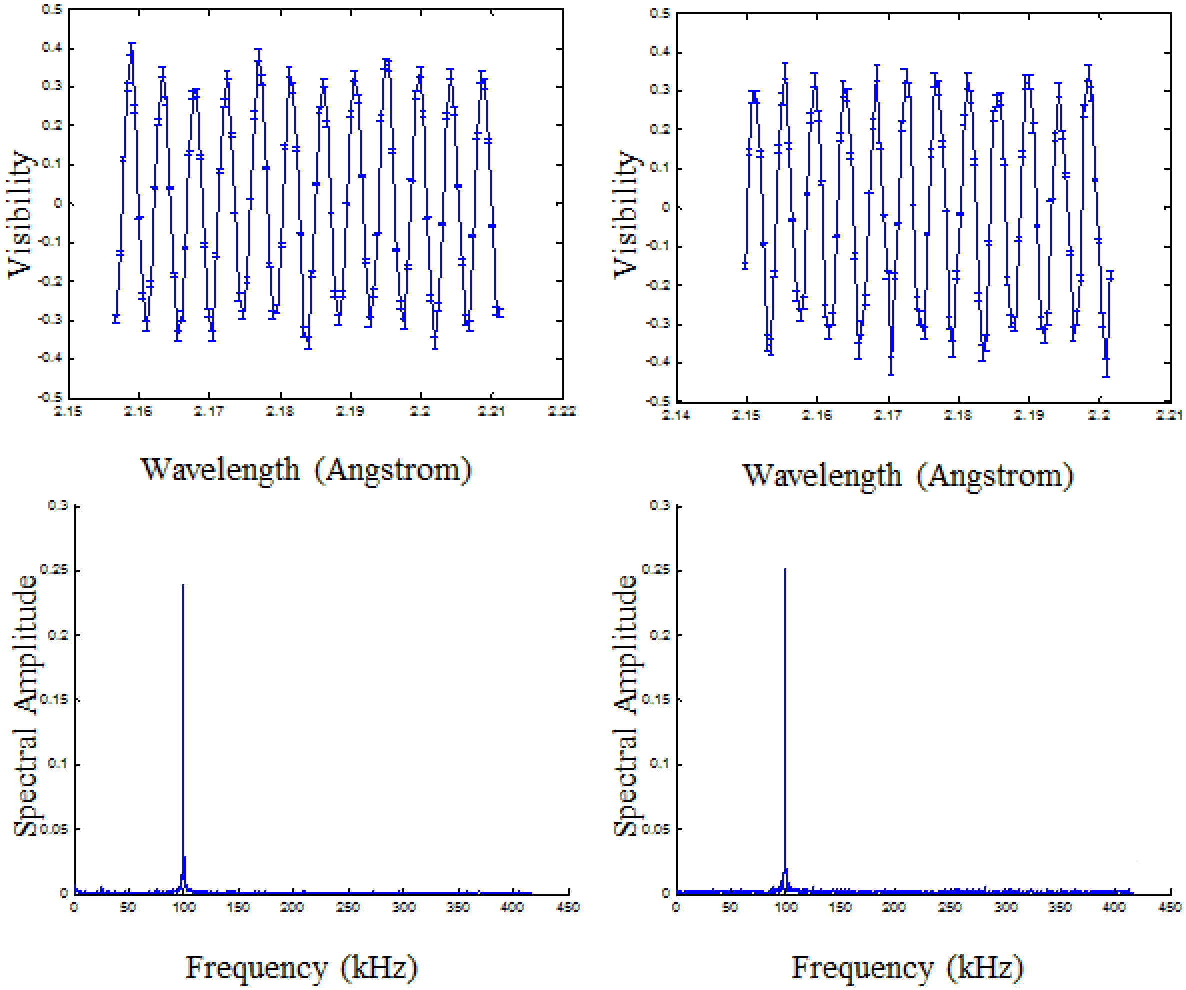

Figure 31. Side by side view of the results from the conventional (left) and experimental (right) setup. The results have been corrected using the Monte-Carlo simulations. The top signals are small snapshots of the MIEZE signals. The bottom graphs show the respective FFTs.

4.5 Wavelength Marking

In this last subsection the wavelength marking method is shown. Figure 32 shows the marked MIEZE signal as a function of time, while Figure 33 shows the same signal as a function of wavelength.

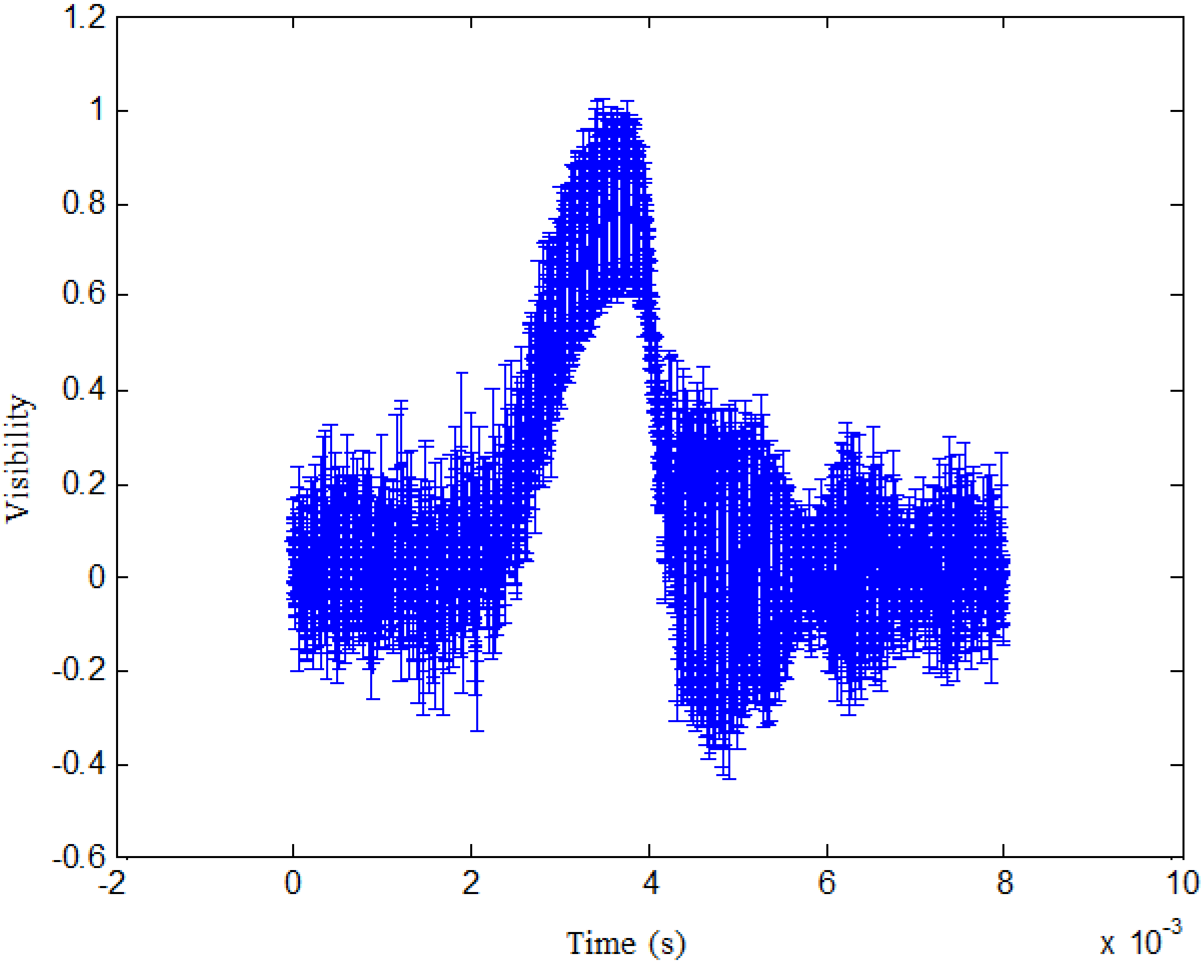

Figure 32. A 100kHz MIEZE signal generated with the conventional setup. The flippers are turned off and on again as to mark certain wavelengths. The y-axis denotes the visibility, while the x-axis denotes the time in seconds.

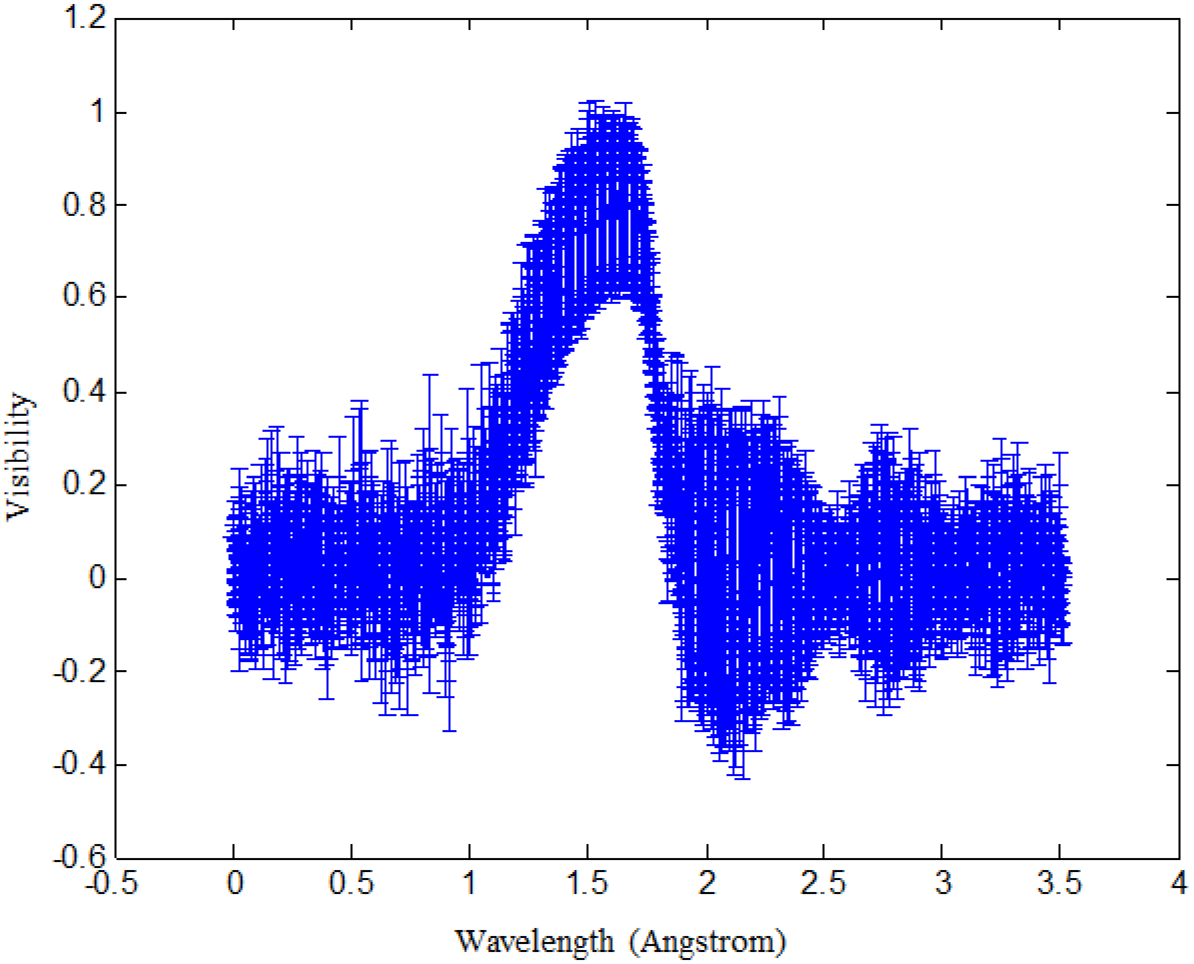

Figure 33. A 100kHz MIEZE signal generated with the conventional setup. The flippers are turned off and on again as to mark certain wavelengths. The y-axis denotes the visibility, while the x-axis denotes the wavelength in Angstroms.

5 Discussion

We attempt to interpret the results shown in the previous section and explain discrepancies between theoretical prediction and experimental reality. In addition some of the results have lead to the development of new methods, which are also explained in this section. However first of all we will note the most important results which concern the main goal of this thesis. It has been demonstrated that the new high field flippers, which are also used by the Larmor instrument are capable of producing a MIEZE signal with a frequency of up to $100kHz$ (i.e. Figure 29). In fact the MIEZE signal produced by these flippers seems to be competitive with conventional resonant flippers at $100kHz$ modulation frequency after corrections for detector thickness are applied (i.e. Figure 31). When these corrections are not applied the conventional flippers outperform our high field flippers (as expected), though the total visibility is still similar (i.e. Figure 30). Furthermore table 3 shows that our theoretical predictions of the location of the focus agrees quite well with the experimental results, especially for higher MIEZE frequencies.

In the next subsection we take a closer look at the Monte Carlo simulations and the effects of detector thickness on the MIEZE signal. Followed by this, in the second subsection, the frequency shift of a defocused MIEZE signal in time of flight is discussed. The third subsection further discusses the comparison of the two MIEZE signals and the validity of the applied corrections. The fifth subsection evaluates the wavelength marking method. In the fifth subsection we will take a second look at the MIEZE focal shape. Finally in the last subsection we attempt to explain why the visibility of our MIEZE signals is lower than expected.

5.1 Monte Carlo Simulations and the Effects of Detector Thickness

Monte Carlo simulations (Figures 21-24) clearly demonstrate that the detector thickness makes the time resolution of said detector worse, however it appears that the time resolution remains much better than the simple prediction made in the method section (equation 124). The actual measured visibility (i.e. Figure 30 and 31) does differ from the predicted visibility (Figure 23), which implies that other factors are at play which result in a lowered total visibility. When we calculate the ratio between the visibilities at two different MIEZE frequencies (Figure 29) and compare this to the expected ratio using Monte Carlo, we find a discrepancy, which implies that there are other factors which are reducing the visibility. These other factors are probably dependent on the MIEZE frequency. These ratios have been calculated explicitly below in table 4.

Ratio	Monte Carlo	Experiment
$\frac{P_{100}}{P_{40}}$	0.80	0.37
$\frac{P_{100}}{P_{20}}$	0.78	0.30
$\frac{P_{40}}{P_{20}}$	0.97	0.82

Table 4. Ratio of visibilities, P, at various MIEZE frequencies of $100kHz$ $40kHz$ and $20kHz$. The ratio is calculated using the results from the Monte Carlo Simulations (left) and the results from the experimental MIEZE setup (right).

One can also see that the visibility as seen by the $8mm$ tube (Figure 25) is higher than the visibility as seen by the $1cm$ tube covered by an $8mm$ cadmium strip (Figure 26), which goes against expectations. However one cannot simply compare the two because the filling pressure and therefore the macroscopic capture cross section of the $8mm$ tube is unknown. The tubes used in the position sensitive detector are the same tubes as in the cadmium experiment. However in the position sensitive detector each tube creates a shadow across the tubes behind it. As a result the effective diameter of each tube in the detector is reduced. The positive effect this has on the visibility can be seen in Figure 27.

The Monte Carlo simulations do show a possible explanation for the discrepancy between the visibility as seen by the cadmium covered helium tube (conventional setup) and the amplitude seen by the uncovered tube (experimental setup).

5.2 Time of Flight MIEZE Frequency Shift

In section 2.6 a shift of the MIEZE frequency was predicted due to defocusing. Figure 27 appears to confirm this frequency shift qualitatively, however in this subsection we wish to confirm the quantitative reliability of our prediction. The frequency uncertainty is roughly $200Hz$ and is equal to the reciprocal of the signal length. The in focus MIEZE signal has a frequency of $99.7 \pm 0.2kHz$, the forward focus signal has a frequency of $100.1 \pm 0.2kHz$ and the backfocus signal has a frequency of $99.3 \pm 0.2kHz$. The predicted frequencies (using equation 93) are $100.0kHz \pm 0.4kHz$, $100.9kHz \pm 0.4kHz$ and $99.0kHz \pm 0.4kHz$ respectively. The uncertainties are based on the fact that the RF waveforms (two in total) which determine the MIEZE frequency each have a finite length. Thus the in focus and back focus frequency shifts are explained quite well by our model, while the forward focus deviates slightly from the theoretical prediction. This difference may be explained by the fact that the "neutron shadow" seen by one of the tubes close to the front of the position sensitive detector is different from the shadow seen by a tube closer to the back of the position sensitive detector. As a result the location within a tube where most neutrons are absorbed is different in a posterior tube compared to an anterior tube. Thus the actual measurement points may be further apart or closer together than $4cm$. Hence it is sensible to add an uncertainty to our positions of $1cm$, which results in an additional frequency uncertainty of $240Hz$. This added uncertainty would explain the discrepancy between our model and the experiment.

From a methodology standpoint the frequency shift due to defocusing was a helpful tool in determining where to put the detector in the MIEZE startup procedure demonstration experiment. If the detector is placed on top of a translation stage the focusing procedure could be completely automatized, using this method. In addition this method only requires a single measurement of the MIEZE signal to determine the location of the real focus, where as an amplitude based approach, which simply looks for the location where the amplitude of the MIEZE signal is maximal, would require a large number of measurements.

5.3 Comparison of the Conventional and Experimental Setups

In this subsection we attempt to compare the conventional MIEZE setup to our novel setup, which utilizes high field flippers. First we note that the neutron windows on the conventional flippers are larger than on the novel flippers, which allows the to work at greater intensities (given a large detector). However practical MIEZE setups are likely to be limited to smaller beam sizes, due to limitations on sample geometry, which become increasingly crucial for large angle scattering [39]. In addition the conventional coils require high currents and water cooling to run properly, while the high field coils function at currents an order of magnitude lower and only require air cooling. On the other hand the conventional coils are much shorter, as a result the RF field has a higher amplitude, which makes the flip less sensitive to mismatching between the static field and the RF frequency. However the high field flippers can be used as adiabatic flippers (still to be tested for MIEZE), which produce an even more stable flip.

Visibility wise the conventional setup outperforms the experimental setup, at a modulation frequency of $100kHz$ by roughly 20%, when we do not correct for detector differences. Yet once the correction has been performed the experimental setup produces the same visibility as the conventional setup. However the validity of the Monte-Carlo based corrections should be confirmed experimentally. In addition detector tilt relative to the incident beam should be taken into account in these corrections, as this tilt changes the effective detector thickness. Though this effective thickness scales with the cosine, thus in first order detector tilt is irrelevant.

The theoretical predictions of the location of the focus were spot on for the conventional setup, while the predictions for the experimental setup, which used a guide field, varied slightly from the measured focus point. This can be attributed to the fact that the utilized guide field did not produce is totally homogeneous field. Note that the accuracy of the predictions increases as the modulation frequency is increased, because the term $\frac{\omega_g}{2\Delta\omega}$, in equation (86), goes to zero.

5.4 Wavelength Marking

Recall that due to hardware and software limitations it is not possible to look at high frequency MIEZE signals at longer wavelengths, because the software does not attribute the correct "time-stamp" to each bin. To remedy this we mark certain wavelengths by turning off the flipper for a defined amount of time at the selected wavelengths. The "off time" thus encodes the wavelength. Figures 32 and 33 clearly demonstrate that the MIEZE signal can be disabled for short amounts of time and therefore that wavelengths can be marked. Though more processing tools are required to automatically recognize the wavelength based on MIEZE "deadtime". This problem is specific to the setup in Delft, therefore further development of this method is not required.

5.5 Focal Shape and Determining the Momentum Distribution of a Sample

The focal shape was derived theoretically to be a sinc function in section 2.6. Figure 28 shows slight agreement between the theory and the experiment for very small displacements, however for larger displacements the experimental results strongly diverge from the predictions. This is probably due to the fact that we assumed a zeroth order wavelength spread in section 2.6. In general the integral in equation (91), must be rewritten as:

$$< \sigma_x >= \int_{-\infty}^{\infty} R(\lambda, \lambda_0, \Delta\lambda) \cos\left(2\Delta\omega[t - \frac{m\lambda\Delta L}{h}]\right) d\lambda \tag{128}$$

Where $R(\lambda, \lambda_0, \Delta\lambda)$ is the distribution function, which has the property $\int R(\lambda, \lambda_0, \Delta\lambda) d\lambda = 1$. In literature often times a first order wavelength distribution function is used [31]. However for simplicity we will assume a Gaussian wave packet such that

$$R(\lambda, \lambda_0, \Delta\lambda) = \frac{1}{\sqrt{2\pi(\Delta\lambda)^2}} e^{-\frac{1}{2}[\frac{\lambda-\lambda_0}{\Delta\lambda}]^2} \tag{129}$$

We now fill this expression into equation (128) and use that the cosine transform is equal to the real part of the Fourier Transform

$$< \sigma_x >= Re[\int_{-\infty}^{\infty} \frac{1}{\sqrt{2\pi(\Delta\lambda)^2}} e^{-\frac{1}{2}[\frac{\lambda-\lambda_0}{\Delta\lambda}]^2} e^{-i(2\Delta\omega[t-\frac{m\lambda\Delta L}{h}])} d\lambda] \tag{130}$$

Next we use a substitution such that $\lambda' = \lambda - \lambda_0$, which simplifies the above equation to

$$< \sigma_x >= Re[e^{-i2\Delta\omega[t-\frac{m\lambda_0\Delta L}{h}]} \int_{-\infty}^{\infty} \frac{1}{\sqrt{2\pi(\Delta\lambda)^2}} e^{-\frac{1}{2}[\frac{\lambda'}{\Delta\lambda}]^2} e^{i2\pi\frac{2\Delta\omega m\lambda'\Delta L}{2\pi h}} d\lambda'] \tag{131}$$

The integral is a simple Fourier transform of a Gaussian which is given by [40][41].

$$< \sigma_x >= e^{-2(\frac{\Delta\omega m\Delta L\Delta\lambda}{h})^2} \cos\left(2\Delta\omega[t - \frac{m\lambda_0\Delta L}{h}]\right) \tag{132}$$

Figure 34 shows a fit of this Gaussian on top of our experimental data. The left most point was collected with the frontal tube, which sees a drastically different "neutron shadow" than the other tubes, therefore it has a different effective thickness and it does not line up with the fit nicely. By slightly adjusting the standard deviation of the Gaussian the fit can be improved, however this cannot be justified theoretically. It is more likely that the discrepancies are due to uncertainty in the helium tube location (as described in section 5.2).

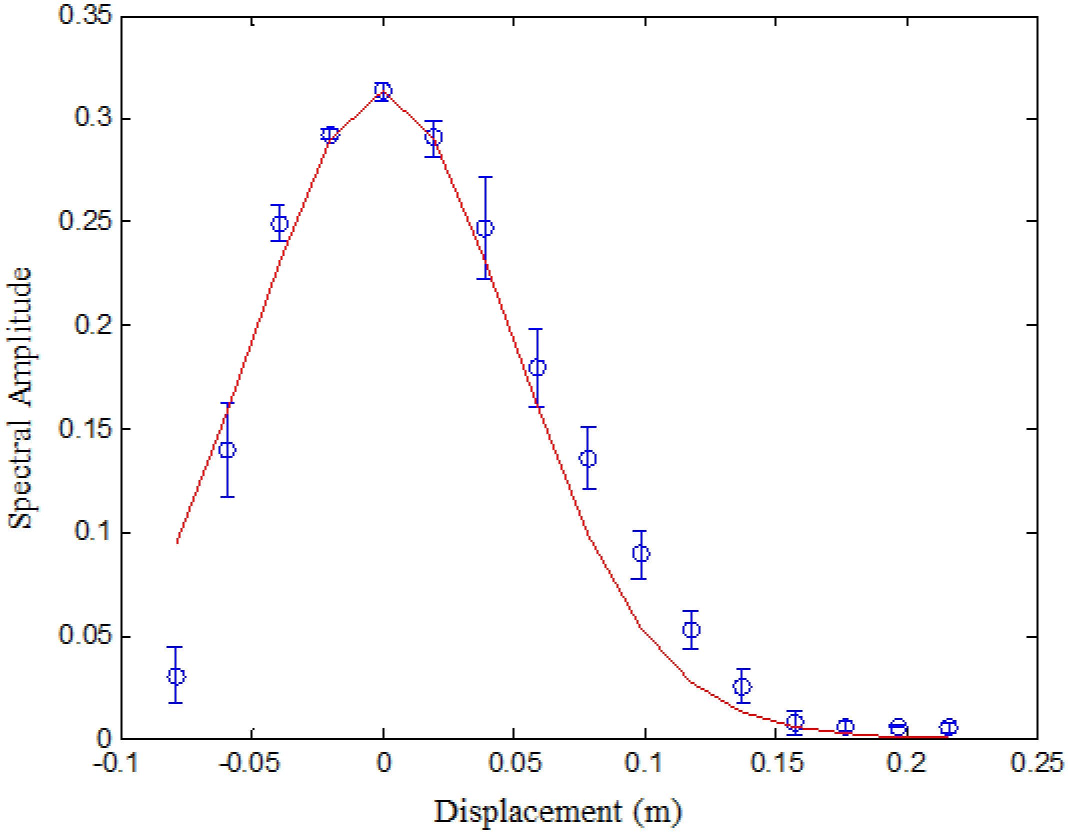

Figure 34. Fit of a Gaussian (red) described by equation (132) to experimental data (blue). The blue points denote the max. amplitude measured by a helium tube at a given distance from the MIEZE focus.

From equation (128) one can deduce that it is possible to measure the momentum distribution of nuclei in a sample, using a MIEZE sample, a highly monochromatic beam and by positioning the sample before the MIEZE instrument. The highly monochromatic beam scatters on the sample and enters the MIEZE instrument. Then using a position sensitive detector the MIEZE focal shape is measured. This focal shape should be equal to the real part of the Fourier transform of the momentum distribution of the sample as per equation (128). However the usefulness of this method is questionable, as it would require a very large position sensitive detector to measure a tight momentum distribution.

5.6 Other Causes for Reduced Visibility

One has likely noticed that the maximum visibility of roughly 35% (Figure 30 Experimental setup absolute maximum) cannot be solely explained by our Monte-Carlo simulations which take into account time averaging due to sampling, detector thickness and averaging over the focal spot. Thus there are other factors at play which affect the visibility in a negative way. There are a set of visibility reducing factors which are frequency independent which will be discussed in the first subsection and a set of frequency dependent factors which are discussed in the second subsection. Most of these factors only contribute a small amount to the total loss, therefore it is believed that the low visibility is due to cumulative effects.

5.6.1 Frequency Independent Factors

In this subsection frequency independent contributors to the loss of visibility are explored. Figure 14 demonstrates a base polarization of 96.5% at a wavelength of 2.1Å, in addition it was found that the flipper efficiency (non bootstrapped), was 96.6%. Thus for four flippers in the case of the conventional setup the total polarization would be reduced to $0.965 * 0.966^4 = 84\%$. In addition to imperfect flippers we also have losses due to the $\frac{\pi}{2}$ rotators. If these rotators do not rotate the spin perfectly by $\frac{\pi}{2}$, but by some angle $\frac{\pi}{2} + \delta\theta$, the visibility of the MIEZE signal will be reduced. This loss can be quantified using equation (82) and (83). We note that if our rotators do not rotate by $\frac{\pi}{2}$ we are no longer measuring the expectation value of the spin in the x-basis, but along some tilted basis $\hat{n} = [\cos(\delta\theta), 0, \sin(\delta\theta)]^T$, whose Pauli matrix is given by $\hat{n} \cdot \vec{\sigma}$. In addition $\vec{\psi}$ will no longer be in an equal superposition between up and down state, but will be given by: $\vec{\psi} = e^{i\sigma_z arg}[\cos\left(\frac{\pi}{4} + \frac{\delta\phi}{2}\right), \sin\left(\frac{\pi}{4} + \frac{\delta\phi}{2}\right)]^T$. Where arg is simply the argument of the e-function. Thus the expectation value would be given by

$$\left\langle \vec{\psi} \middle| \vec{\sigma} \cdot \hat{n} \middle| \vec{\psi} \right\rangle = \cos(\delta\theta)\cos(\delta\phi)\cos(2arg) - \sin(\delta\phi)\sin(\delta\theta) \tag{133}$$

Note that the right term $|\sin(\delta\phi)\sin(\delta\theta)|$ can be determined by measuring the mean value of our MIEZE signal. If in addition to that we assume that $\delta\phi$ and $\delta\theta$ are equal in magnitude, which is a reasonable assumption, since both $\frac{\pi}{2}$ rotators are identical, we can determine the amplitude reduction. By looking at our data it was determined that $\delta\phi = \delta\theta = 0.070 - 0.122Rad$. In the worst case scenario this gives an additional amplitude reduction of $\cos(0.122)^2 = 0.98\%$
Another factor which can lower the MIEZE amplitude is background. This can be demonstrated using equation (122) and by adding a constant relative background B to I_+ and I_-. Then we find

$$P = \frac{1 + \cos(2\Delta\omega t) + B - 1 + \cos(2\Delta\omega t) - B}{1 + \cos(2\Delta\omega t) + B + 1 - \cos(2\Delta\omega t) + B} = \frac{\cos(2\Delta\omega t)}{1 + B} \tag{134}$$

We can see that if the background amounts to just 2%, which in the case of the experimental setup amounts to just 1 count per second. The polarization is reduced to $\frac{1}{1.02} = 98\%$.
One can see that all of these factors bring down the visibility from 96.5% (base polarization) to 80.6%.

5.6.2 Frequency Dependent Factors

In this subsection we will look at frequency dependent visibility losses. It is thought that chopper jitter is the main cause of visibility loss. The frequency of the chopper varies slightly in time (jitters), which can cause the RF coils and the detector to be started earlier than when the neutrons actually arrive (if the disks are slower than expected) or later than when the first neutrons arrive (if the disks are faster than expected). As a result some unwanted averaging over the MIEZE signal takes place, which lowers the observed amplitude. From section 2.6 we know that the MIEZE phase at the detector is given by:

$$\phi = 2\Delta\omega t = 2\Delta\omega(t_0 + t') \tag{135}$$

Where t_0 is the time when the RF flippers turn on and t' is the particular time within the pulse. If the chopper has some jitter, this MIEZE phase gets a small error, characterized by Δt

$$\phi = 2\Delta\omega(t_0 \pm \Delta t + t') \tag{136}$$

The detector will start to measure at a fixed t_{delay} after receiving the pulse from the chopper. However the neutrons may arrive a bit sooner or later (Δt), due to chopper jitter. As a result the phase of the MIEZE signal at the time when the detector turns on is given by

$$\phi = 2\Delta\omega(t_0 \pm 2\Delta t) \tag{137}$$

Thus due to the fact that both the detector and the RF flippers are triggered by the chopper, the effect of jitter is doubled. We can determine the effect on the visibility simply by averaging the MIEZE signal over Δt, assuming a Gaussian jitter (note we set $t_0 = 0$ for convenience and C is the normalization factor)

$$< \sigma_x >= \int_{-\infty}^{\infty} Ce^{-\frac{1}{2}\frac{t^2}{dt^2}} \cos(4\Delta\omega t)dt = e^{-8\Delta\omega^2\Delta t^2} \tag{138}$$

Δt was measured to be on the order of $0.8\mu s$. We find that in this case the visibility is reduced to 60%. If the jitter is slightly larger, for example $1.2\mu s$, the visibility would be reduced to just 32.1%.

Another, although small, frequency dependent factor could be inelastic scattering of neutrons in air. Though very few neutrons will scatter along the flightpath and make it to the detector, those that do will be completely depolarized. This may cost another $1\% - 2\%$.

5.6.3 Summary

The loss of visibility is determined by a variety of frequency independent factors, such as rotator angle, flipper efficiency and base polarization, but also by frequency dependent factors such as detector thickness, focal spot size, averaging due to sampling and chopper jitter. When all these effects are taken into account the maximum achievable visibility at $100kHz$ (MIEZE frequency) should be between 39% and 46% (at 2Å wavelength). In reality a maximum visibility of $35\% \pm 2\%$ is observed on the experimental setup. Thus it appears that most, but not all factors which contribute to visibility loss have been explained.

6 Outlook

It has been demonstrated that the high field flippers which are also used by the Larmor instrument are capable of producing a MIEZE signal of $100kHz$. The next step is to attempt to generate a MIEZE signal using the Larmor instrument and to gradually increase the modulation frequency into the MHz range. Due to the small focus size at these frequencies and the aforementioned frequency dependent degradation of the visibility it is recommended to use the MIEZE startup procedure described in the method section. In these initial tests we plan to measure the self diffusion of water at various temperatures (see section 2.8). If the Larmor instrument functions at these frequencies one can expect spin echo times of up to $35ns$ (10Å wavelength) at the sample position. In addition the MIEZE mode at Larmor should also be tested using the gradient coils which are integrated into the flippers. This should increase the stability of the flip. It should be noted that even in this case the RF coils must be triggered by each time of flight pulse or else it will definitely not work in time of flight (section 5.6.2). Possible pitfalls which could prevent the Larmor instrument from doing MHz MIEZE are detector thickness (CASCADE detector required), jitter of the time of flight pulse, vibrations/thermal expansion, which cause the distance between the two spin flippers to change and scattering of neutrons on molecules in the air (vacuum flight tube required).

If successful the MIEZE mode of Larmor may be used to explore the dynamics of magnetic materials [42] and to develop new methods for quasi-elastic neutron scattering like MISANS, a combination of SANS and MIEZE [42][43][44]. Another possibility would be to attempt SEMSANS in a MIEZE configuration (SEMSANS with only two flippers), this could potentially also allow for the combination of both techniques.

7 Conclusion

The main goal of this research was to demonstrate that resonant RF flippers, which use magnetic poleshoes to obtain high magnetic fields, are applicable to the MIEZE technique. Evidence has been provided that these novel high field flippers are indeed capable of producing a MIEZE signal of up to $100kHz$. In addition it was shown that the MIEZE signal obtained has an amplitude similar to the signals that could be obtained using more conventional spin flippers. Furthermore effects of detector thickness on the measured MIEZE amplitude were demonstrated both experimentally and with Monte-Carlo simulations. The results show that a very thin detector (i.e. CASCADE) is required to measure high frequency MIEZE signals. In addition the shape of the MIEZE focal spot was modeled to be Gaussian. This was confirmed experimentally using a position sensitive detector. Finally the importance of a stable pulse frequency and the effects it has on the measured MIEZE amplitude was derived. This research provides the confidence required to start to test and implement MIEZE on the Larmor instrument at ISIS neutron source in the UK. In these tests the instrument will be pushed to its limits possibly achieving MHz modulation and $20ns$ spin echo time. This would enable the research of a variety of materials, including magnetic materials which are critical for quantum computing and improved memory.

References

[1]: A. Taylor, et al. Science Vol. 135 Issue 5815, (2007) 1092-1095.
[2]: T.E. Mason, et al. Physica B **385-386**, (2006) 955-960.
[3]: M. T. Rekveldt, et al. Review of Scientific Instruments **76**, (2005) 033901.
[4]: R. Golub, et al. Am. J. Phys. **62** (9), (1994) 779-778.
[5]: G. Brandl, et al. Nucl. Instr. And Meth. A **654**, (2011) 394-398.
[6]: https://www.mlz-garching.de/reseda
[7]: W. Haeussler and L. Kredler AIP Conference Proceedings **1599** 298, (2014).
[8]: S.A. Wolf, et al. IBM J. Res. and Dev. Vol. 50 No. 1 (2006) 101-110.
[9]: J. Tejada, et al. Nanotechnology **12**, (2001) 181-186.
[10]: W.H. Kraan, et al., Nucl. Instr. And Meth. **510**, (2003) 334-345.
[11]: H. Hayashida, et al., Nucl. Instr. and Meth. **574**, (2007) 292-296.
[12]: F: Mezei, Physica B **151**, (1988) 74-81.
[13]: V.K. Ignatovich and F.V. Ignatovich, Am. J. Phys. **71**, (2003) 1013-1024.
[14]: W. Besenbck et al., J. Neutron Research vol. 7, no. 1, (1998) 65-74
[15] W.H. Kraan *Instrumentation to handle thermal polarized neutron beams*, PhD Thesis, Interfaculty Reactor Institute, Delft University of Technology, Netherlands (2004).
[16] H.M. Shimizu, et al., Physica B **276-278**, (2000) 63-64.
[17] J. Fuezi, et al., Physical B **350**, (2004) 169-172.
[18] V.G. Syromyatnikov, V.M. Pusenkov, IOP Conf. Series: Journal of Physics: Conf. Series **862**, (2017) 012028.
[19]: N. Arend *New Aspects of the MIEZE Technique and Verification of the Multi-level MIEZE Principle*, PhD Thesis, Technische Universitaet Muenchen, Germany (2007).
[20] J. Plomp *Spin Echo development for a time of flight neutron reflectometer* Interfaculty Reactor Institute, PhD Thesis, Delft University of Technology, Netherlands (2009).
[21] J. Zhao, et al., Appl. Phys. Lett. **107**, (2015) 113508.
[22] T. Oda et al., Review of Scientific Instruments **87**, (2016) 105124.
[23] M. Strobl, Scientific Reports **4**, (2014) 7243.
[24] M. Koeppe, et al., Physica B **266**, (1999) 75-86.
[25] G. Squires, *Introduction to the Theory of Thermal Neutron Scattering*, Dover Publications, United Kingdom, (1997)
[26] Y. Nazarov and J. Danon, *Advanced Quantum Mechanics*, Cambridge University Press, United Kingdom, (2013)
[27] J.P. Hansen and I.R.McDonald *Theory of Simple Liquids*, Academic Press, Inc., United States of America, (1986).
[28] M. Bleuel and A.A. van Well, Physica B **406**, (2011) 2478-2481.
[29] J. Teixeira, et al., Phys. Rev. A, Vol. 31 **3** (1985) 1913-1917.
[30] L. Cavatorta et al., Jounral of Physics: Condensed Matter 6 (1994) A**113**.
[31] A.A. van Well, Physica B **180**, (1992) 959-961.
[32] A.A. van Well and H. Fredrikze, Physica B **357**, (2005) 204-207.
[33] W.H. Kraan et al., Nucl. Instr. And Meth. A **300** (1991) 35-42.
[34] F. Groitl et al., Review of Scientific Instruments **86**, (2015) 025110.
[35] T. Keller et al., Physica B **162**, (1990) 327-330.
[36] W.H. Kraan et al., Physica B **297**, (2001) 23-27.
[37] M. Koehli et al. J. Phys.: Conf. Ser. **746** (2016) 012003.
[38] M. Batz et al., J. Res. Natl. Inst. Stand. Technol. **110**, (2005) 293-298.
[39] N. Martin, Nucl. Instr. And Meth. A **882**, (2018) 11-16.
[40] M. Abramowitz and I.A. Stegun, Handbook of Mathematical Functions with Formulas, Graphs, and Mathematical Tables, 9th printing. New York: Dover, (1972).
[41] http://mathworld.wolfram.com/FourierTransformGaussian.html.
[42] G. Brandl et al., Nucl. Instr. And Meth. A **667**, (2012) 1-4.
[43] M. Bleuel et al., Nucl. Instr. And Meth. A **600**, (2009) 220-222.

[44] M. Bleuel et al., Physica B **356**, (2005) 213-217.

Appendix

RF Waveform generation script.

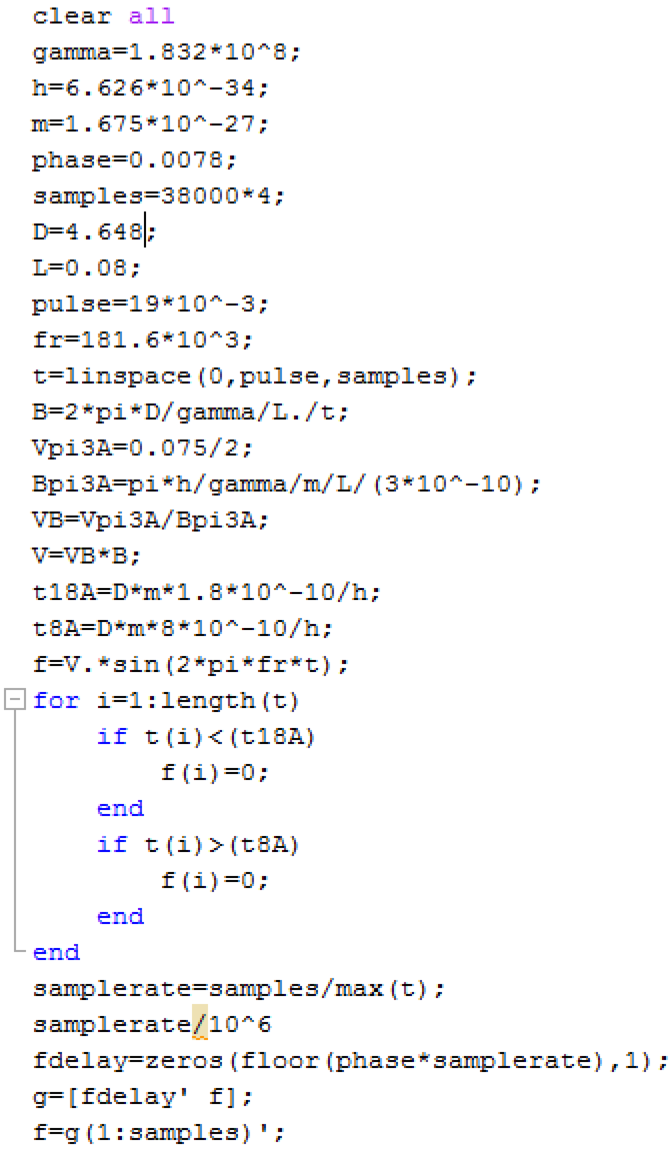

```
clear all
gamma=1.832*10^8;
h=6.626*10^-34;
m=1.675*10^-27;
phase=0.0078;
samples=38000*4;
D=4.648;
L=0.08;
pulse=19*10^-3;
fr=181.6*10^3;
t=linspace(0,pulse,samples);
B=2*pi*D/gamma/L./t;
Vpi3A=0.075/2;
Bpi3A=pi*h/gamma/m/L/(3*10^-10);
VB=Vpi3A/Bpi3A;
V=VB*B;
t18A=D*m*1.8*10^-10/h;
t8A=D*m*8*10^-10/h;
f=V.*sin(2*pi*fr*t);
for i=1:length(t)
    if t(i)<(t18A)
        f(i)=0;
    end
    if t(i)>(t8A)
        f(i)=0;
    end
end
samplerate=samples/max(t);
samplerate/10^6
fdelay=zeros(floor(phase*samplerate),1);
g=[fdelay' f];
f=g(1:samples)';
```

First Data Processing Script.

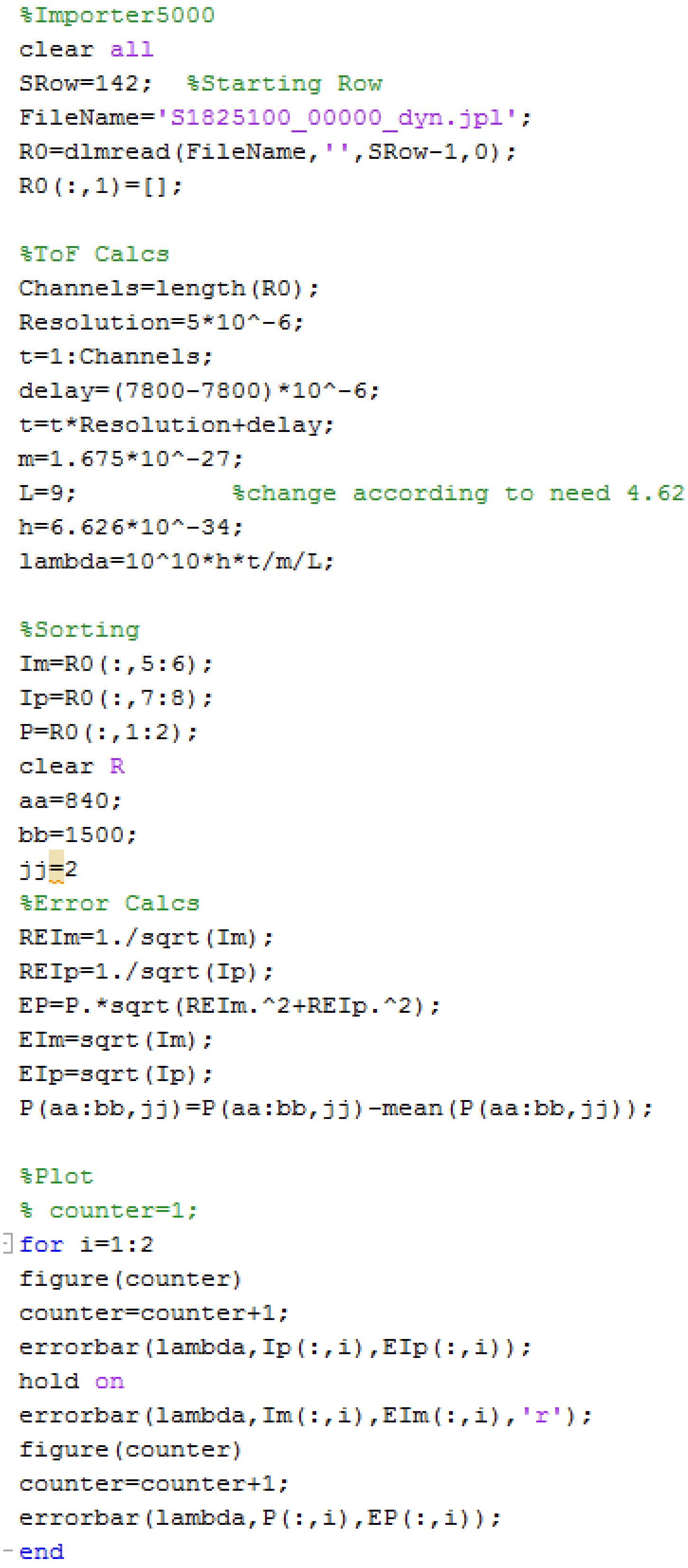

```
%Importer5000
clear all
SRow=142;  %Starting Row
FileName='S1825100_00000_dyn.jpl';
R0=dlmread(FileName,'',SRow-1,0);
R0(:,1)=[];

%ToF Calcs
Channels=length(R0);
Resolution=5*10^-6;
t=1:Channels;
delay=(7800-7800)*10^-6;
t=t*Resolution+delay;
m=1.675*10^-27;
L=9;          %change according to need 4.62
h=6.626*10^-34;
lambda=10^10*h*t/m/L;

%Sorting
Im=R0(:,5:6);
Ip=R0(:,7:8);
P=R0(:,1:2);
clear R
aa=840;
bb=1500;
jj=2
%Error Calcs
REIm=1./sqrt(Im);
REIp=1./sqrt(Ip);
EP=P.*sqrt(REIm.^2+REIp.^2);
EIm=sqrt(Im);
EIp=sqrt(Ip);
P(aa:bb,jj)=P(aa:bb,jj)-mean(P(aa:bb,jj));

%Plot
% counter=1;
for i=1:2
figure(counter)
counter=counter+1;
errorbar(lambda,Ip(:,i),EIp(:,i));
hold on
errorbar(lambda,Im(:,i),EIm(:,i),'r');
figure(counter)
counter=counter+1;
errorbar(lambda,P(:,i),EP(:,i));
end
```

Second Data Processing Script

```
%Importer9000 Modified to include Normalization
clear all
SRow=142;  %Starting Row
FileName='S1816016_00000_dyn.jpl';
R=dlmread(FileName,'',SRow-1,0);
R(:,1)=[];

%ToF Calcs
Channels=length(R);
Resolution=1.2*10^-6;
t=1:Channels;
delay=(11000-7800)*10^-6;
t=t*Resolution+delay;
m=1.675*10^-27;
L=9;           %change according to need 4.62
h=6.626*10^-34;
lambda=10^10*h*t/m/L;

%Sorting
Im=R(:,33:48);
Ip=R(:,49:64);
P=R(:,1:16);
clear R

%Error Calcs
REIm=1./sqrt(Im);
REIp=1./sqrt(Ip);
EP=P.*sqrt(REIm.^2+REIp.^2);
EIm=sqrt(Im);
EIp=sqrt(Ip);

%NormData
FileName='S1817001_00000_dyn.jpl';
R=dlmread(FileName,'',SRow-1,0);
R(:,1)=[];

%Sorting
Im0=R(:,33:48);
Ip0=R(:,49:64);
P0=R(:,1:16);
clear R

%Error Calcs
REIm0=1./sqrt(Im0);
REIp0=1./sqrt(Ip0);
EP0=P0.*sqrt(REIm0.^2+REIp0.^2);
EIm0=sqrt(Im0);
EIp0=sqrt(Ip0);

%Begin Normalization
PN=P./P0;
EPN=PN.*sqrt(EP0.^2./P0.^2+EP.^2./P.^2);
```

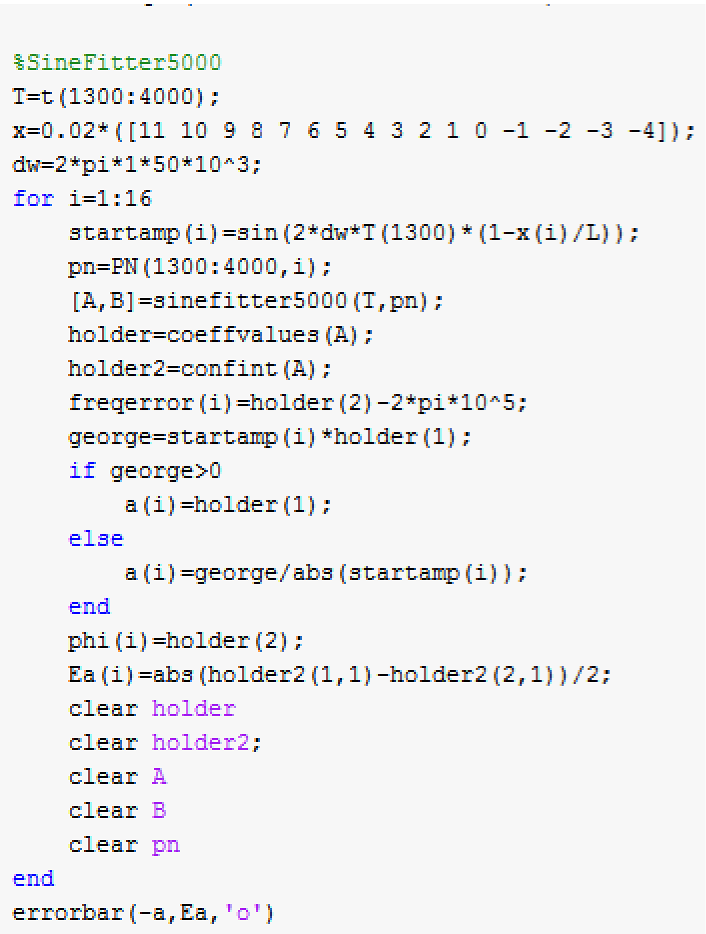

```
%SineFitter5000
T=t(1300:4000);
x=0.02*([11 10 9 8 7 6 5 4 3 2 1 0 -1 -2 -3 -4]);
dw=2*pi*1*50*10^3;
for i=1:16
    startamp(i)=sin(2*dw*T(1300)*(1-x(i)/L));
    pn=PN(1300:4000,i);
    [A,B]=sinefitter5000(T,pn);
    holder=coeffvalues(A);
    holder2=confint(A);
    freqerror(i)=holder(2)-2*pi*10^5;
    george=startamp(i)*holder(1);
    if george>0
        a(i)=holder(1);
    else
        a(i)=george/abs(startamp(i));
    end
    phi(i)=holder(2);
    Ea(i)=abs(holder2(1,1)-holder2(2,1))/2;
    clear holder
    clear holder2;
    clear A
    clear B
    clear pn
end
errorbar(-a,Ea,'o')
```

Sinefitter

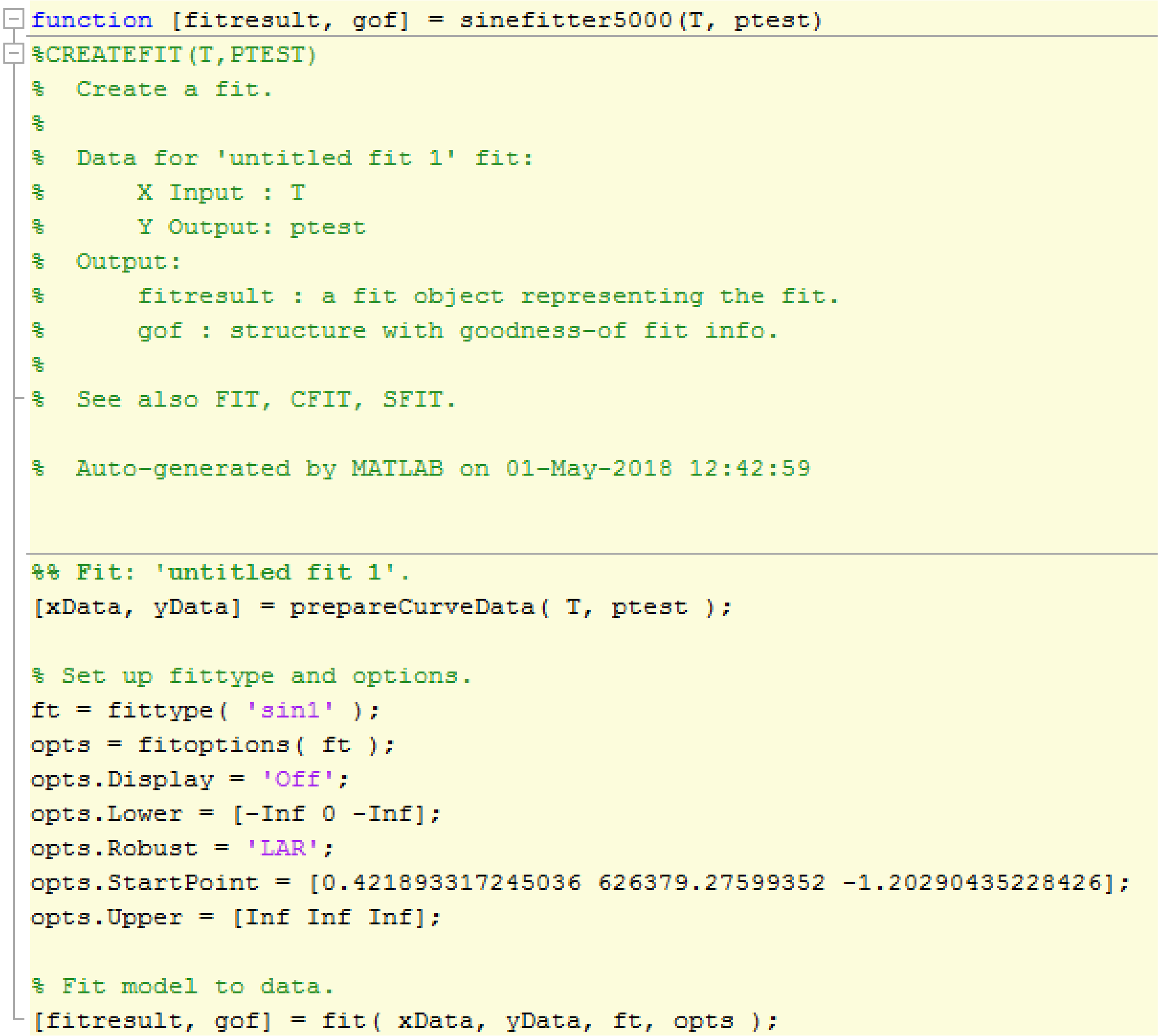

```
function [fitresult, gof] = sinefitter5000(T, ptest)
%CREATEFIT(T,PTEST)
%  Create a fit.
%
%  Data for 'untitled fit 1' fit:
%      X Input : T
%      Y Output: ptest
%  Output:
%      fitresult : a fit object representing the fit.
%      gof : structure with goodness-of fit info.
%
%  See also FIT, CFIT, SFIT.

%  Auto-generated by MATLAB on 01-May-2018 12:42:59


%% Fit: 'untitled fit 1'.
[xData, yData] = prepareCurveData( T, ptest );

% Set up fittype and options.
ft = fittype( 'sin1' );
opts = fitoptions( ft );
opts.Display = 'Off';
opts.Lower = [-Inf 0 -Inf];
opts.Robust = 'LAR';
opts.StartPoint = [0.421893317245036 626379.27599352 -1.20290435228426];
opts.Upper = [Inf Inf Inf];

% Fit model to data.
[fitresult, gof] = fit( xData, yData, ft, opts );
```

```cpp
#include "stdafx.h"
#include <math.h>
#include <stdio.h>
#include <iostream>
#include <string>
#include <fstream>
#include <stdlib.h>     /* srand, rand */
#include <time.h>
#include <string>
#include <random>
using namespace std;

void main()
{
        ofstream FOMd;
        ofstream Pd;
        FOMd.open("FOMd.bin", ios::out | ios::app | ios::binary);
        Pd.open("Pd.bin", ios::out | ios::app | ios::binary);
        srand(time(NULL));
        double INST_RES = 1; //Instrument Max pol
        double Sm = 159; //macroscopic xsection
        double m = 1.675e-27; //neutron mass
        double h = 6.626e-34; //Planck Constant
        double lambda; //Wavelength
        double lres; //wavelength res
        cout << "Wavelength (Angstrom)? ";
        cin >> lambda;
        lambda = lambda*1e-10;
        cout << "Wavelength Resolution (percentage)?";
        cin >> lres;
        double dlam = 0.01*lres*lambda;
        double v = h / lambda / m; //Velocity
        double dm;
        cout << "Distance Modifier? ";
        cin >> dm;
        double D[] = { 1e-3, 2e-3, 3e-3, 4e-3, 5e-3, 6e-3, 7e-3, 8e-3, 9e-3, 10e-3, 11e-3, 12e-3, 13e-
3, 14e-3, 15e-3, 16e-3, 17e-3, 18e-3, 19e-3, 20e-3 };
        int L = 20; //Number of elements in D
        double samp; //sampling time
        cout << "Sampling time (microseconds)? ";
        cin >> samp;
        samp = samp*1e-6;
        double samp2 = samp;
        double f; //MIEZE Frequency
        cout << "MIEZE Frequency (kHz)? ";
        cin >> f;
        f = f*1e3;
        samp = 1 / f / 10;
        double w = 2 * 3.1415*f;
        double N; //Number of Runs
        cout << "Number of Runs? ";
        cin >> N;
        double *t; //Time
        int T = ceil(10 / f / samp); //Length of time signal
        t = new double[T];
        int range_from = 0;
        int range_to = 1e4;
        std::random_device                  rand_dev;
        std::mt19937                        generator(rand_dev());
        std::uniform_int_distribution<int>  distr(range_from, range_to);
        double *s1; //I+ Signal
        double *s2; //I- Signal
        s1 = new double[T];
        s2 = new double[T];
        double *sp1; //I+ Signal
        double *sp2; //I- Signal
        sp1 = new double[T];
        sp2 = new double[T];
        double *S1;
        S1 = new double[T];
        double *S2;
        S2 = new double[T];
        double *F;
        F = new double[T];
        double *P;
        P = new double[L];
```

```
        double *FOM;
        FOM = new double[L];
        for (int i = 0; i < T; i++)
        {
                t[i] = samp*i;
                S1[i] = 0;
                S2[i] = 0;
        }
        double Ultimate = 1 / samp2 / w * 2 * sin(w*samp2 / 2);
        double rn;
        double tabs;
        int tabs2;
        double dumb = 0;
        for (int i = 0; i < L; i++)
        {
                double n = 0;
                double tmax = dm*D[i] / v;
                for (int j = 0; j < N; j++)
                {
                        for (int k = 0; k < T; k++)
                        {
                                rn=distr(generator);
                                //rn = rand() % 10000;
                                tabs = -1 / Sm / v*log(rn/ range_to);
                                double Amp = exp(-3.1415*3.1415*2*(2*w*m*tabs/h/2/3.1415)*(2 *
w*m*(tabs-1/Sm) / h / 2 / 3.1415)*dlam*dlam);
                                //double Amp = 1;
                                tabs2 = ceil(tabs / samp);
                                for (int jk = 0; jk < T; jk++)
                                {
                                        s1[jk] = 1 + Amp*cos(w*t[jk]);
                                        s2[jk] = 1 - Amp*cos(w*t[jk]);
                                }
                                if (tabs < tmax)
                                {
                                        n = n + 1;
                                        if (tabs2 + i <= T)
                                        {
                                                sp1[k] = s1[tabs2 + k];
                                                sp2[k] = s2[tabs2 + k];
                                        }
                                        else {
                                                int k2 = tabs2 + k - T;
                                                sp1[k] = s1[k2];
                                                sp2[k] = s2[k2];
                                        }

                                }
                                else {
                                        sp1[k] = 0;
                                        sp2[k] = 0;
                                }
                                S1[k] = S1[k] + sp1[k];
                                S2[k] = S2[k] + sp2[k];
                        }

                }
                for (int k = 0; k < (T-ceil(2/f/samp)); k++)
                {
                        F[k] = INST_RES*(S1[k] - S2[k]) / (S1[k] + S2[k]);
                }
                dumb = 0;
                for (int k = 0; k < (T - ceil(2 / f / samp)); k++)
                {
                        if (F[k] > dumb)
                        {
                                dumb = F[k];
                        }
                }
                P[i] = Ultimate*dumb;
                FOM[i] = Ultimate*Ultimate*dumb*dumb*n;
                FOMd << FOM[i] << endl;
                Pd << P[i] << endl;
        }
        FOMd.close();
        Pd.close(); }
```

A Time of Flight MIEZE Spectrometer

N. Geerits, S.R. Parnell, M.A. Thijs, W. Bouwman and J. Plomp
Faculty of Applied Sciences, Delft University of Technology, 2629JB Delft, The Netherlands

Concept

- Utilize two resonant flippers to introduce $\Delta\phi$ between two spin states
- Timescale given by: $\frac{\Delta\phi(x)}{\omega_n} = \tau_{echo}$
- $\Delta\phi = 0$ at detector (focus condition)
- Polarization is modulated in time with $\omega = 2\gamma\Delta B$

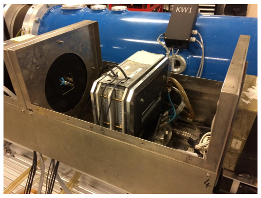

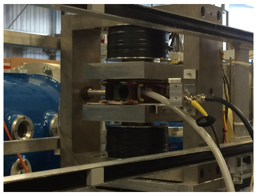

Motivation

- Inelastic scattering
- Magnetic samples (sample can be placed after the analyzer)
- Combination of elastic and inelastic measurements (MISANS)
- Timescales up to 20ns (RESEDA)

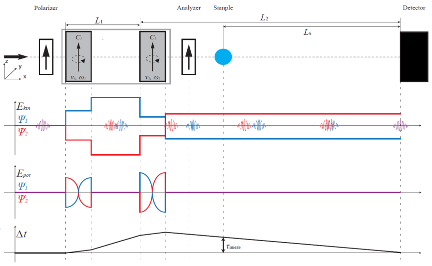

Goals

We have developed a new spin flipper (gradient flipper which are used by Larmor). We wish to test how applicable these coils are to MIEZE. Tests are done in ToF to prove the feasibility of MIEZE at pulsed sources.

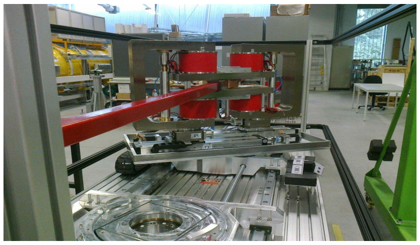

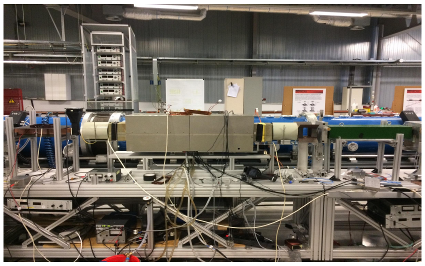

Method

- Build a conventional MIEZE setup using resonant flippers
- Construct a MIEZE setup using the novel gradient coils
- Compare the two resulting MIEZE signals

Benchmark

- Resonant coils have well defined fields
- 100kHz ToF MIEZE setup
- ToF achieved by ramping the RF field
- Contrast of 40%
- Using a PSD the focal point was imaged and was found to be 6cm wide

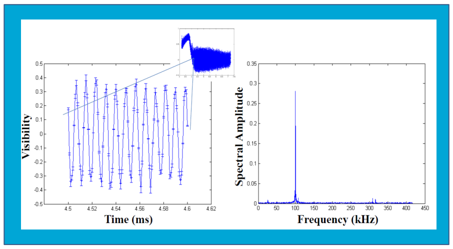

Modeling

- Gradient MIEZE requires a guide field to prevent depolarization
- Focus is very sensitive to small changes in fields and path lengths

→ Therefore it is important to compare analytic predictions with FEM

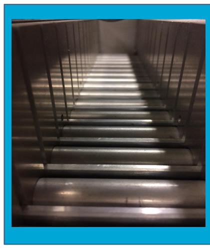

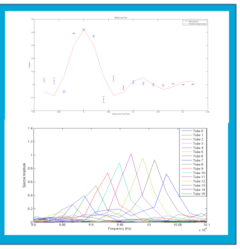

Gradient MIEZE Tests

- Focus can be moved by tuning the frequency of one of the flippers
- Until now these flippers have only been tested in “1/t resonant mode”
- Several MIEZE frequencies (20kHz,40kHz,100kHz)

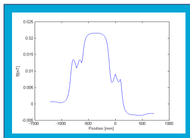

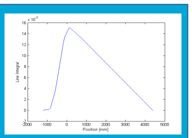

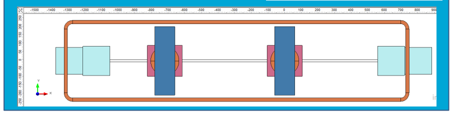

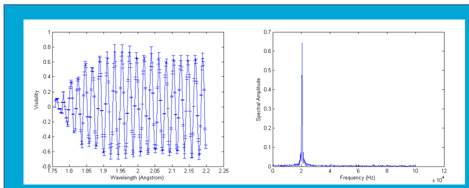

20 kHz

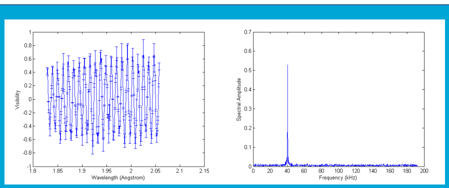

40 kHz

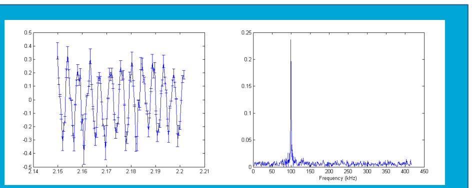

100 kHz

Outlook

Next we wish to attempt MIEZE using the Larmor instrument at ISIS. We believe that we can achieve 1-2MHz modulation and spin echo times of up to 40ns for 8 Angstrom neutrons

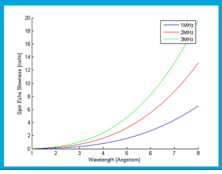

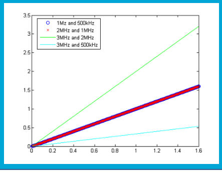

TU Delft Delft University of Technology